TÉCNICO LISBOA

Design, modelling and characterization of porous structures produced by metal additive manufacturing for application in temporary bone implants

Beatriz Rocha Antão Rodrigues

Thesis to obtain the Master of Science Degree in

Materials Engineering

Supervisors: Prof. Augusto Manuel Moura Moita de Deus
Eng. Pedro Afonso Ferreira Nogueira

Examination Committee

Chairperson: Prof. Alberto Eduardo Morão Cabral Ferro
Supervisor: Prof. Augusto Manuel Moura Moita de Deus
Members of the Committee: Prof. Alexandre José da Costa Velhinho

December 2023

This work was created using LaTeX typesetting language
in the Overleaf environment (www.overleaf.com).

Declaration

I declare that this document is an original work of my own authorship and that it fulfills all the requirements of the Code of Conduct and Good Practices of the Universidade de Lisboa.

Acknowledgments

Firstly, I would like to deeply thank my supervisors, Professor Augusto Moita de Deus and Pedro Nogueira, for allowing me to work on this project, for being supportive, patient and for providing valuable guidance and feedback, challenging me throughout the project's development. I also want to thank them for their availability and support, and for providing me with the necessary tools to prosper.

I am also grateful for the professors involved in the "GradImp - Implantes biodegradáveis em ferro poroso obtidos por fabrico aditivo", a FCT Project PTDC/CTM-CTM/3354/2021, particularly Professor Fátima Vaz, Professor Beatriz Silva and Professor João Magrinho for the helpful insights and availability to discuss the thesis's development. For producing the samples, I would like to thank INEGI.

I am thankful for my friends and colleagues who always listened to me during stressful times, and provided brief moments of distraction from my responsibilities.

I would like to thank my family, my mom, dad and sister, for giving me everything I needed to make me able to prospect and for always believing in me and supporting my dreams and ambitions. Without their unconditional support, I would not be where I am today.

Lastly, I would like to thank Afonso, for listening to me countless times about my thesis, for helping me get to where I am, believing in me, and always being willing to help me. For being there by my side.

Abstract

As life expectancy increases, with its associated health issues, the field of orthopaedics has seen a rise in demand in recent times. Bones lose their ability to regenerate due to diseases and cellular behaviour [1], which decreases the ability of self-regenerative tissues and increases the risk of fractures [2]. To help regeneration of fractures, prostheses and plates have been used for decades, and have undergone continuous improvements over time. Recently, biodegradable materials and lattice structures have been evolving to be implemented in medical uses, such as temporary implants, that mimic the behaviour of bones. Additive Manufacturing (AM) technologies are used to print these complex structures, that otherwise would be very difficult to produce. Lattice structures are made of a repetition of unit cells, and this study focuses on two types of unit cells (Rhombitruncated Cuboctahedron (RTCO) and Truncated Octahedron (TO)) to be implemented in biodegradable prostheses made from 99.8% pure Iron and produced by Selective Laser Melting (SLM). The mechanical behaviour of plates made of these structures was evaluated through experimental Three-Point Bending (3PB) and Finite Element Analysis (FEA). Energy absorption (E_a), stiffness (k), as well as reaction force (RF) vs. displacement (U) were studied. Computational validation analysis, comparison between the mechanical properties of different cells with different densities, bones and performance indexes analysis were conducted. The computational model accurately represents the mechanical behaviour of the samples. RTCO have higher k and E_a values than TO cells for the same relative density ($\bar{\rho}$). Except for those with 5% $\bar{\rho}$, all of the other cells are stable and suitable for use in prostheses or plates, the selection depends on the fracture being treated.

Keywords

Bone prosthesis; Three-Point Bending (3PB); Finite Element Method (FEM); Cellular Structure; Biodegradability; Additive Manufacturing (AM)

Resumo

Os ossos perdem a capacidade de regeneração com a idade [1], diminuindo a capacidade de auto-regeneração dos tecidos e aumentando o risco de fracturas [2]. O campo de medicina ortopédica tem assistido a um aumento dos problemas de saúde relacionados com fracturas. Para facilitar a regeneração de fracturas, próteses e placas ortopédicas têm sido utilizadas. Materiais biodegradáveis e estruturas celulares têm sido estudados para produção de próteses temporárias que mimetizam o comportamento dos ossos. Tecnologias de fabrico aditivo são utilizadas para produzir materiais com estruturas celulares complexas, que de outra forma não seriam possíveis de produzir. A presente tese estuda dois tipos de células a serem implementadas em próteses biodegradáveis produzidas em ferro 99,8% puro por fusão seletiva por laser. O comportamento mecânico das células (Rhombitruncated Cuboctahedron (RTCO) e Truncated Octahedron (TO)) são analisados por flexão de três pontos através de ensaios experimentais e de análise de elementos finitos, nomeadamente pelo estudo de grandezas como a absorção de energia (E_a), rigidez (k) bem como força de reacção (RF) vs. deslocamento (U). Foram efectuadas análises de validação computacional, comparação de propriedades mecânicas de diferentes células com diferentes densidades e análises de índices de desempenho. O modelo computacional representa corretamente o comportamento mecânico das amostras. As células RTCO apresentam rigidez e energia absorvida superiores do que as células TO quando têm a mesma densidade relativa. Com exceção das células com 5% de densidade relativa, todas as outras células são estáveis e adequadas para próteses.

Palavras Chave

Prótese óssea; Ensaio de flexão a três pontos; Método de elementos finitos; Estrutura celular; Biodegradação; Manufatura Aditiva

Contents

List of Figures

List of Tables

List of Symbols

A	cross-sectional area
D_{Ap}	apparent density
D_{Ash}	ash density
E_a	absorption energy
E	Young' s modulus
F	force
I	moment of inertia
L_0	original length
Ln	final length
MRF	maximum reaction force
M	bending moment
P	load
V_M	material volume
V_R	real volume
V_T	total volume
V_p	total volume of open spaces or voids in a material
W_w	wet weight
W_{Ash}	ash weight
Δ	displacement
$\bar{\rho}$	relative density
δ	deflection
ϵ	strain
ϕ_B	bulk porosity
ϕ	porosity
$\rho*$	cellular material density
ρ_s	solid material density
ρ	density
σ_e	engineering stress
σ_t	true stress
σ_y	yield stress
σ_b	bending stress
σ_{max}	maximum stress
σ	stress

ε_e	engineering strain
ε_t	true strain
d_n	neutral axis distance
d	diameter of cross-section
k	stiffness
m	mass

Acronyms

3PB	Three-Point Bending
AM	Additive Manufacturing
BTE	Bone Tissue Engineering
C	Cubic
CAD	Computer-Aided Design
DCP	Dynamic Compression Plates
EDM	Electrical Discharge Machining
FEA	Finite Element Analysis
FEM	Finite Element Method
LC-DCP	Limited Contact Dynamic Compression Plate
LCP	Locking Compression Plate
MAM	Metal Additive Manufacturing
PBF	Powder Bed Fusion
RCO	Rhombicuboctahedron
RF	Reaction Force
RTCO	Rhombitruncated Cuboctahedron
SLM	Selective Laser Melting
SS	Stainless Steel
STL	Standard Triangle Language
TC	Truncated Cube
TO	Truncated Octahedron

1

Introduction

1.1 Introduction

Nowadays, as life expectancy increases globally, medical issues have increasingly become a matter of attention. Consequently, bone fractures have been a public health issue [3, 4]. This concern is furthermore justified by the function of bones, which provide both structural support and protection of organs. Despite the fact that bones have the ability to self-regenerate, in many cases, fractures do not heal completely. It is estimated that about 10% of bone fractures result in nonunion or incomplete healing [5, 6].

In addition, fractures can occur due to several factors, including diseases, such as osteoporosis, which causes bone fragility and leads to fractures [7], most of which require surgery and specialized medical equipment, which can be challenging for both surgeons and investigators [8].

Fractures in elderly patients with osteoporosis can increase mortality by 20%, compared to those without fractures [3]. Additionally, individuals over 50 years old have a 74% increased risk of fractures [9].

Fractures can lead to other social problems, including physical incapacity, reduced quality of life, lost productivity, declining health, and increased healthcare costs for individuals, families, societies, and healthcare systems [10].

According to a recent study by Ai-Min et al. [10], there has been a 33.4% increase in fractures since 1990, resulting in 178 million new cases worldwide. Another study estimates that age-related fractures in the United States will increase from 2.1 million in 2005 to over 3 million in 2025 [11]. Moreover, the Global Burden of Disease, Injuries, and Risk Factors Study (GBD) reported that musculoskeletal problems affect 1.71 billion people globally [4].

Permanent and temporary prostheses have been developed, as well as biodegradable medical devices, to promote the repair and regeneration of different tissues [4, 12]. Bone tissue engineering (BTE) has aroused interest in the application of temporary bone implants. The implants degrade inside the patient's body with the help of fluids. Meanwhile, the fractured bone regenerates and replaces the implant completely. This process avoids a second surgery to remove the prosthesis and consequently less cost and pain to the patient.

Advancements in this field can be achieved through experimental methods that take real scenarios

into account and correlate directly with clinical applications. However, there are some disadvantages, as it can be costly and challenging to control certain experimental data. In order to overcome these issues, simulations can be conducted using the Finite Element Method (FEM) to study the bone structure and materials used in medicine. This approach can provide a better understanding of clinical limitations, and prepare for potential scenarios. [6].

Specific data can be studied to correlate mechanical behaviour and tissue regeneration, such as strain, pressure, stability, and fluid velocity [6, 12]. FEM has been used by researchers to analyze various mechanical phenomena. The correlation between strain and relative velocity in cells and tissues by FEM was investigated by Prendergast et al. [13], while Søballe [14] and Carter et al. [15], studied the mechanical requirements to promote regeneration of tissues [6].

New materials have been utilized for biomedical applications, either by studying composition or developing structured materials. The application of engineered geometries in materials tends to be an ideal representation of structures present in nature, such as honeycombs or foams. These structures promote enhanced specific properties with less density when compared to bulk materials.

Therefore, materials with engineered geometries applied, have been studied to optimize the design and arrangement of the unit cell, as properties depend highly on the geometry [16].

Lattice and cellular structured materials have an important role in the advancement of medical equipment, due to exceptional performance and properties. Nowadays this type of material is already used in some applications, such as biological tissue engineering, however, this field is expected to further progress in the future [16]. Since bone is a cellular material, lattice and cellular structures are largely studied to mimic bone properties and avoid stress shield issues between bone-prosthesis interfaces [17].

The need to customize prostheses for patients' unique conditions and the complexity of lattice structures makes Additive Manufacturing (AM) technology suitable for this application[17]. This technology has shown a promising future, due to high control in the production of small series, which allows for personalization in geometry and materials. The use of medical scanners promotes the possibility of computer-aided design, which facilitate design and the implementation of devices in the patient [18].

Nowadays AM is utilized to create biomaterials to act as scaffolds for tissue and bone repair [19], custom-made clear aligners for the dental industry and biobased implantable products such as bone implants, joint replacement, devices and stents [18].

Biomaterials play an important role in the medical industry. The concept of biomaterials dates back to ancient Egyptian times, approximately 4000 years ago, when animal-origin sutures were first used and since then have been developed further. It is estimated that the biomaterial industry will generate an increase in revenue from $178 billion in 2019 to $287 billion in 2026 [18].

Despite the advancements and studies, there is still room for improvement, as recent discoveries and applications still have limitations and do not meet the ideal outcome [8, 19]. In the 1950s Professor

Sir Charnley, a recognized orthopaedic surgeon, stated “Practically all classical operations of surgery have now been explored, and unless some revolutionary discovery is made which will put the control of osteogenesis[1] in the surgeon’s power, no great advance is likely to come from modification of their detail”. To this day, no bone substitute has been developed [12]. To summarise, there is a necessity to continue developing and studying treatments and strategies for bone healing in order to overcome limitations such as extended recovery time, patients’ pain and high treatment costs [12].

This study was performed under the scope of a larger project called ”GradImp - Implantes biodegradáveis em ferro poroso obtidos por fabrico aditivo”, which is funded by FCT (PTDC/CTM-CTM/3354/2021). The objective of the project is to produce prostheses printed by Selective Laser Melting (SLM) with 99,8% purity Iron. The material has the capacity to self-degrade without significant harmful effects and safe absorption by the human body, enabling it to imitate natural bone and respond to the tissue’s needs during the regeneration process.

The present thesis intends to study and understand further the use of cellular-structured materials for orthopaedics equipment. The study developed aims to find the unit-cell geometry and relative density for optimal mechanical performance in bending tests.

Previously, in Castresana Olleta [20] five unit cells were studied under compression tests by Finite Element Analysis (FEA). The Rhombitruncated Cuboctahedron (RTCO) and Truncated Octahedron (TO) cells simulations exhibited the best mechanical behaviour and will now be studied under bending.

Results from three-point bending FEA and experimental tests of 316L Stainless Steel samples, printed by SLM were analysed and compared, in order to understand the mechanical behaviour of the samples. The impact of using FEM as a tool to give a better understanding of possible scenarios was also studied. Moreover, FEA of 99,8% purity Iron was conducted and compared with FEA of Stainless Steel samples and FEA of two types of tissue bones examples to understand and predict the real application.

1.2 Thesis outline

This thesis is organized as follows:

In chapter 1 an introduction to the theme and objectives of the thesis is presented, defining the context and current problems in the area.

The chapter 2 establishes the areas of study, outlines previous research used to support the methodology and experiments, and highlights the novelty of this dissertation.

In chapter 3 information about procedures, methods and techniques used in the research is given.

In chapter 4 the data obtained from the numerical and experimental procedures is analysed.

Finally in chapter 5 conclusions are presented based on the collected data.

[1] Process of cartilage or mesenchymal cells transforming into bone. It maintains skeletal strength and structure.

2

State of the art

In this chapter, an introduction is presented to establish the context and the areas of study of this master's thesis. It identifies previous research used to support the methodology and experiments performed in this dissertation.

2.1 Medical and orthopaedic research

Orthopaedic issues lead to financial and social problems. This matter has increased globally, bringing the need to uphold medical and orthopaedic research. This provides a deeper understanding of health, diseases and treatments that can be used in orthopaedics [10, 21].

Moreover, it leads to better implementation of newer treatments and technologies in medicine, namely in the expertise of orthopaedics, improving patients' recoveries [22].

To conduct medical and orthopaedic research, different specialities have been introduced in orthopaedics, such as biomechanics, biomaterials, electrophysiology, molecular biology, critical care and surgical practices [21].

2.1.1 Fractures

The breakage of bone, resulting in anatomic discontinuity, is by definition a bone fracture. This condition leads to instability, which can compromise the function of the locomotor system [8].

Fractures are normally associated with other types and degrees of injury, affecting surrounding soft tissues and nerves, and can harm the normal behaviour of blood supply [8].

The most common causes of bone fractures are traumas, diseases, medical conditions (osteoporosis), and overuse injuries (normally caused by repetitive microtrauma, normally sports-related injuries) [23]. To describe and specify the type of fracture and its treatment, it is possible to use several data, such as the location, morphology, severity, age, size of the fracture and fixation stability [5, 8].

Fractures can be described as closed when the bone does not penetrate and damage the skin, or as

open, when there is penetration of the skin, which tends to provoke more damage in the surrounding soft tissues, with a higher risk of infections. Depending on the context of the fracture, it can be either stress fractures or overuse injuries, resulting from repetitive loading or simple fractures, which occur when a bending or twisting force is applied to the bone [8].

After the fracture takes place, the body reacts by self-healing. There are five biological mechanisms, being, inflammation, soft and hard callus formation, bone remodelling and regeneration [5, 6], presented in Figure 2.1. Before the inflammation process takes place, there is an anabolic stage, in which the local tissues increase in volume. This happens to act as a scaffold for cellular activity [6].

In the inflammatory process, the fracture is surrounded by blood clots to prevent infection, and there is the formation of a soft callus, where the cartilage forms around the fracture site [6]. To turn the bone hard again, the hard callus phase takes place, the osteoblast cells add minerals to create a new portion of the bone [6].

Last but not least, the two final phases are bone remodelling and regeneration where the new bone tissue replaces the old bone tissue.

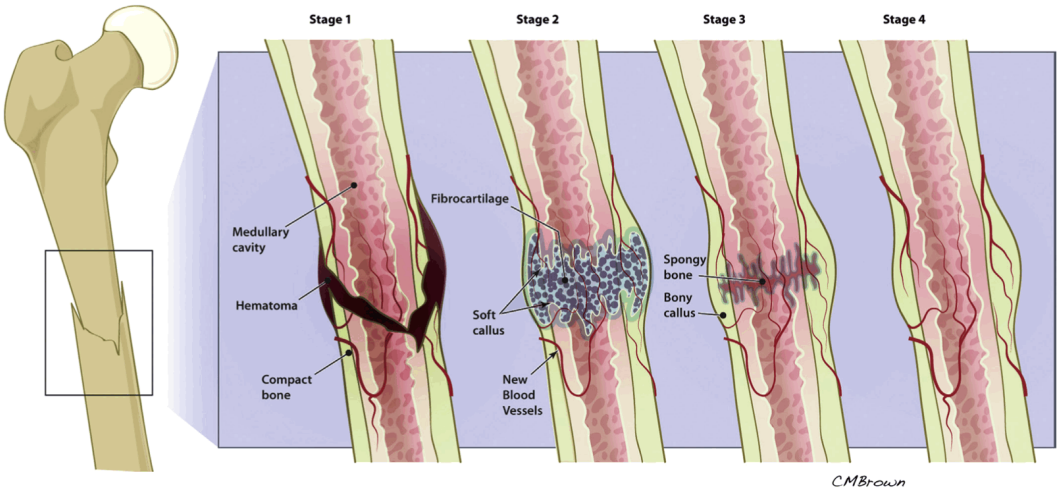

Figure 2.1: Stages of fracture repair. Stage 1: inflammation. Stage 2: soft callus formation. Stage 3: hard callus formation. Stage 4: bone remodelling and regeneration. Retrieved from Li et al. [24].

The healing of bones is highly dependent on the type of pressure, stress and fluid flow applied during recovery. Prendergast et al. [13] studied the healing time and behaviour of the different elements of bones influenced by fluid flow and tissue shear strain. Carter et al. [15] wrote about the hydrostatic stress history applied in fibrocartilage, cartilage, fibrous tissue and bone. Claes and Heigele [25] studied the effect of hydrostatic stress and the strain in the ossification [6].

Despite the five self-healing mechanisms mentioned before, (Figure 2.1), bone regeneration can be complex and insufficient due to the size of the fracture or the medical condition of the patient [12].

The Bone Tissue Engineering (BTE) field emerged from the necessity of going against the limitations

of conventional fracture treatments. The main objective is to regenerate bone flaws, through bioengineering, using scaffolds and target cells that promote growth [19]. Scaffolds and bone substitutes, promote the migration, proliferation and differentiation of bone cells for bone regeneration [12].

Besides BTE, there are also mechanical devices, such as plates. The main function of plates is to ensure stability by joining fractured bones. This medical device helps bone regeneration, and normally it is used simultaneously with enhanced bone regeneration. There are several types of plates depending on the zone to be healed and it can be permanent or not, depending on the case specifications and the treatment adopted [12].

Last but not least, surgery can be done to reduce space between bone fractures, and to remove fragments that were generated during an accident and that affect the normal behaviour of the bone. Surgery can also be done to add plates or prostheses to ensure mechanical support while the bone heals. After the treatment is complete, the plates can be removed, decreasing the chance of infections and making the process of healing faster and less painful for the patient.

2.2 Bone

2.2.1 Bone plates

There are several devices used to repair, substitute, support or heal bones. Two main pieces of equipment can be used: bone prostheses and plates. A prosthesis is used mainly to replace a missing bone or tissue that was lost due to accidents or disease [26, 27].

Depending on the trauma, the location and the size, different types of prosthesis can be used. There are several types of prosthesis, such as upper and lower limb, neural, retinal, maxillofacial, and ocular prosthesis [26, 27].

A plate has a different purpose compared to prostheses. A plate is a temporary device used to promote reconstruction and stabilization of bone fractures, to make the recovery easier and faster for the patient. These plates are applied with screws on both sides of the fracture and are typically made of Stainless Steel or titanium. Depending on the type of fixation and constraints of each case, different plates can be used. The most employed are Dynamic Compression Plates (DCP), Limited Contact Dynamic Compression Plate (LC-DCP) and Locking Compression Plate (LCP), presented in Figure 2.2 [28].

The size of the plates must be proportional to the bone fractures to withstand the stress generated during the patient´s motion [28]. The plates can be classified by geometry and function. Firstly, plates can be classified, depending on the geometry:

- DCP, a conventional plate that has compression holes, enables the screws to position and compress the bone. This diminishes the size of the fracture [29].

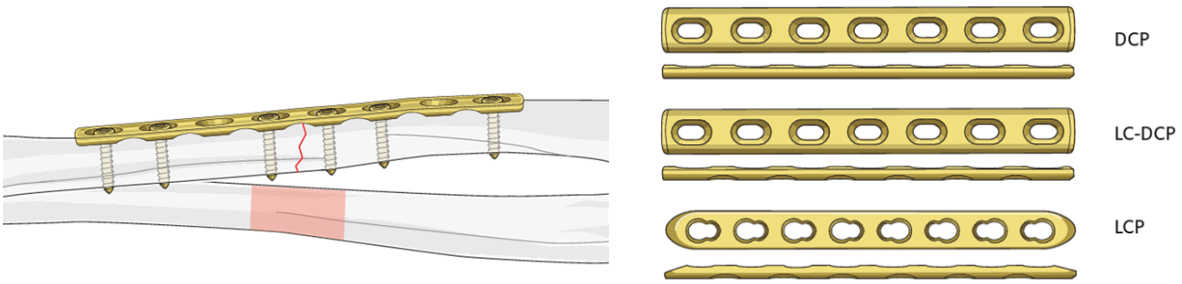

Figure 2.2: Fixation example of transverse fracture: open reduction, compression plating and different types of plates [28].

- LC-DCP has less contact with bone compared with the other plates, which helps circulation and, consequently the regeneration of the bone, it also minimises soft tissue irritation, uses screws that compress the bone to minimise the size of the fracture [29].
- LCP has "combi-holes" with conical geometry, the screws are positioned with a fixed angle, allowing the combination of locking and non-locking screws, it allows faster mobilisation of the patient during recovery [30].

Secondly, depending on the function, plates (Figure 2.3) can be classified by:

- Buttress plates or peri-articular plates, L-shaped and T-shaped, join the ends of long bones when fractured. Used normally in knees and ankles, places with large compression force [28].
- Neutralization plates are used to cover the fracture area and distribute the load evenly, increasing the fixation of the fracture site [28].
- Tension plates, normally wires that convert tensile force into compressive force. Bridging plates are used for multi-fragment fractures, connecting two pieces of healthy bone like a bridge [28].

2.2.2 Bone as a material

Bone is a natural composite material. These types of materials, by definition, are the junction of two or more distinct constituents at an atomic or larger scale that are not meant to be separated [7].

Normally, natural composite materials appear in nature and are not made or changed by man. This type of material tends to have different combinations of constituents and structures (for example, fibre with different directions) [31, 32].

As for bones, it is possible to observe different parts, the cortical and trabecular bone, that have different pore directions, densities, and bonds between constituents. This influences the mechanical behaviour of bones, owing to the dependence on their composition and structure [7].

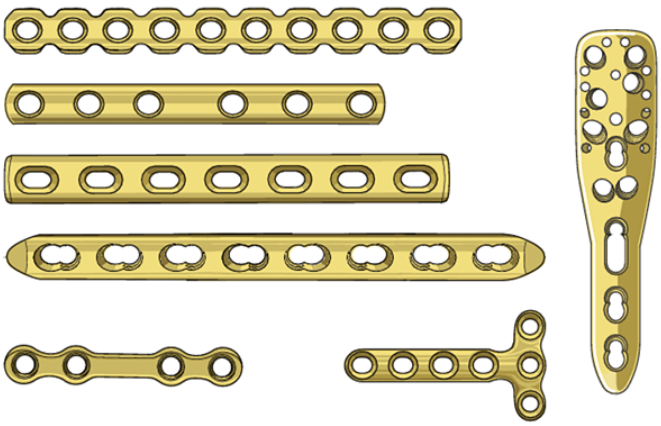

Figure 2.3: Some examples of plate designs [28].

Bones have several constituents. There are two types of constituents: organic and inorganic. Proteins, the main organic component, are about 60% of the total composition of bones, with 90% of collagen[1] type I and the remaining 10% being non-collagenous proteins. The inorganic part known as hydroxyapatite[2] takes about 40% of the bone volume. The collagen present has 35% of a flexible extracellular matrix and 65% is constituted of harder minerals, normally calcium and phosphate [33]. Collagen can absorb energy, while the harder minerals give stiffness to the tissues [7].

2.2.2.A Mechanical behaviour and properties of the bone

Studying the mechanical and chemical properties of bones contributes to clinical practices [34]. The mechanical properties can be affected by the characteristics of the patient, such as age, sex, anatomical location, load orientation, bone density, and bone diseases.

Mechanical properties of bones allow the protection of vital organs and support movement [34]. The cortical bone is mostly present in the outer part of the bone and the trabecular bone tends to be in the inner part of the bone [7].

One difference between the cortical and trabecular bones is the density. The density of a cortical bone is between 1800-2000 kg/m^3 and trabecular bone is between 200-600 kg/m^3 [7]. There are several types of densities: ash, relative and apparent density. The Ash Density (D_{Ash}), is used for studying the properties of the bones, and is calculated by Equation (2.1):

$$D_{Ash} = \frac{W_{Ash}}{V_R} \tag{2.1}$$

[1] Strong and fibrous protein that provides structure and elasticity to skin, muscles, bones, tendons, and other connective tissues in the body.

[2] Ceramic mineral made of calcium and phosphate, present in bones. It is used in protein purification, tissue engineering, and dental materials.

The calculation consists of dividing the Ash weight (W_{Ash}) by the real volume (V_R). The real volume measurement does not consider pore space, since Ash weight only accounts for inorganic minerals remaining after removal of organic matter, mainly water [35, 36].

The Relative Density ($\bar{\rho}$) is represented by the ratio of the wet weight of the bone (W_w) and the real volume of the bone tissues (V_R).

The Apparent Density (D_{Ap}) is the relation between the (W_w) and the volume of the bone tissues and pores present in the bone (V_T), expressed in Equations (2.2) and (2.3), respectively [37].

$$\bar{\rho} = \frac{W_w}{V_R} \tag{2.2}$$

$$D_{Ap} = \frac{W_w}{V_T} \tag{2.3}$$

The porosity of the trabecular bone can reach 80%, influencing the density [7], accounting for ρ = 1 - ϕ, where ρ is the density and the ϕ is the porosity. To study the porosity is important to understand the different porosities, such as the bulk, effective and surface porosity.

The bulk porosity (ϕ_B) is the overall porosity of a material, considering the voids and pores within the material, and it is the ratio between the total volume of open spaces or voids in a material (V_p) and the total volume of the material (V_M), including both solid's and pore's volume (Equation (2.4)) [38, 39].

$$\phi_B = \frac{V_p}{V_M} \tag{2.4}$$

The Effective Porosity is the total porosity that is interconnected and contributes to fluid flow and does not consider the isolated or non-interconnected pores in the material. The surface porosity exists on the surface of a material, normally irregularities, cracks, or voids and can influence mechanical strength, adhesion, and surface reactivity [40].

Several tests can be done to evaluate stiffness, strength and toughness, namely compression, tension, bending, fatigue, creep and torsion, so as to understand the mechanical behaviour of bones [7].

Through different mechanical tests, it is possible to obtain several data, such as yield stress, Young's modulus (E), stiffness (k) and the energy necessary to reach yield in a material, which confers the material its resilience. This can be represented mathematically by:

$$E = \frac{\sigma}{\epsilon} = \frac{F/A}{dl/l} \tag{2.5}$$

The stress (σ) is the force (F) divided by the cross-sectional area (A). The strain (ϵ) is the change in length, divided by the original length (L_0), defined by: ($Ln - L_0$)/L_0. Ln is the length after the deformation.

It is also possible to obtain the tensile strength and the flexural strength [41]. The energy absorbed by the material can be also studied, represented by the area of the curve until the ultimate stress [41]. The plots that are presented in Figure 2.4 demonstrate the different data that is possible to get from mechanical tests, showing the relationship between stress (σ) and strain (ϵ) [7].

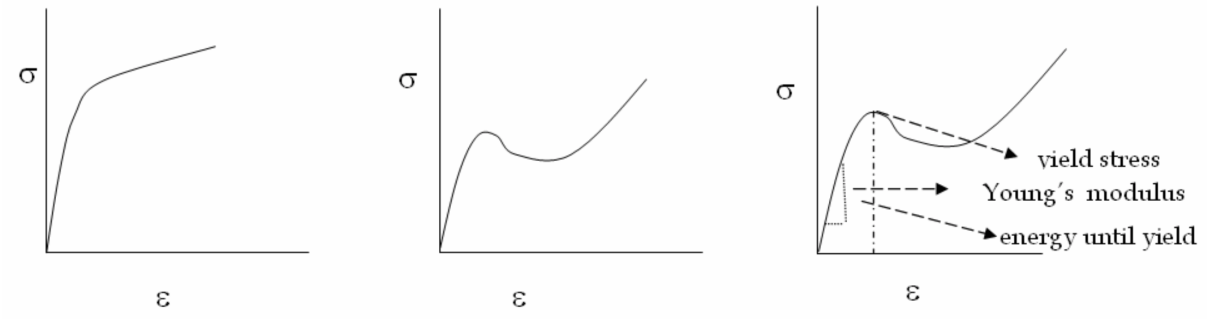

Figure 2.4: Stress-strain curves for healthy (left) cortical and (centre) trabecular bone and typical stress-strain curve (right) [7].

Since bones have different constituents, their mechanical properties will perform differently. The mineral constituents have mostly an elastic behaviour, while the plastic deformation is achieved through the collagen matrix. To better withstand possible fractures, the matrix between the mineral particles can create a barrier to crack propagation, allowing the dissipation of energy. In the bone, the bond of the matrix is mainly responsible for the toughness of the bone [7].

2.2.2.B Types of tissue bones

As mentioned before, there are two types of tissue of bones: trabecular, (otherwise known as cancellous bone) and cortical (otherwise known as compact or dense bone). The porosity is the main difference between the two types of bones, and that is why it is important to analyse their specifications to understand their mechanical behaviour and function [34].

Cortical has a porosity of about 5% to 15%, and the trabecular bone has a much higher porosity, between the values of 40% to 95% (Table 2.1) [34]. It is also important to note the arrangement of the lamellae[3] is different between the two types of bones, in which the cortical bones are organised concentrically and the trabecular bones are longitudinal [7]. As a result of different porosities, the cortical bone is normally situated in the outer part, making a thin shell, protecting the trabecular bone, which is usually towards the centre of the bones [34].

Cortical bone, as described previously, has different arrangements of constituents. Therefore, its

[3]Concentric rings of different bone matrix, providing the mechanical proprieties of bones. Made of organic and inorganic materials, such as collagen and hydroxyapatite crystals. There are three types of lamellae: concentric (circular and arranged concentrically around the central canal of each osteon), circumferential (wrapping around the circumference of the entire bone), and interstitial (irregularly shaped and fills in the spaces between osteons).

Table 2.1: Mechanical properties of bones [20].

Cortical bone			
Density [g/m^3]	1.5-2		
Porosity [%]	5-15		
	Load direction	Strength [MPa]	Modulus of elasticity [GPa]
Compressive properties	Longitudinal	190-245	14-28
	Transverse	30-170	-
Tensile properties	Longitudinal	130-190	7-25
	Transverse	40-60	-
Trabecular bone			
Density [g/m^3]	0.2-0.6		
Porosity [%]	40-95		
	Strength [MPa]	Modulus of elasticity [GPa]	
Compressive properties	1-12	0.1-0.4	
Tensile properties	2	6-14	

behaviour is anisotropic. The longitudinal direction has higher strength than the radial and circumferential directions. Cortical bones can also be considered as transversely isotropic material because there is similar mechanical behaviour in the circumferential and radial direction when under stress [34].

Trabecular bones have less density than cortical bones. The percentage of porosity is going to determine the mechanical behaviour. Moreover, since trabecular bones behave as an anisotropic material, the arrangement of the constituents is going to affect the behaviour as well [34].

2.2.2.C Bending properties of bones

The properties of the bone can be evaluated through several tests. Since bones deal with compressive and tensile stress simultaneously, to evaluate the structural properties, bending test can be done [42]. Furthermore, it helps understand the biomechanics of the human body and how it functions [43].

This test can be applied to several types of bones. However, it is more conducive in long bones, where repetitive loads involving flexure, torsion and compression happen [42]. The failure point tends to be on the convex side of the material.

Since fractures are a complex phenomenon, involving different types of stress (σ) and strain (ϵ) during movement, such as normal stress, shear stress, normal strain and shear strain, flexural tests can give important information [44].

Comparatively, the three-point bending tends to be more used than four-point bending as a result of the irregular geometry of the bone, making it more difficult to have four supports contacting the bone simultaneously instead of three. Usually, the size sample used happens to be more adequate to the three-point bending procedure [7].

During the three-point bending test, there are some assumptions made, such as the bones are cylinders, (Figure 2.5). Normally the data acquired by the bending test is yield-stress (σ_y), Young's-modulus (E), ultimate stress and ultimate strain, represented by the stress (σ) and the strain (ϵ) equations (Equation (2.6) and Equation (2.7)) [7].

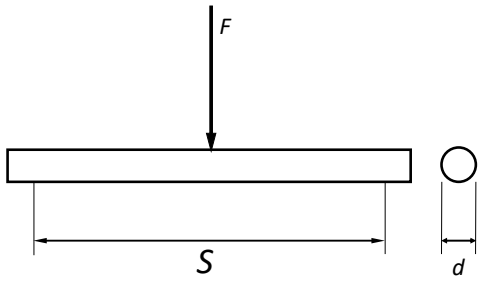

Figure 2.5: Schematic of three-point bending of bones. d - diameter of their cross-section; F - applied load and S - distance between lower supports.

$$\sigma = \frac{FS}{\pi \left(\frac{d}{2}\right)^3} \tag{2.6}$$

$$\epsilon = \frac{12 \left(\frac{d}{2}\right) \Delta l}{S^2} \tag{2.7}$$

2.3 Biomaterials

Biomaterial is described by the American National Institute of Health as "any substance or combination of substances, other than drugs, synthetic or natural in origin, which can be used for any period of time, which augments or replaces partially or totally any tissue, organ or function of the body in order to maintain or improve the quality of life of the individual" [4].

Biomaterials can be liquid, solid or gas and are engineered to be used in medical applications, such as implants (heart valves, intraocular lenses, ligaments or bone replacements) or medical devices (artificial hearts, biosensors or pacemakers) [4, 45, 46]. These materials can be of natural or synthetic origin and it is possible to find metals, ceramics, polymers, and composite [18, 45].

Biomaterials are normally used to replace or enhance organs or tissues present in the human body, having a therapeutic and diagnostic purpose. Biomaterials must be biofunctional and biocompatible, accomplishing their specific function without adverse effects on the organism, they must be blood compatible, nontoxic, noninflammatory, nonpyrogenic, non-allergenic and non-carcinogenic [4, 45, 46]. These obligations are documented by the International Standards Organization in ISO 10993 [47].

Biomaterials can be classified depending on their permanence on the body: they can be either resorbable materials, where material gradually releases the mass and is dissolved over time or non-

resorbable, staying permanently in the body [46].

Biomaterials can be active biomaterials (bioactive), reacting with the tissues, these types can be osteoconduction (allows the cellular growth along the surface of the material) or osteoinductive (stimulates the growth and the proliferation of tissues/cells). There are also inactive biomaterials causing almost null reactions with the surrounding tissues [18, 45, 46].

Depending on the function and reaction of the body to the material, biomaterials can be classified as biotolerant, bioinert, biodegradable and bioactive. Biomaterials have different requirements for different purposes, and the mechanical, physical, chemical, and biological properties are studied [18, 45, 46].

There are several types of biomaterials (Figure 2.6):

Biotolerant materials have a separation between the host tissue and the material, by a fibrous tissue (scar tissue). Despite being accepted by the host tissue, these materials are not inert to the host [18].

Bioinert materials do not react with surrounding tissues and body fluids and have high stability, they can have direct contact with organs and have a structural function [18].

Biodegradable materials are engineered to dissolve or disintegrate during usage, while in contact with organs or body fluids, the most common example is the surgical sutures [18].

Biocompatible or **Bioactive** materials interact with the tissue or body fluids without producing harmful responses [18].

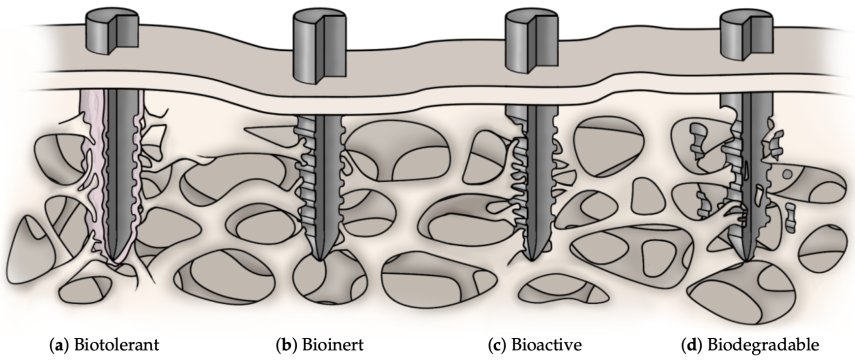

Figure 2.6: Biomaterial classifications explained [18].

2.3.1 Prostheses materials

Prostheses materials, depending on the function of the biomaterial used, can be orthopaedic (used in artificial bones, fracture fixation and bone grafts), cardiovascular (used in heart valves, pacemakers, catheters, grafts and stents), dental (used in orthodontics), soft tissues (used in reconstructive and augmentation) and surgical materials (used in staples, sutures, scalpels, surgical tools) [4, 45].

For orthopaedic implants and prostheses, metals are mostly used because of high stiffness, wear resistance, ductility, biocompatibility and thermal and electrical conductivity, allowing for load-bearing

applications[4, 18, 45].

Stainless steels (301, 304, 347 and 316L), titanium and titanium-base alloys (Ti-6Al-4V, TiAl4VELI, Ti6Al17Nb) are the most commercially available [4]. However recent studies have been suggesting the usage of Iron (Fe), magnesium (Mg) and zinc (Zn) for implants with biodegradable purposes [48].

Iron is naturally present in the human body, with an average of 3 to 4 grams. Iron has an important impact on oxygen transport, energy production, and DNA synthesis [49]. Its biocompatibility is, thus, inherent. Zinc and Magnesium are also possible, however have downsides such as non-suitable mechanical properties and non-suitable degradation rate, respectively [48]. The Young's modulus (E) of compact Iron is approximately 210 GPa, and through the manipulation of the density and geometry acquired by the material (making it a cellular material), the Young'smodulus (E) can be lower, making it possible to fit the bones' mechanical properties [48].

Stainless steel has in its composition chromium, which promotes a protective oxide layer (avoiding corrosion) leading to biocompatibility [45]. In the last few years, Stainless Steel has been altered by adding molybdenum and reducing the amount of carbon, enhancing ductility and making it easier to produce. This allows the wider implantation in medical devices, due to its properties and price [45]. However, the high amount of nickel (10-14%), can be harmful, causing tissue reactions and stress fractures, delaying the regeneration of organs [45].

Titanium is the most used material for implants. It is highly resistant to corrosion, due to its passivation layer formed by the presence of oxygen, does not create galvanic corrosion (contrary to Stainless Steel) and is biocompatible. However, titanium is difficult to process due to its hardness, and it is not antibacterial [45].

2.4 Cellular structures

Gibson and Ashby [50] were among the first to consider the concept of cellular structures of materials and described two types of cellular structures; foams (open or closed cell) and honeycombs. Materials with two or three-dimensional arrangements are considered cellular materials [16, 38].

Because of their geometry, they tend to have high values of mechanical properties, scaled to their relative density and compared to compact materials. Engineered materials have tailored geometries, making it possible to control the properties and mechanical behaviour of the structure (Figure 2.7) [16, 38].

Nowadays, cellular materials can be categorized in two main types of cellular structures: stochastic structures and non-stochastic structures (fig. 2.8) [17, 50]. Furthermore, cellular materials can have different morphologies. For example, the cells can be randomly oriented (foams) or have organised periodic repetition and randomly oriented (honeycombs and lattice structures). The shape and size of cells can also differ, or even be uniform or non-uniform [16, 37]. There are several applications and

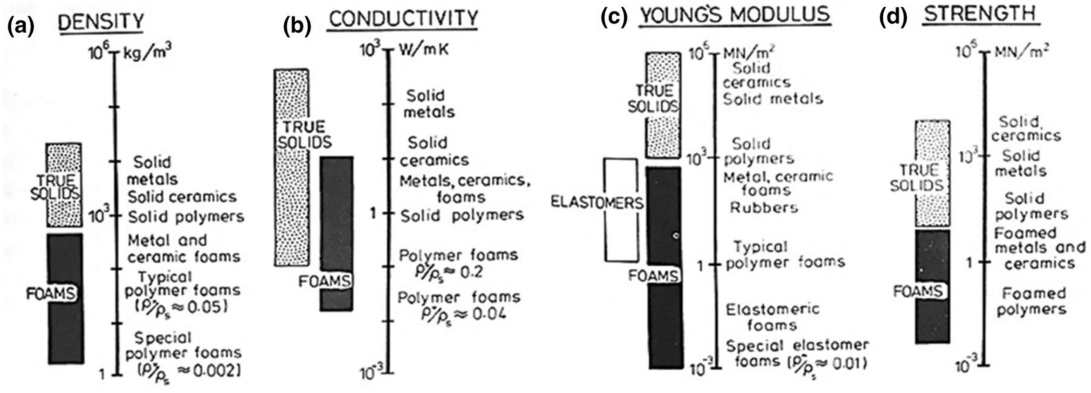

Figure 2.7: Comparison of foams with true solid materials in (a) Density, (b) Conductivity, (c) Young's modulus and (d) Strength [50].

multiple properties for each type of cellular structure (Table 2.2) [16, 38].

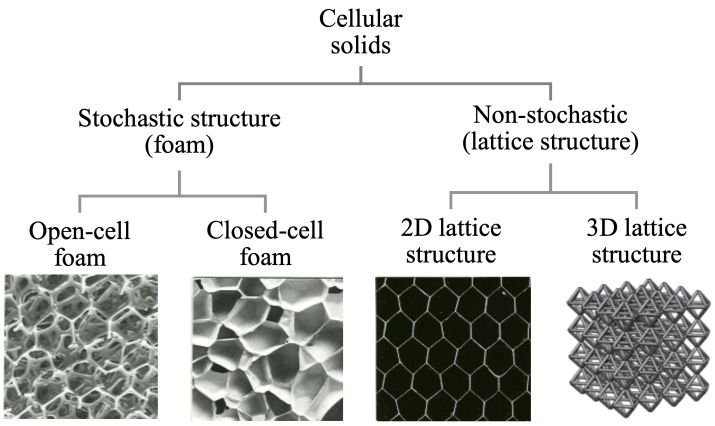

Figure 2.8: Categories of cellular solids [17].

2.4.1 Natural cellular materials

Natural cellular materials grow in nature. Some examples of natural materials are bone, honeycombs, wood and cork. These materials can have several structures and tend to be non-uniform. Materials with cellular structure have different mechanical properties from bulkier versions of the same material. [51].

The creation of new materials by mimicking natural cellular materials makes it possible to achieve high-performance applications [51]. In Table 2.2 various applications of cellular materials are given.

Table 2.2: Cellular materials applications [16].

Types of Cellular Structures	Applications
Foams	Energy absorbers, filters, silencers, flame arresters, heaters and heat exchangers, electro-chemical devices.
Honeycombs	Energy absorbers, biomedical implants, filters, sensors, actuators, vibration absorber or damper.
Lattice	Energy absorbers, heaters and heat exchangers, engine hood, biomedical implants, wings, gas turbine engine fan blades, vibration absorber, robotic system, spacecraft and aircraft structures.

2.4.2 Engineered cellular materials

Besides natural cellular materials, there are also cellular materials produced and studied by man, this type of materials are called Engineered cellular materials, and they can be made from a variety of materials such as polymers, metals, ceramics, glasses, and composites [50].

2.4.2.A Honeycombs

Cellular materials can be divided depending on the shape or patterns created by their structure. Honeycombs are described as structures with regular geometries with the same shape and sizes (fig. 2.9). The shapes of honeycombs follow well-defined geometric patterns, using either tetrahedron, triangular prism, square prism or hexagonal prism [16].

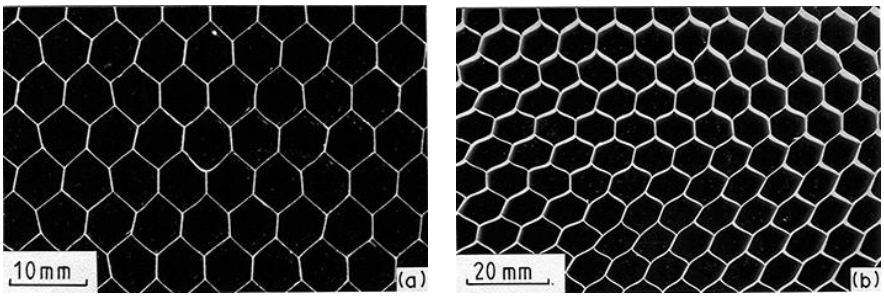

Figure 2.9: (a) Aluminum and (b) paper-phenolic honeycombs [50].

2.4.2.B Foams

Contrary to honeycombs, foam structures have irregular shapes and organisation. The foam structure is three-dimensional and can be divided into groups, open-cell, where there are only edges dividing the cells or closed-cell when the cells have walls between them, this type of foam can have cells partially closed or open [50].

The mechanical properties of both types of foams are different. In open-cell foams, there is wall

bending and axial deformation. In closed-cell foams, beyond bending and axial deformation, there is also edge contraction, mechanical stretching and in some cases enclosed gas pressure [50].

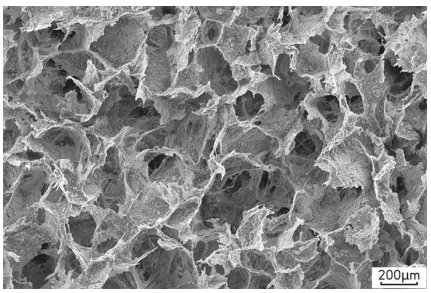

Figure 2.10: A mineralized collagen-GAG scaffold for regenerating bone. Microscopy by Biraja Kanungo [51].

2.4.2.C Lattice structures

The most recent group in cellular materials to receive attention is the lattice structures materials, characterised by their patterns of unit cells of complex geometries that can be either repeating and continuous or irregular having different sizes and topologies. These structures can be two or three-dimensional [17].

The geometries can have several designs such as Kelvin and rhombicuboctahedron, pyramidal, diamond cubic or octahedral [17]. Some of the geometries used are represented in Figure 2.11.

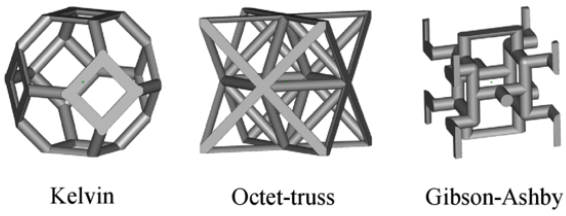

Figure 2.11: 3D unit cell structure examples [52].

Since lattice structures are engineered, the main difference between these structures and foams or honeycombs is the topology of the unit cells, which can be designed to have certain properties, depending on the application [16].

There are several types of patterns: direct patterning, where the pattern is repeated translationally; conformal patterning, where the unit cell follows a surface geometry when repeated; and topology optimization, where the distribution and organisation of the pattern and the cell are optimised [17].

Apart from the type of patterning, the lattice structures can also be classified into three groups, depending on the organisation and uniformity. Disordered lattice structures (when the unit cells are randomly allocated and have various sizes and topologies); periodic lattice structures (when the unit cell with the same shape and size is repeated uniformly); and pseudo periodic lattice structures or

conformal lattice structures (where the shape of the unit cell is the same, however, the size is different). The different classification schemes are represented in fig. 2.12 [16].

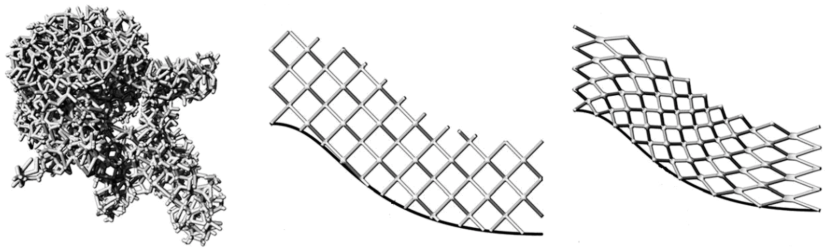

(a) (b) (c)

Figure 2.12: Classification of lattice structures: (a) random lattice structures; (b) periodic lattice structures; (c) periodic lattice structures [16].

The unit cells can be classified in bending and stretch-dominated architecture, depending on their behaviour when stresses are applied. The applications are different, as well, the stretch-dominated architecture is used when strength and stiffness are desired, while, the bending-dominated architecture is highly used when there is a need for energy absorption. The Figure 2.13 represents the different curves of stress-strain depending on the dominant architecture of the unit cell [17].

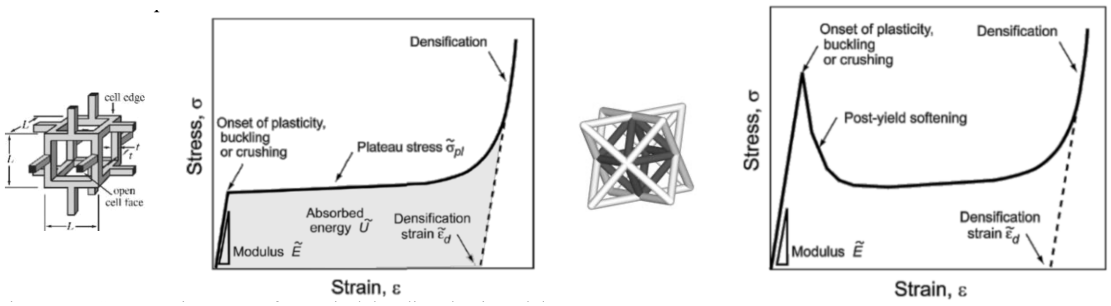

Figure 2.13: Stress-strain curve of (left) a bending-dominated and (right) stretch-dominated lattice structure [17].

To accomplish certain properties, the design is a fundamental part of the acquisition of the pattern and can be done in three ways, unit cell structure design, mathematical algorithm, or unit cell topology optimization. Some of these structures can be used for medical use and in other industries as well, due to their flexibility to meet most of the requirements needed [16].

2.5 Mechanical and Material Characterisation Tests

2.5.1 Three point bending testing

Bending testing determines the force, strength and stiffness of the material while bending. The main data acquired is the modulus of elasticity, bending stress and strain of the material [53].

Despite the existence of a four-point bending test, the most used is the three-point bending test. The configuration of the test consists of several supports with equal distance between them. In three-point bending, there are only three supports, while in four-point bending there are, as the name suggests, four supports. In both cases, the outer supports are below the sample, and the inner supports (responsible for the load applied) are above the sample [54].

Depending on the material and the geometry of the specimen, the distance between the support changes [54]. There are several standard documentation for bending tests such as ASTM D790-03, ASTM D7264/D7264M-07, and ISO 178:2019 [55–57].

2.5.1.A ASTM C393 - 00 [58]

ASTM C393 is a standard procedure that discriminates the bending test procedure for sandwich constructions (including continuous and discontinuous bonding surfaces) [58].

The beam sandwich is subject to a bending moment, through a load in the centre of the specimen applied perpendicularly to the surface of the specimen. The data acquired is the relationship between the force and deflection of the specimen [58]. The loading fixture, in the standard procedure, is represented in Figure 2.14, S is the total distance between the outer supports of the test, the load is represented by P_1 and is situated in the middle of the specimen [58].

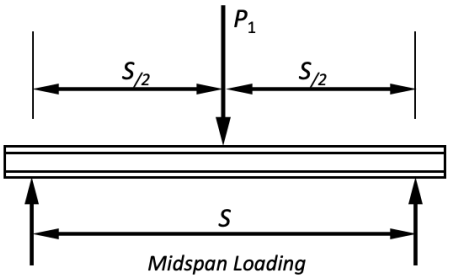

Figure 2.14: Standard configuration 3-Point Loading [58].

2.5.2 Compression testing

Compression tests aim to evaluate different materials under compression loads. The stress and strain are evaluated, these allow the determination of several properties such as strength, Young's modulus, and ductility [59–61].

These kinds of tests are important to analyse materials and structures that tend to be subjected to compressive loads during usage and anticipate some problems that might exist in the application or durability of the materials [62]. The ASTM E9–19 and ASTM E209–18 are standard documentation that can be used in compressive tests.

2.5.2.A ASTM E9

This document gives guidance on how to proceed with axial-load compression testing of metallic materials at room temperature, and the apparatus, specimens, and procedure specifications [62].

An axial compressive load is applied against the specimen, at the same time. The load and stain are recorded. The document should indicate the requirements that need to be accomplished, the surface finish, the flatness and parallelism, the gauge length location, the specimen measurement, cleaning, lubrication, and Testing Speed [62].

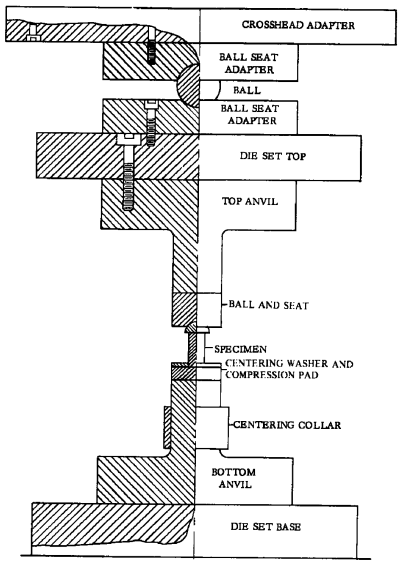

Figure 2.15: Example of Compression Testing Apparatus [62].

2.6 Finite element analysis

The FEM introduced by Clough in the early 1960s in "The finite element method in plane stress analysis" is used to solve numerical problems for engineering and physics purposes, with a finite number of elements incorporated into the model [63].

The numerical method consists of separating the model (domain) into individual sub-domains or finite elements, and as a result, vertices are created and used to obtain local solutions (Figure 2.16). When all the small sub-domains are brought together, the global solution is presented [64, 65].

Several steps need to be taken into account. Firstly the discretization, where the domain is divided into shapes, and they can be 1D, 2D or 3D. The elements can have several geometries, depending on the dimension, such as triangles, rectangles, squares, tetrahedrons, and rectangular or triangular prisms, represented in Figure 2.16. The smaller the elements the higher the accuracy of the results [64].

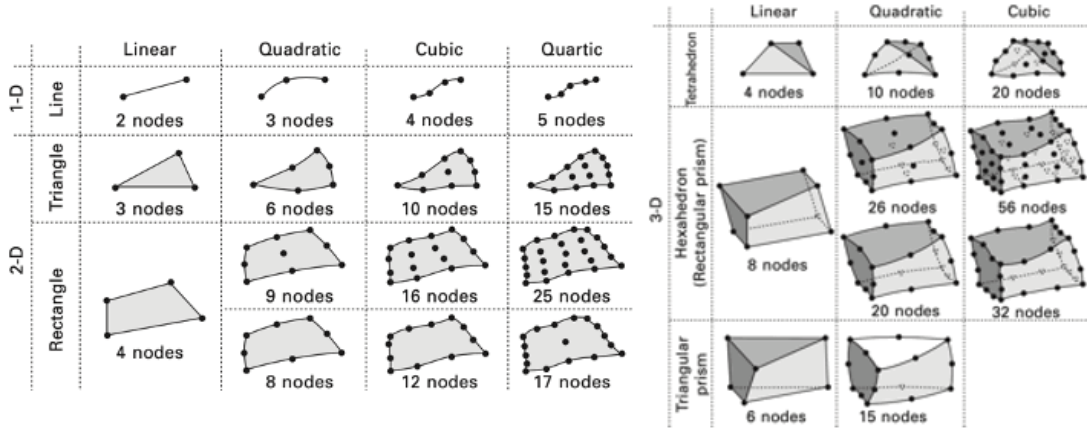

Figure 2.16: Common finite elements [65].

Secondly, the assembly is created, where different parts from a model are defined, and locally distributed. The interaction between parts is defined. After the assembly, the boundary conditions are imposed, referred to as loads, displacements, constraints, orientation, and several coefficients [64, 65].

To determine the solution, the numerical methods have a coordinate system, normally defined by x, y and z. The mesh is referred to as the domain, composed of several vertices and separated parts. The vertices are the points that define the local solution, known as nodes [64].

2.6.1 Simulia - Abaqus

Abaqus is a software that uses FEM to perform stress analysis. It was released in 1992, is part of SIMULIA, and has different software and interfaces. Abaqus CAE (Complete Abaqus EnvIronment) is the interactive interface that enables the user to manipulate and submit simulations with high complexity and accuracy creating FEM. Furthermore, Abaqus can also be operated by Python language [66].

Abaqus is used for mechanical studies and stress analysis, such as static, and dynamic analysis, with highly challenging and complex problems. Abaqus allows less production cost, validation of model and product, and reduction in experimental analysis and cost.

The modules presented in ABAQUS are the (1) part module, (2) property module, (3) assembly module, (4) step module, (5) interaction module, (6) load module, (7) mesh module, (8) job module and the (9) visualization module.

2.7 Additive manufacturing

In the 1980s, AM emerged as a new technology with various applications. This technology consists of adding the material layer-by-layer onto a surface. The combination of the different layers gives the final geometry designed by Computer-Aided Design (CAD). It is possible to generate and produce complex parts that could not be produced otherwise, through conventional manufacturing processes [16, 67–70].

This technology allows faster prototyping, reduces energy consumption and has less waste of material per product, it requires fewer inventories, since production can be done on demand [67, 69, 71], and is highly flexible due to its wide range of sizes and many kinds of material, such as metals, ceramics and polymers. The AM processes can have several categorizations, the most common are: material extrusion, binder jetting, direct energy deposition and powder bed fusion [16, 17, 72]. The Figure 2.17 presents several processes of AM.

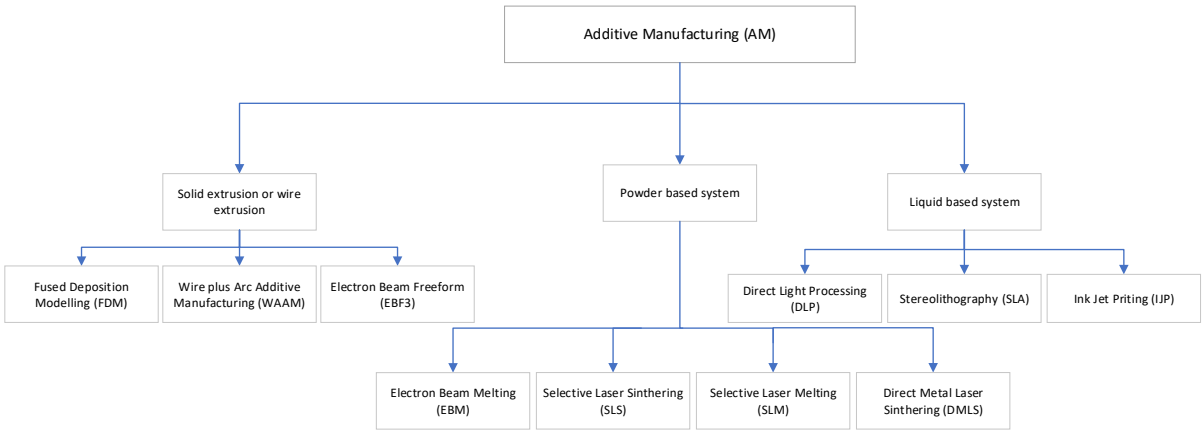

Figure 2.17: Classification of Additive Manufacturing. Adaptation from Rajaguru et al. [67].

Generally, there are several steps to manufacture a product through AM. First of all, there is a creation of a virtual model, that is afterwards converted into a Standard Triangle Language (STL). The next step is slicing and creating the supports [67].

Since the AM is good for complex geometries, and has the potential for the production of parts that need to be custom-made and also for mimicking certain materials and structures such as lattice

structures [16, 17], there are developments in 3D printable biomaterials to be applied in biomedical devices or even for the reconstruction of organs and tissues [73].

2.7.1 SLM - selective laser melting

The AM subgroup, Metal Additive Manufacturing (MAM) uses metallic materials. Powder bed fusion is a process that creates metallic parts by the fusion or deposition of metallic powder, normally deposited into a bed (surface from the printing machine). Heat is the main source for the fusion of the powder, normally by a laser or an electron beam. This technology requires an inert atmosphere or vacuum, because of the oxidation of the metal during the manufacturing process [68, 69]. SLM is one of the main technologies in Powder Bed Fusion (PBF), using laser to melt the metallic powder [74].

The layer thickness in SLM tends to be between the values of 30–90 µm. Despite all the advantages of AM and SLM, there is a chance of thermomechanical failure, because of thermal loading that can occur during production; thermal distortion, oxidation when the inert gas or vacuum is incorrectly applied; and solidification defects or deformation of intended geometries [68].

The applications of SLM are mainly in high-value constituents and engineered lattice structures [68]. Some of the materials that can be used in SLM are Stainless Steel, titanium alloy, cobalt chrome, nickel alloy and aluminium alloy [69].

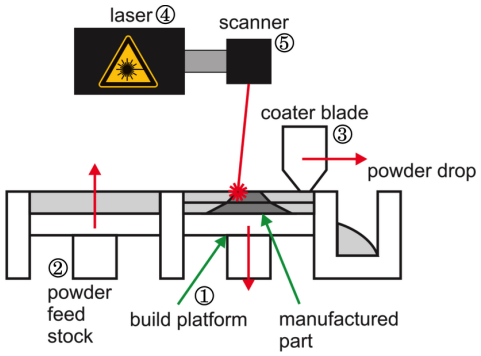

Figure 2.18: SLM schematic representation [75].

2.7.2 Electrical Discharge Machining (EDM)

EDM is mainly used to machine rigid and high-temperature alloys that are difficult to work with traditional technologies [76]. It uses electrical discharges promoting an arc between the tool and the workpiece, allowing the material to erode. This makes it a non-contact machining process, there is no physical contact between the tool and the workpiece [76].

The material used for the electrode tool is conductive (for example copper or graphite) in order to produce the discharges and the workpiece is also made of a conductive material (steel or titanium). In

most cases, a dielectric fluid is used to clean the eroded material [77].

Due to its technology, EDM is very precise, has very tight tolerances (2-20 μm), and can produce complex geometries and fine details. It is suitable for demanding applications such as aerospace, automotive, and medical [78–80].

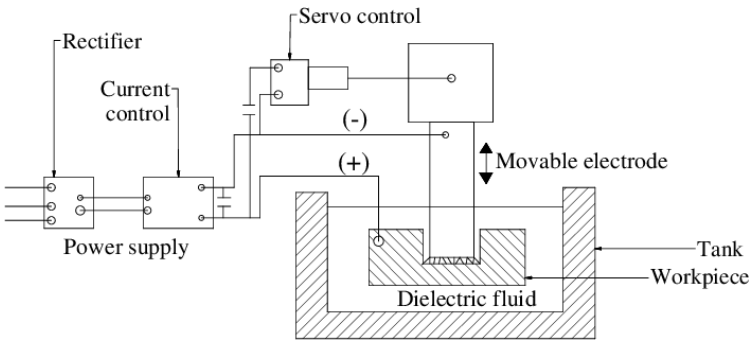

Figure 2.19: EDM schematic representation [81].

3

Materials and methods

The information about the procedures, methods and techniques used to conduct the research and analyse the data are mentioned in this chapter. The specifications and information of equipment, software and materials used are also indicated.

Since this dissertation aims to study the material, cell geometries and relative density applied in bone prosthesis under bending, the methodologies used to analyse the mechanical behaviour were FEM analysis and experimental Three-Point Bending (3PB). The final results obtained from each type of analysis were compared. The strategy followed for the development of the dissertation is divided into 6 main steps, presented in Table 3.1.

Table 3.1: Strategy by steps used to conduct the study.

1	2	3	4	5	6
Choice of the cell geometry	Specimens design	Convergence analysis (symmetry, mesh and friction coefficient)	Simulations (Fe, Stainless Steel and bone)	Experimental procedure	Analysis and comparison of results

The project's methodology and organization are presented in Figure 3.1.

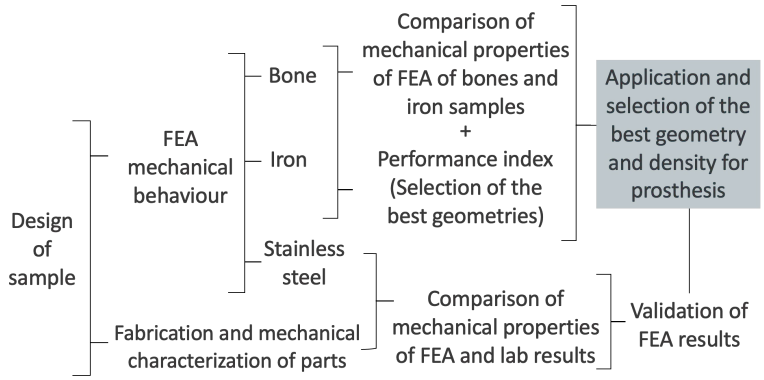

Figure 3.1: Project methodology.

3.1 Unit cell design

As mentioned in Chapter 2, the lattice structures are an arrangement of unit cells [82]. In this dissertation, the structures studied are made of uniform unit cells [83].

Five open-cell polyhedrons were previously studied by Castresana Olleta [20], by performing compression tests. The Cubic (C), Truncated Octahedron (TO), Truncated Cube (TC), Rhombicuboctahedron (RCO), and Rhombitruncated Cuboctahedron (RTCO), cells are shown in Figure 3.2.

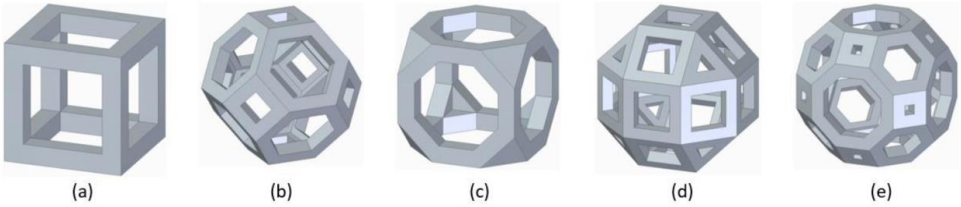

Figure 3.2: Unit cells selected for analysis in Castresana Olleta: (a) C; (b) TO; (c) TC; (d) RCO; (e) RTCO [20].

The five-unit cell topologies (Figure 3.2) used were based on Chantarapanich et al. [84] and considered the most appropriate for tissue engineering. The unit cells were selected based on several criteria, including mechanical behaviour, geometry assembly and manufacturing viability of 119 polyhedrons.

Each unit cell was made to fit into a cube with 3.5 x 3.5 x 3.5 mm (length, width and height, respectively). These dimensions were used by Sharma and Pandey in order to maintain the same size and replication patterns despite the different topologies being studied [85]. This allows a better correlation between the mechanical properties of each geometry cell.

Despite the capacity of the five cell geometries to present stable behaviour and the ability to mimic the cortical bone in high relative densities, only the TO and RTCO were able to embody the trabecular bone mechanical behaviour at low relative densities [20, 86].

The TO and RTCO were the only geometries to follow the engineering curve in elastic and plastic regions of both cortical and trabecular bone with constant relative density ($\bar{\rho}$). Presented in Table 3.2, comparing to the cortical bone the relative densities ($\bar{\rho}$) to best fit the engineering curve were 43.5% and 43.4% in RTCO and TO respectively, and in the trabecular bone were 4.5% RTCO and 3.7% to emulate the mechanical behaviour of bone.

Table 3.2: Best geometries and relative densities for compression tests [20].

	Cortical bone		Trabecular bone	
	Elastic zone	Plateau zone	Elastic zone	Plateau zone
C	30.7%	39.4%	x	
RCO	42.5%		x	
RTCO	43.5%		4.5%	
TC	31.8%	41%	x	
TO	43.4%		3.7%	

The unit cells selected to be analysed by bending are TO and RTCO (presented in Figure 3.2) since they had the best mechanical behaviour under compression in previous studies. Each cell geometry and arrangement of the lattice structures was designed in SolidWorks.

3.1.1 Sample geometry

According to the standard ASTM C393 - 00, each specimen must have certain dimensions [58]. The samples made by additive manufacturing follow the standard documentation and are mentioned as "Produced sample", in Table 3.3 (Figure 3.3). For the FEA, to save computational time, a "simplified version of the sample" in Table 3.3 (Figure 3.4) was designed. Furthermore, to avoid high computational cost, a symmetry convergence analysis was performed (Appendix A), and the model used in the final simulations is ¼ of the original geometry, ("¼ of sample" in Table 3.3 (Figure 3.5)). The ¼ models were submitted to a mesh convergence analysis, as featured in Appendix B.

Table 3.3: Sets of measurements used to study the unit cells.

	Measurements (a, b and c from fig. 3.4) [mm]	Use/Objective
1. Simplified version of the sample (Figure 3.4)	38.5 x 10.5 x 3.5	For the mesh and friction coefficient convergence analysis
3. ¼ of sample (Figure 3.5)	85.75 x 22.75 x 7	To save computational time in FEA, the sample is ¼ of the produced samples (the boundary conditions allow the FEM the analysis of ¼ as if it were the complete model)
2. Produced sample (Figure 3.3)	171.5 x 45.5 x 3.5	For the experimental bending test, produced by SLM

Figure 3.3: An example of the experimental bending samples RTCO-025-02 in Table 3.4.

To estimate the best boundary conditions in FEA, a simplified version of the TO and RTCO samples were designed, the measurements are indicated in Table 3.4.

The specimen design, for both final FEA and experimental testing, has 49 x 13 cells. The number of vertical cells and the surface height differ depending on the specimen, as detailed in Table 3.4. These dimensions were determined based on the standard ASTM C393 [58].

According to the Standard documentation, the measurements of the specimen follow several rules. The width is not less than 2x the total thickness (c in Figure 3.4), not less than 3x the dimension of a core cell (3.5 mm) and nor greater than ½ of the span length (S in Figure 2.14). The length must be higher than the support span length (S in Figure 2.14). The ASTM C393 stipulates that the facing

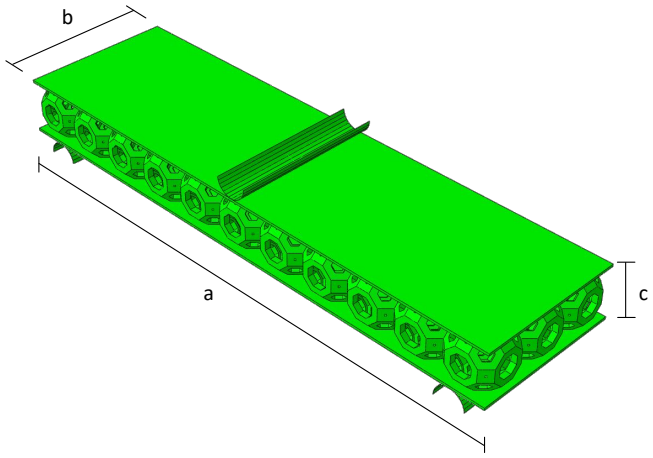

Figure 3.4: Example of sample assembly for preliminary simulation (RTCO).

thickness is determined by the test operator [58]. To determine the influence of the facing thickness in the specimens, different heights were taken into account, as in Table 3.4.

The relative densities ($\bar{\rho}$) used in this dissertation were 5%, 25% and 40% and were obtained by the Equation (3.1). The $\bar{\rho}$ is equivalent to the ratio between the volume occupied by the material (V_M) and the entire volume (V_T). The density is varied by changing the strut thickness in all directions.

$$D_R = \frac{V_M}{V_T} \tag{3.1}$$

For each geometry (for all relative densities, both TO and RTCO), two facing heights were studied:

- The first surface height was limited by the minimum resolution possible to be produced by the SLM machine at INEGI (which is 0.2 mm).
- The second surface height was limited by the thickness of the geometry edges, depending on the geometry's relative density ($\bar{\rho}$). For example, in TO a relative density ($\bar{\rho}$) of 0.406 has an edge thickness of 0.56 mm, therefore the face thickness is 0.56 mm.

The mechanical behaviour of samples without the influence of the outer surfaces is also studied. The presence of two rows of cells in the assembly of the specimens was analysed. The total specimen batch studied is indicated in Table 3.4.

A symmetry sensibility analysis was conducted (Appendix A). This analysis allows the simulations to be carried out using only ¼ of the geometry size without compromising the accuracy of the results, thereby saving computational time. Two examples of the symmetry parts can be seen in Figure 3.5

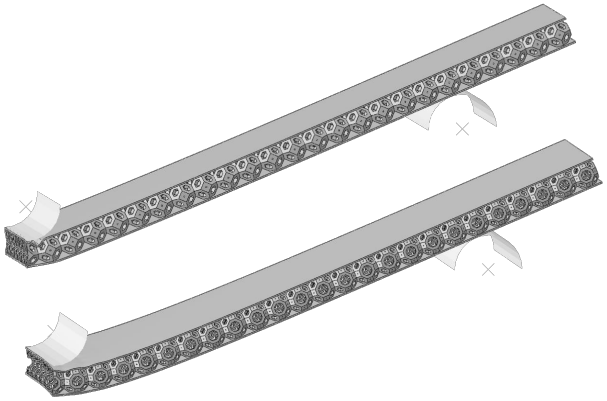

Figure 3.5: Example of bending FEA ¼ geometry (top) TO-025-02 and (bottom) RTCO-025-02 in Table 3.4.

Table 3.4: Samples' design parameters.

Preliminary geometries analysis					
	Number of cells	Dimensions [mm] (a,b,c) (Figure 3.4)	Relative density	Surface height [mm]	Designation
TO	11x 3 x 1	38.5 x10.5 x 3.5	0.253	0.4	0-TO
RTCO	11x 3 x 1	38.5 x10.5 x 3.5	0.253	0.4	0-RTCO
Final geometries analysis and Experiment procedure specimens					
	Number of cells	Dimensions [mm] (a,b,c) (Figure 3.4)	Relative density	Surface height [mm]	Designation
TO	49 x 13 x 1	171,5 x 45.5 x 3.5	0.406	0.2	TO-040-02
				0.56	TO-040-056
			0.253	0.2	TO-025-02
				0.4	TO-025-04
				0	TO-025-0
			0.054	0.2	TO-005-02
	49 x 13 x 2	171,5 x 45.5 x 7	0.253	0.2	TO-025-02-2
RTCO	49 x 13 x 1	171,5 x 45.5 x 3.5	0.400	0.2	RTCO-040-02
				0.79	RTCO-040-079
			0.253	0.2	RTCO-025-02
				0.53	RTCO-025-053
				0	RTCO-025-0
			0.050	0.2	RTCO-005-02
	49 x 13 x 2	171,5 x 45.5 x 7	0.253	0.2	RTCO-025-02-2

3.2 Material characterization

3.2.1 Stainless steel 316L

Compression tests were performed to obtain the mechanical properties of the material, inserted in the FEA software for the bending analysis, shown in Figure 3.6. The data was obtained by Nogueira et al. for the project "GradImp - Implantes biodegradáveis em ferro poroso obtidos por fabrico aditivo", FCT PTDC/CTM-CTM/3354/2021 [87].

The compression test was performed according to ASTM E9-19 (ASTM, 2019) [88], the material was Stainless Steel 316L and the powder chemical composition followed the ASTM F3184 - UNS S31603 / ASTM A276 [89, 90].

The samples were cylinders with 17.5 mm of radius and 32 mm of height, produced by SLM, the compression tests were performed in an Instron SATEC 1200 with a load cell of 1200 kN. The experiments were carried out in C1-type specimens at a displacement rate of 2.1 mm/min.

To obtain the stress-strain curve, the values for ε_e, σ_e, ε_t and σ_t (engineering strain, engineering stress, true strain and true stress, respectively) are calculated (Equations 3.2-3.5).

$$\varepsilon_e = \frac{\Delta L}{L_0} \tag{3.2}$$

$$\sigma_e = \frac{F}{InitialA} \tag{3.3}$$

$$\varepsilon_t = \ln(\varepsilon_e + 1) \tag{3.4}$$

$$\sigma_t = \sigma_e(\varepsilon_e + 1) \tag{3.5}$$

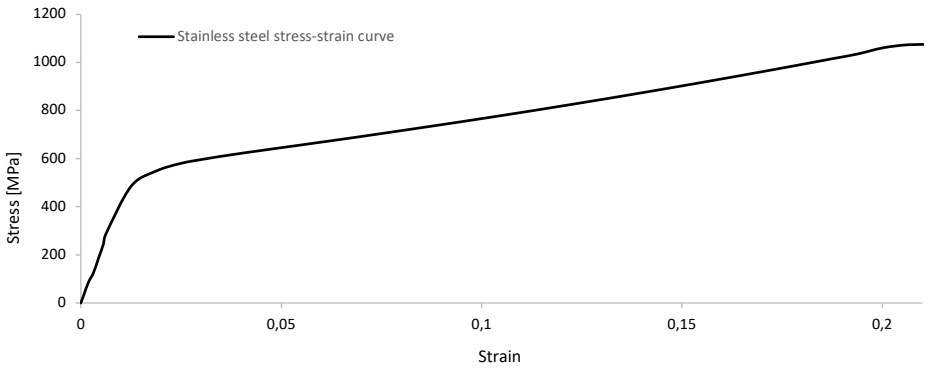

Figure 3.6: Stress-strain curve of Stainless Steel 316L.

3.2.2 Iron

In Chapter 2, a review of the literature revealed that Iron was a promising material for biodegradable bone implants. With this in mind, 99.8% purity Iron was used in a set of FEA simulations that included all the geometries before mentioned.

According to ASTM E8-16a and E9-19, tensile and compression tests, respectively, were performed. The mechanical property data used for FEA model was obtained experimentally by Salama et al. and by Neves Manuel [48, 91]. As a result, the obtained mechanical properties were introduced into the FEA model for the bending analysis (Figure 3.7). The material characteristics of Iron (99.8% purity) from Goodfellow Inc., Cambridge, UK, were acquired from a machined rod and experimentally assessed by

compression tests performed in an Instron SATEC 1200 with a load cell of 1200 kN. The experiments were carried out in C1-type specimens at a displacement rate of 2.5 mm/min. To obtain the stress-strain curve the equations 3.2-3.5 were calculated.

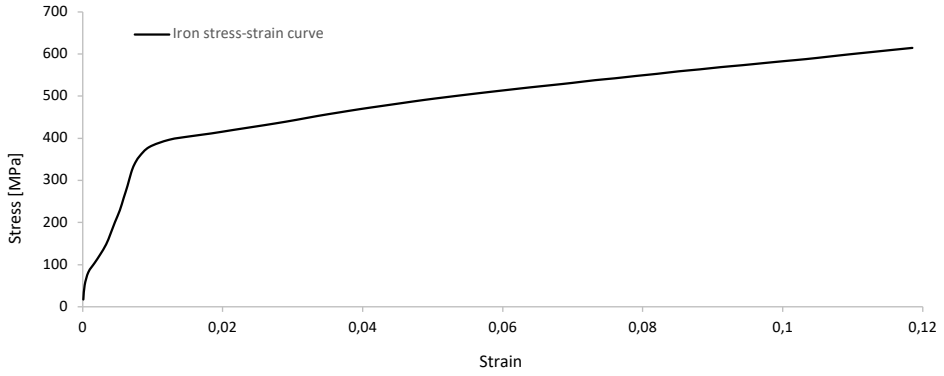

Figure 3.7: Stress-strain curve of Iron 99,8% purity.

3.3 Finite element analysis

For the numerical 3PB test, the FEA software used was ABAQUS 2022 by Dassault Systems, Waltham, MA, USA. The package used more specifically is ABAQUS/Standard and the chosen type of analysis is dynamic implicit in order to be closer to an experimental 3-point bending test, allowing to set a constant displacement and velocity to the inner support responsible for the load applied [54].

In this dissertation, the units chosen in ABAQUS software were millimetres [mm] for distance, seconds [s] for time, and Megapascal [MPa] for stress.

To create the simulations several steps, designated by “modules” in ABAQUS (Section 2.6.1) were followed. The **parts** were created in SolidWorks and imported to FEA software. The characteristics of the geometries used in all of the simulations are given in Section 3.1 and the measurements used are presented in Table 3.4. A total of 28 models were created, according to each geometry and material.

The parts created as the loading pins of the bending test machine were modelled as ”rigid surfaces” based on their real geometry. The “rigid surfaces” are stiffer than the specimen, no matter the loads and forces applied will not deform. All “rigid surfaces” have the same size and curvature, having 10.5 mm of diameter and longitudinally 45.5 mm, represented in Figure 3.8.

The data used in FEM analysis for the **properties** of the materials is given in Table 3.5 and Table 3.6 for the simulations of 99,8% pure Iron and Stainless Steel (SS), respectively. In the software, these properties were assigned to each part, and all the data was input in the ”Edit material” box dialogue, in Figure 3.9, where the density and the elastic regime (Young’s modulus and Poisson’s ratio) and plastic regime (yield stress and plastic strain) were attributed.

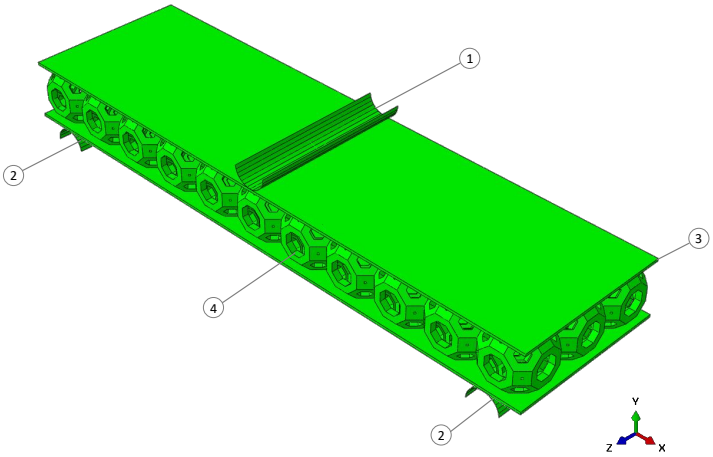

Figure 3.8: Example of sample assembly of the test parts and location of supports, (1) loading cylinder, (2) support cylinder, (3) sample surface and (4) sample cells.

Table 3.5: Properties considered for the computational model, regarding the Stainless Steel [91].

Density [g/cm^3]	Poisson's ratio	Young's modulus [MPa]	Yield stress [MPa]	Ultimate tensile strength [MPa]
7,9	0,3	194800	448	695

Table 3.6: Properties considered for the computational model, regarding the Fe of 99,8% of purity [91].

Density [g/cm^3]	Poisson's ratio	Young's modulus [MPa]	Yield stress [MPa]	Ultimate tensile strength [MPa]
7,2	0,29	204000	350	614

The ABAQUS **assembly** is represented in Figure 3.8. In each model, the assembly is composed of the specimen being analysed and the loading cylinders. The loading cylinder located in the middle of the specimen is the loading bar, where the displacement is applied vertically (y-axis) against the specimen. The lower supports are located in the outer part of the specimen, both at an equal distance of 64 mm from the centre, exemplified in Figure 3.8. To save computational time, ½ and ¼ symmetry models were studied, and the results from the convergence analysis (in Appendix A) allowed the modification of the assemblies for ¼. An example is given in Figure 3.10.

Since the conditions are constant throughout the simulation, only one **step** was defined in to the model. The time period of 660 seconds was chosen according to the standard ASTM C393 - 00 [58] (Section 2.5.1.A), assuring the velocity of 0.03 mm/s. "Nlgeom" was turned on. To reduce divergence the "automatic stabilization" was selected.

The increments chosen were based on the values given by the tool "mesh verify" and the capacity of the software to converge. The maximum increment size is 1000 and the initial and minimum increment size are 0,01 and 1×10^{-1}, respectively. The rest of the variables used are default from ABAQUS.

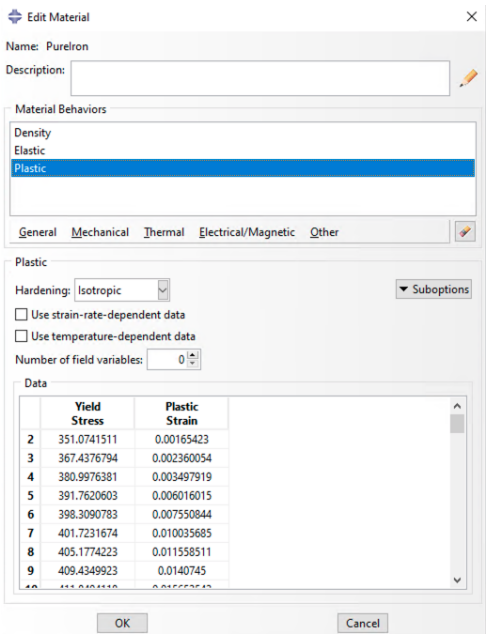

Figure 3.9: Edit material box dialogue - Abaqus.

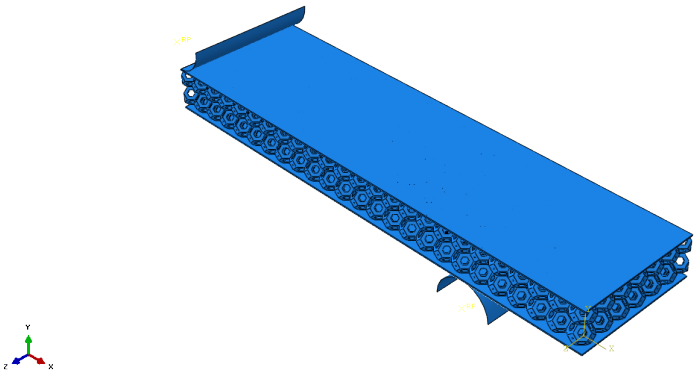

Figure 3.10: Example of sample assembly of ¼ part location supports (model presented is TO-025-02-2).

To collect the data, every 10 seconds outputs were requested. Additional points were requested at the beginning of the simulation (being at 18, 36, 54, 72 and 90 seconds) to obtain more information about the elastic regime. The field output variables requested were stress components and invariants (“*S*”), plastic strain components (“*PE*”), equivalent plastic strain (”*PEEQ*”), plastic strain magnitude (”*PEMAG*”), logarithmic strain components (“*LE*”), translations and rotations (“*U*”), translational and rotational velocities (”*V*”), reaction forces and moments (“*RF*”), concentrated forces and moments (”*CF*”), contact stresses (”*CSTRESS*”), Contact displacements (”*CDISP*”).

To have the expected response of the **interaction** between parts, the penalty method was used to model the tangential behaviour, in which a friction coefficient of 0,2 was used. The study to determine the best friction coefficient is presented in Appendix C. Additionally, in the normal behaviour method, the

”hard contact” was selected in order to avoid the overlapping of surfaces during the bending process. The parts have surface-to-surface contact interactions. All the supports had tangential contact with the specimen (presented in Figure 3.11).

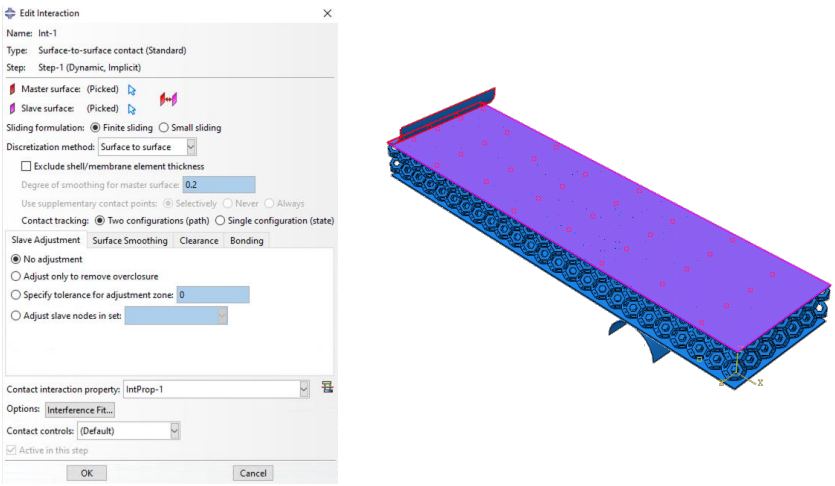

Figure 3.11: Example of step interaction and respective assembly.

Several **boundary conditions** were assigned to the model. ”Encastre” was attributed to the lower supports. This option removes all of the degrees of freedom in the boundary conditions since these are static. Therefore, there is no movement applied.

Displacement of -22 mm in the y-axis direction was applied to the upper loading bar, assuring the velocity of 0,03 mm/s, mentioned in the standard ASTM C393 - 00 (Section 2.5.1.A). Being the model ¼ of the original geometry, used in the simulations, symmetry boundary conditions were applied, exemplified in Figure 3.12, assuring the symmetry of the model.

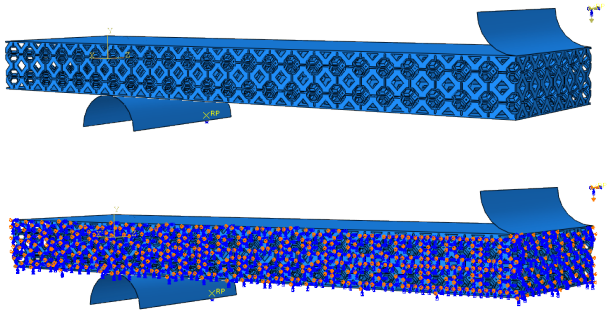

Figure 3.12: Representation of boundary conditions location in the model and sample symmetry cut.

All the models were meshed with quadratic tetrahedral elements (C3D10) (Figure 3.13) with an average mesh size of 0.4. The **mesh** size was chosen based on a sensitivity analysis detailed in Appendix B. The supports are meshless as they were modelled as ”rigid bodies”.

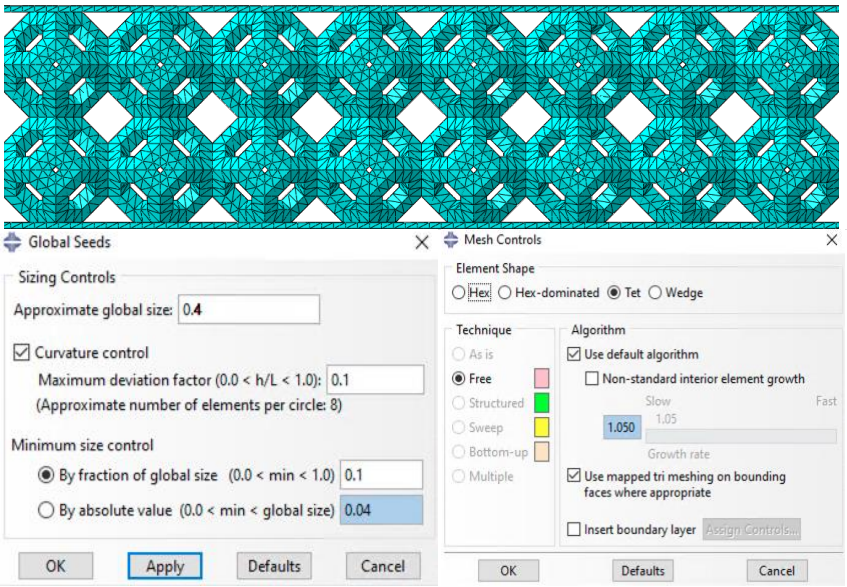

Figure 3.13: Mesh size and global seed and element shape toolbox.

To finish the simulation process, the job was submitted, and subsequently, the results of the analysis were shown in the **visualization module**. To analyse and compare the results from the different simulations and experimental work, the output variables presented in the visualization module were interpreted. For the FEA of bones, the same methodology was applied. The values of reaction force (RF) and the displacement ($U, U2$) were collected to obtain the force-displacement curve and consequently calculate the absorption energy (E_a) and stiffness (k). The von Mises stresses ($Primary : S, Mises$) were studied in order to compare the stress levels and the magnitude between structures. To detect and quantify the permanent plastic deformation, the plastic strain component ($Primary : PEandMaxPrincipal$) was studied.

3.4 Experimental procedure

3.4.1 Sample manufacturing

The Laser M2 Series 5 metal printing system from GE Additive produced the test samples. The technique used was SLM, which allows the production of the samples through additive manufacturing, explained in Section 2.7.1.

An example of a SLM printed sample is presented in Figure 3.3, and the measurements of all samples are indicated in Table 3.4.

The equipment has a dual-laser system with 1 kW combined with 3D optics with 70 – 500 μm spot size and a maximum speed of 4.5 m/s. The layer thickness ranges between 25 - 120 μm, as shown

in Figure 3.14. To prevent oxidation and safety hazards, the machine has a gas flow system allowing an inert nitrogen atmosphere. The chamber dimensions where the samples were manufactured are 245 x 245 x 405 mm, and the temperatures while operating were between 18 and 25 ºC [92]. The software platform used was Amp™, GE's developed by the GE Additive. The machine presented belongs and was operated by INEGI from Faculdade de Engenharia da Universidade do Porto.

Figure 3.14: SLM equipment - Laser M2 Series 5 from GE Additive [92].

3.4.2 Sample preparation - EDM

To give the samples the proper finishing, electrical discharge machining was used, this technology is explained in Section 2.7.2. When printing via SLM, there is a need to use supports (Section 2.7.2), to get the proper sample geometries and dimensions. EDM is used to remove the supports created. This excess of material in the samples would make it impossible to carry out the bending test and the results could not be compared with FEA since the samples would not be representative of each other.

The machine used was a Charmilles Robofil 190 (Figure 3.15) from the Núcleo de Oficinas (NOF) at Instituto Superior Técnico [93]. The machine uses deionized water as the dielectric liquid, and its power source is Isopulse 80 Amp. The samples were machined in a 200 by 200 mm working area.

All the samples were photographed after the EDM treatment as well as the removed parts in order to further analyse and understand the impact on the mechanical behaviour of the structures. The measurements of the samples after being machined are presented in Table 3.7.

Figure 3.15: Charmilles Robofil 190.

Figure 3.16: EDM post-processing fragments (1) RTCO-025-02-2 samples (2) rows of cells that were excessively cut (3) support used while printing the sample.

3.4.3 Three-point bending test

The bending testing was done in the Instron 3369 universal mechanical testing machine, located in Laboratório de Mecânica Experimental – DEM, Instituto Superior Técnico.

The displacement induced was -22 mm vertically. Three span bars with 10,5 mm of diameter were used. Two of them, used as support, had a distance of 64 mm from the sample´s centre and were static. The span bar located on the upper centre, moved vertically in order to apply the displacement required, presented in Figure 3.17. All of the conditions imposed are equal to the FEA analysis.

The data was obtained by *Instron Bluehill Universal* software. Reaction Force-Displacement curves were obtained in each test. Both parameters were measured by the machine, the Reaction Force (RF) was measured by the machine load cell and the displacement through the cross-head cell. Since the specimens did not have a visible failure moment, the tests were terminated when the force-displacement curve started to decline, after getting the maximum reaction force point present in the curve.

Table 3.7: Sample measurements after EDM finishing (a,b,c measurements represented in Figure 3.4).

	RTCO		
Measurements (mm)	a	c	b
RTCO-0.05-0.2	170,2	4,01	45,52
RTCO-0.25-0	170,5	3,63	45,4
RTCO-0.25-0.2	170,95	3,97	45,43
RTCO-0.25-0.4	171	4,45	45,46
RTCO-0.25-0.2-2	170,9	7,51	45,5
RTCO-0.40-0.2	170,9	3,97	45,47
RTCO-0.40-0.56	170,8	4,76	45,46

	TO		
Measurements (mm)	a	c	b
TO-0.05-0.2	170,95	4,03	45,46
TO-0.25-0	171	3,56	45,36
TO-0.25-0.2	170,9	3,98	45,21
TO-0.25-0.53	170,9	4,63	45,49
TO-0.25-0.2-2	170,8	7,49	45,42
TO-0.40-0.2	171	3,97	42,51
TO-0.40-0.79	170,95	5,14	45,59

Figure 3.17: Instron 3369 in the bending and compression test of the samples.

3.4.4 Data processing and sample characterization

To collect and analyse the data several software were used. For the FEA, the ABAQUS Visualization was used to gather all the data from the simulations, and the parameters obtained from the *.ODB* file for each sample were: Reaction Force and Displacement as a function of time.

For the experimental procedure of the bending test, the software Bluehill Universal was used, the parameters collected were displacement and the applied force on the samples, related to time.

In order to get the final analyses and to take some conclusions from the FEA and experimental results, Microsoft Excel was used. This software was able to gather all the information and compare several data, creating force-displacement curves for each sample and model.

Through the curves, several mechanical properties were obtained, such as stiffness (k, slope resultant from the force-displacement curve), and absorbed energy (E_a, force-displacement curve area).

4

Results and discussion

This chapter presents and examines the data obtained from the numerical and experimental procedures. The force-displacement plots from bending testing (numerical and experimental) are presented and analysed, showing the relationship between force and deflection of the material. The stress-strain plot will not be analysed, since the material does not assume a uniaxial load behaviour [94–98].

The data from the different structures were analysed to draw conclusions about the mechanical behaviour of both cell types. Firstly, a computational model was validated and presented. Secondly, the mechanical behaviour of the different geometries, with different relative densities, outer surface heights and unit cells were compared. Performance indexes were analysed. Lastly, the structures are compared with data from bone tissue obtained through two additional simulations.

The results are presented through the different types of analysis. In each subchapter to analyse the results, several methodologies were used. In FEA the .odb file gives a scheme of colours representing the stress. Laboratory photographs were taken in order to analyse and correlate local deformations. Force-displacement curves and tables were organized in Microsoft Excel.

The Table 4.1 presents the data used in each subchapter of Chapter 4. The data analysed was from the set of samples, presented in Table 3.4, taken from the FEA models and from SLM printed samples, for both materials (Stainless Steel and Iron) and for both cells (RTCO and TO).

Table 4.1: Organization of files, documents and results followed for the results and discussion of results.

		Material	
		Stainless Steel	99,9% purity Iron
FEA Abaqus	Visual representation of stresses and deformations (.odb)	2. Comparison between different cell geometries - RTCO and TO	-
	Force - Displacement curve (excel)	1. Computational model validation 2. Comparison between different cell geometries - RTCO and TO 3. Comparison between different densities, surface heights and stiffness	2. Comparison between different cell geometries - RTCO and TO 4. Comparison of FEA models - Iron specimens and bone
Experimental Bending Test	Visual representation of deformations (photography)	2. Comparison between different cell geometries - RTCO and TO	-
	Force - Displacement curve (excel)	1. Computational model validation 3. Comparison between different densities, surface heights and stiffness	-

4.1 Computational model validation

The first analysis, the computational model validation was carried out to ensure the validity of the FEM model and to understand the accuracy of the results obtained [99–101]. This process consists of testing a computational model to ensure its reliability and to simulate as close as possible the real-world system.

In order to obtain the validation, a comparison between the results of the model and experimental data is performed and analysed [99–101]. The data used was the Stainless Steel simulation and the results from the experimental bending testing of one of each Stainless Steel samples. For statistical evaluation, at least three samples of each geometry would be preferable. However, due to limited production capacity and a restricted time frame, two samples of each geometry were produced. Only the best sample of each geometry was chosen for this evaluation. Nevertheless, both samples of each geometry had the same mechanical behaviour qualitatively and the E_a and MRF values obtained were very close.

The validation was based on the error factor that was calculated between the absorbed energy obtained in FEA and in the laboratory experiments, for each geometry (Equation (4.1)).

$$\text{Error}(\%) = \left| \frac{E_a FEA - E_a LAB}{E_a LAB} \right| \times 100 \tag{4.1}$$

The relative error values presented in Table 4.2 ensure the credibility of the computational model, according to the analysis and determination of acceptable relative error percentages for computational model validation studied by Liu et al. [102]. The values presented in Table 4.2 are in the range of acceptable values since only four samples are above 10% relative error and are all below the error percentage studied by Liu et al. [102]. Note that the force-displacement curves are similar (Figure 4.1 and Figure 4.2).

Table 4.2: Relative error factor calculation for computational model validation.

Geometry	RTCO							TO						
Relative density [%]	5	25				40		5	25				40	
Surface height [mm]	0,2	0	0,2	0,4	0,2-2	0,2	0,56	0,2	0	0,2	0,53	0,2-2	0,2	0,79
E_a FEA [J/mm^2]	5657	4546	20004	38294	52924	25650	59224	2980	2513	14335	47930	49350	18197	76712
E_a FEA [J/mm^2]	5351	5101	19913	37696	52782	25608	57083	2141	2958	14809	45513	46569	14343	71939
Relative Error [%]	5,7	-10,9	0,5	1,6	0,3	0,2	3,8	39,2	-15,1	3,2	5,3	6,0	26,9	6,6

Since the specimens are SLM produced, there are many factors to take into account owing to the limitations of AM, that are not considered by the FEM software, making the results slightly different [102–104].

In most cases, the results of the energy absorption from the computational model were higher than the results from the experimental bending test. This is considered common because, despite the optimizations that can be done when producing an additive manufactured part, the specimens when printed

are prone to have defects, such as porosity, unsintered or unmelted powder in the interior of the structures and finishing defects, such as roughness and bad cohesion of layers and FEM does not account for that.

Furthermore, SLM technologies produce the specimens layer by layer, making the geometries sectioned into horizontal layers, contrary to FEM which assumes a bulk structure without layers or imperfections. Since FEM analysis assumes perfect conditions, the parts emulating the specimens are prone to have better mechanical behaviours. Consequently, a slightly different mechanical behaviour is seen.

The behaviour of the specimens with the lowest relative density and lowest surface heights are more uncertain than those with a higher relative density and height of the outer surface, present in Table 4.2 and Figure 4.3.

All specimens have higher energy absorption values in the computational model, apart from the specimens with no surfaces in both TO and RTCO geometries, in Table 4.2, Figure 4.1 and Figure 4.2. The lack of surface makes the cells directly in contact with the supporting bars from the flexural equipment. In the experimental procedure with the RTCO and TO of 02-0 (without surface), there was slippage of the sample, while in the simulation due to the interactions and the constraints applied in the software. The slippage is substantially lower than in the experimental procedure, and this justifies the lower energy absorption values in the computational model than in the experimental procedure.

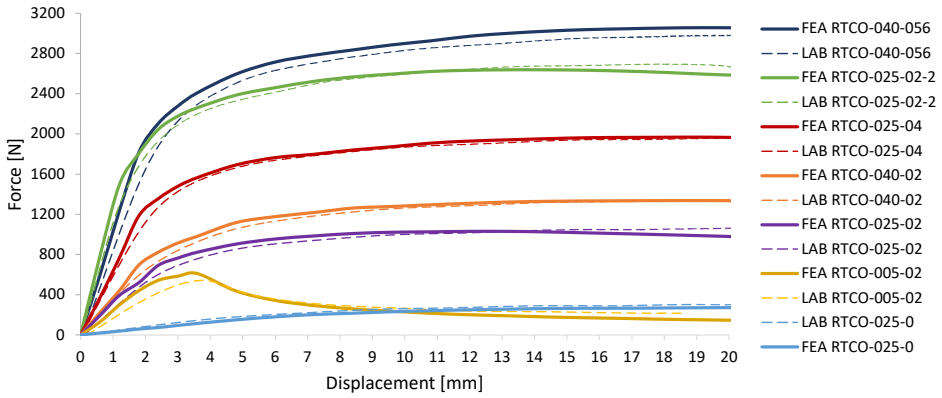

Figure 4.1: Force-displacement curve of the RTCO geometries, experimental data (dashed lines) and FEA data (solid lines).

In Figure 4.1 and Figure 4.2, the results are paired in colours to make it easier to identify and compare the values retrieved from the computational model with respective experimental values. Each specimen test has a defined colour.

The geometries that are more foreseeable in the computational modelling simulation are RTCO, since they have the lowest relative error values, being more concentrated in the 5% error range in Figure 4.3. The FEA and laboratory curves of the same topologies in Figure 4.1 have closer overlapping than in the TO force-displacement curve in Figure 4.2.

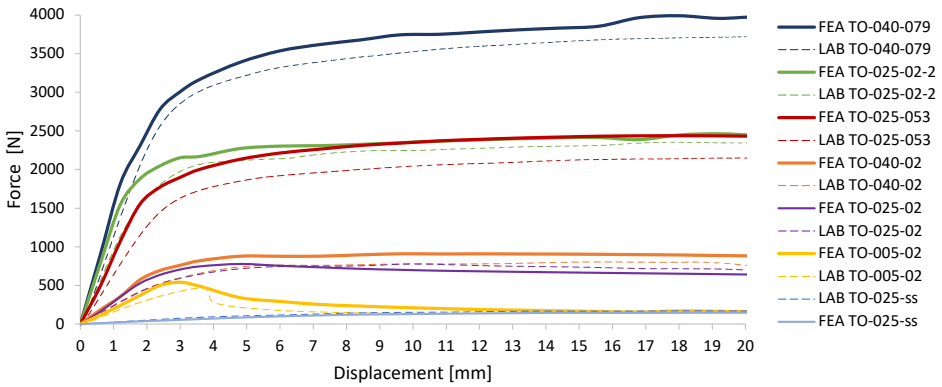

Figure 4.2: Curve force-displacement of the TO geometries, experimental data (dashed lines) and FEA data (solid lines).

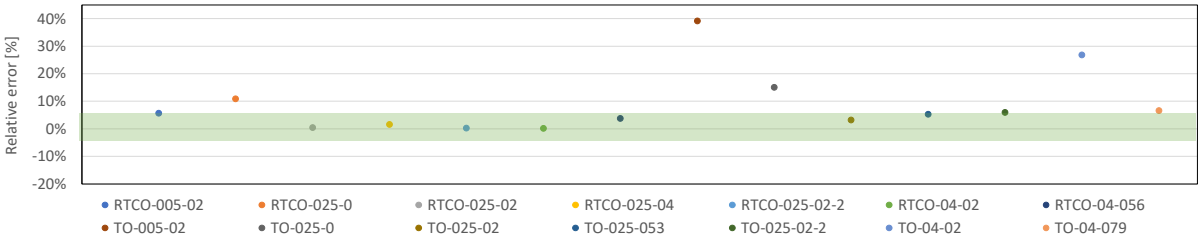

Figure 4.3: Graph with the relative error of the different geometries and relative densities (green area accounts for less than 5% of relative error).

4.2 Comparison between different cell geometries - RTCO and TO

After the computational model validation, the different cell geometries were compared in order to understand the mechanical behaviour of each one. Each figure has force-displacement curves and stiffness of TO and RTCO geometries of Iron and Stainless Steel simulations, with the same relative density and surface height.

The results of the simulations with the lowest relative density geometries and surface height parts (**5% of relative density and 0,2 mm of surface height**) are demonstrated in Figure 4.4. As the lines in Figure 4.4 are close to overlapping, all the samples have the same mechanical behaviour qualitatively.

Table 4.3: Values for Energy absorption (E_a) [J/mm^2] from laboratory tests and FEA of Iron and Stainless Steel of TO and RTCO with density of 5% and surface height of 0,2 mm.

	RTCO		TO	
	Iron	Stainless Steel	Iron	Stainless Steel
FEA	4479	5657	4071	5126
Lab	-	5351	-	2141

After the elastic regime, the force-displacement curve decreases due to buckling on the outer sur-

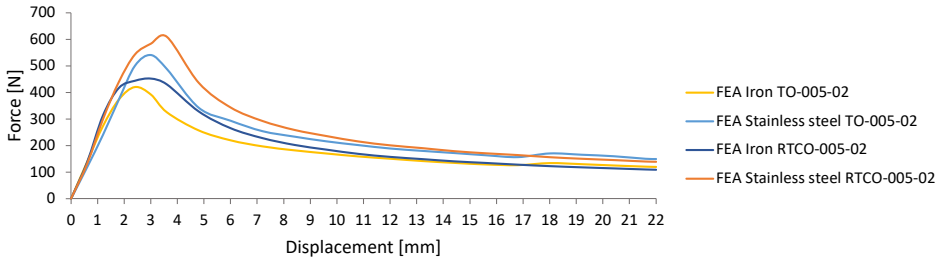

Figure 4.4: Force-displacement curve from FEA of Iron and Stainless Steel of TO and RTCO with density of 5% and surface height of 0,2 mm.

faces and also owing to failures happening in the cells. These outlines were possible to observe in the experimental bending test, where the only geometries demonstrating the failure were the TO and RTCO specimens with the lowest density (5%).

The k, E_a and MRF in the elastic regime values are higher in RTCO than the TO, demonstrated in Table 4.3. In both geometries, the reaction force is higher in Stainless Steel than in Iron (Figure 4.4). However, the geometries' stiffness is similar, as shown in Figure 4.5.

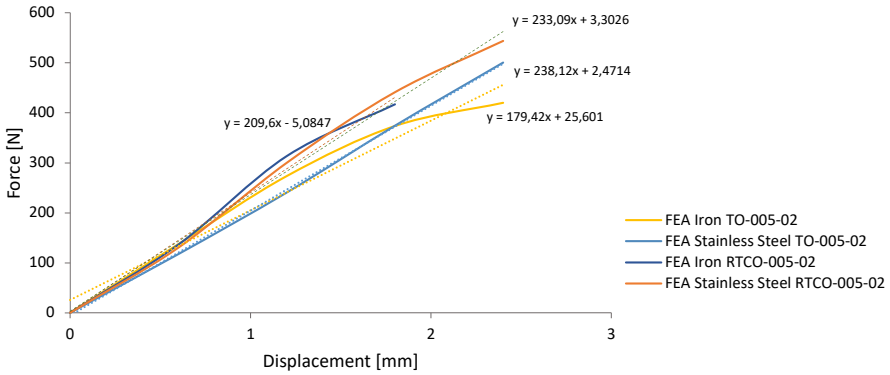

Figure 4.5: Stiffness evaluation from FEA of Iron and Stainless Steel of TO and RTCO with density of 5% and surface height of 0,2 mm.

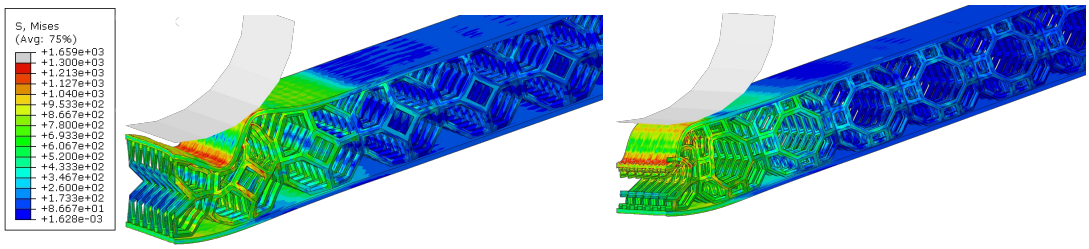

Figure 4.6: FEA of (left) TO and (left) RTCO of 5 % relative density unit cell and 0,2 mm surface height.

The RTCO presents lower stress concentration than TO, however, the deformation of the RTCO centre cell is higher than the TO. This is due to the geometry and the connection between the cells and

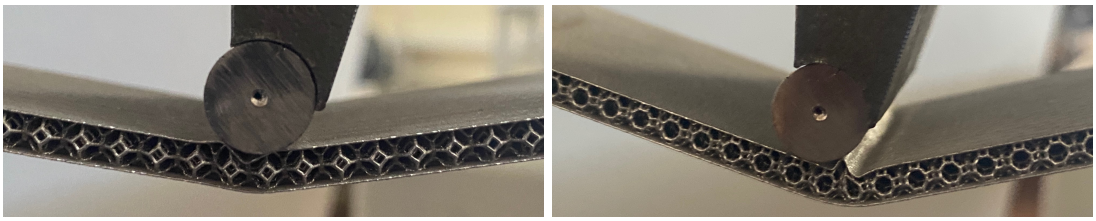

Figure 4.7: Samples produced by SLM (left) TO and (left) RTCO of 5 % relative density unit cell and 0,2 mm surface height.

the outer surfaces. The behaviour of the FEA in both geometries is similar to the experimental samples (Figure 4.6 and Figure 4.7). Buckling is mainly observed in the superior outer surface, as it is the furthest region from the neutral axis that is under compression. The highest compression stress is seen in the surfaces which present wrinkling associated with buckling. The surface is also stiffer than the cells. Consequently, the surface withstands a high portion of the load, possible to observe in Figure 4.6. In RTCO geometry with a relative density of 5% the deformation caused by buckling happens in the centre of the cell located in the middle of the sample, while in TO, the buckling happens between cells (fig. 4.7). In geometries with a relative density of 5%, there is lower load transfer between the outer surfaces and the cells, causing the buckling to be localised, directly onto the surface in contact with the equipment.

There is compressive and tensile stress in the results of the FEA simulations, on the superior outer surfaces, causing the buckling. Meanwhile, there are tensile forces on the lower surface. The 5% relative density was the only sample to present fracture in the cells.

The results from the specimens without surfaces (**25% of relative density without surfaces**) are presented in Figure 4.8. These geometries have cells in direct contact with the bending test equipment.

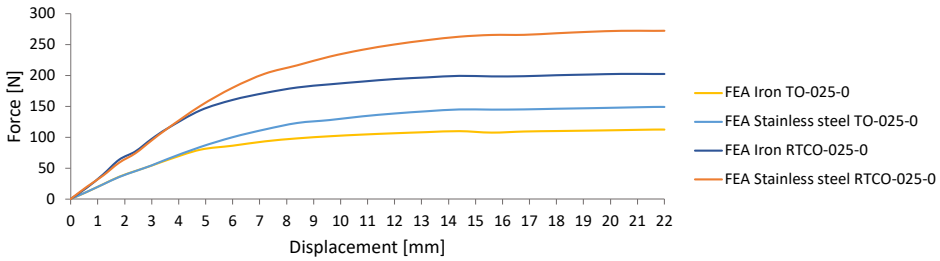

Figure 4.8: Force-displacement curve from FEA of Iron and Stainless Steel of TO and RTCO with density of 25% and no surface.

Table 4.4: Vales for Energy absorption (E_a) [J/mm^2] from laboratory tests and FEA of Iron and Stainless Steel of TO and RTCO with density of 25% and no outer surface.

	RTCO		TO	
	Iron	Stainless Steel	Iron	Stainless Steel
FEA	3633	4546	1991	2513
Lab	-	5101	-	2958

As seen previously, the geometries made of RTCO cells have higher values in the reaction force than those made of TO cells, and those made of Stainless Steel have a higher strength than those made of Iron. In force-displacement curves (Figure 4.8), the geometries with no outer surfaces have the lowest stiffness, reaction force and energy absorption values (Table 4.4).

Despite the presence of an elastic regime, the slope is lower in the force-displacement curve, having lower stiffness when compared to all models with surfaces.

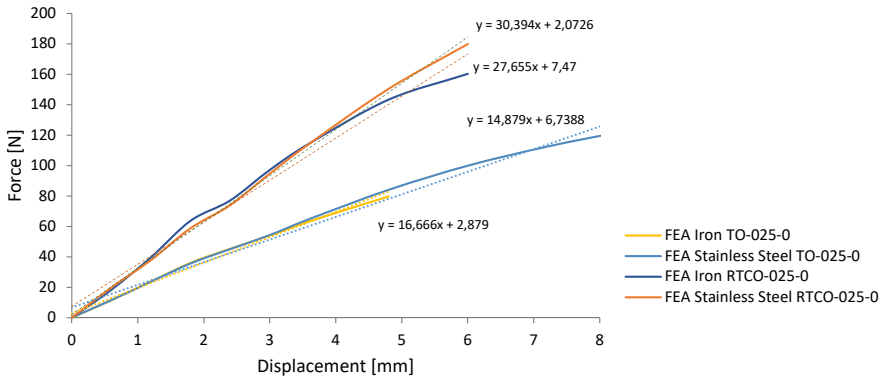

Figure 4.9: Stiffness evaluation from FEA of Iron and Stainless Steel of TO and RTCO with density of 25% and no surface.

The mechanical behaviour qualitatively is similar in FEA and in the experimental tests (Figures 4.10 and 4.11). There is no buckling due to the absence of the outer surface. The stresses are located between the cells, because there is the transmission of stresses by the cells, unlike models with outer surfaces.

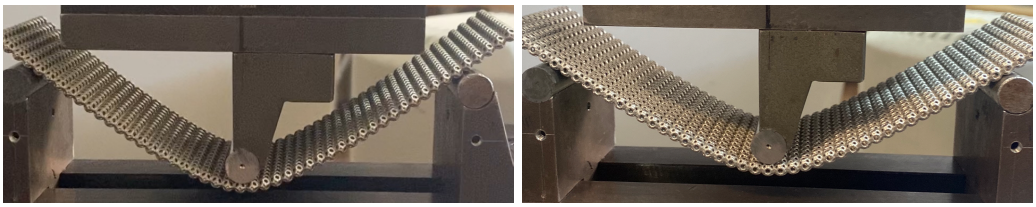

Figure 4.10: Samples produced by SLM (left) TO and (left) RTCO of 25 % relative density unit cell and no surface.

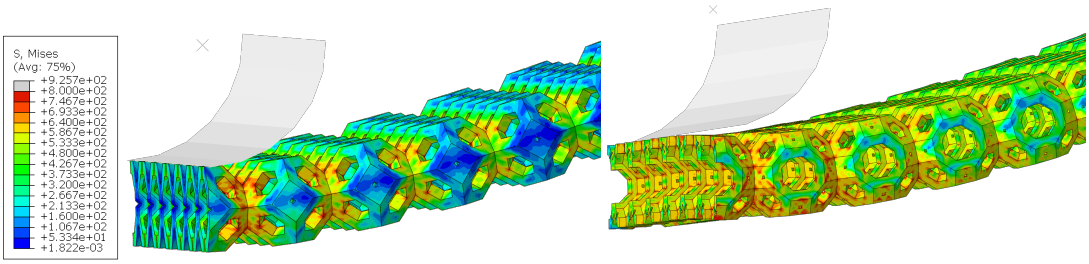

Figure 4.11: FEA of (left) TO and (left) RTCO of 25% relative density unit cell and no surface.

After the deformation, when the samples are no longer under load application, the structures without surfaces have a greater recovery, compared to all models with surfaces. The stiffness is higher in the RTCO geometry than in the TO geometry (Figure 4.9). However, the values are similar between the different materials, indicating that the elastic regime is similar with both Stainless Steel and Iron materials. These can be expected because the two materials have similar E, due to the resemblance of chemical bonds between the main element in both materials, iron.

In Figure 4.12, the force-displacement curve of the computational model of RTCO and TO geometries with **25% of relative density and 0,2 mm of surface height** is presented.

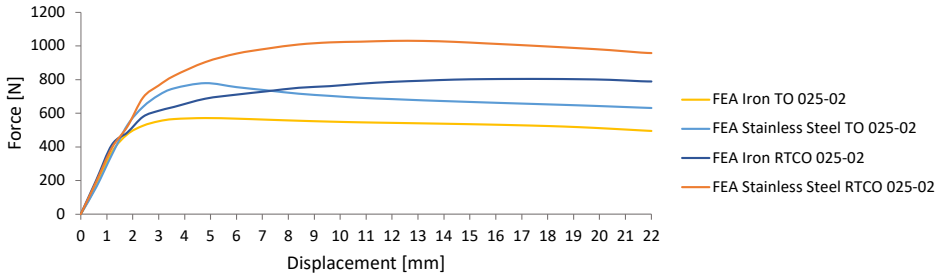

Figure 4.12: Force-displacement curve from FEA of Iron and Stainless Steel of TO and RTCO with density of 25% and surface height of 0,2 mm.

Force values of RTCO geometries are higher than TO compared with the same material, and the Stainless Steel material has higher energy absorption and stiffness than the Iron material (Figure 4.12). Nevertheless, contrary to the geometries presented before, the Stainless Steel TO computational model has higher reaction force values in the elastic regime than the Iron RTCO model (Table 4.5), meaning that the Stainless Steel TO model is stiffer than the Iron RTCO model, since the latter has a lower slope in the elastic regime.

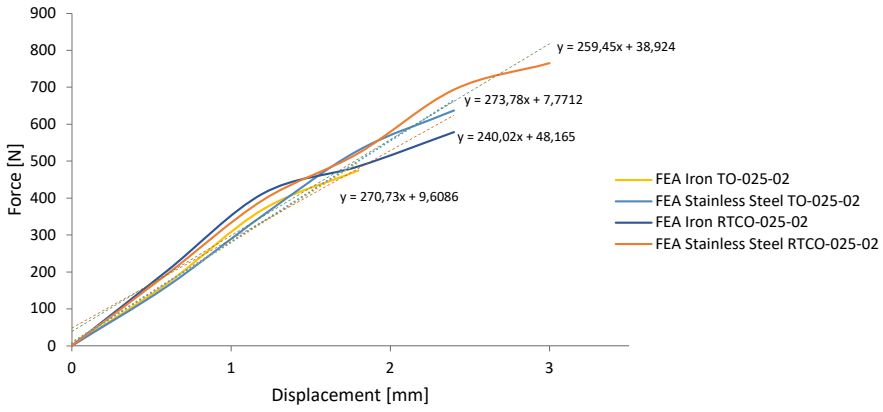

Figure 4.13: Stiffness evaluation from FEA of Iron and Stainless Steel of TO and RTCO with density of 25% and surface height of 0,2 mm.

Table 4.5: Vales for Energy absorption (E_a) [J/mm^2] from laboratory tests and FEA of Iron and Stainless Steel of TO and RTCO with density of 25% and surface height of 0,2 mm.

	RTCO		TO	
	Iron	Stainless Steel	Iron	Stainless Steel
FEA	15703	20004	11350	14334
Lab	-	19913	-	14809

The stiffness values in Figure 4.13 are similar between cell geometries. The Iron TO model starts deforming permanently (entering in the elastic-plastic regime) at a lower displacement value than the other geometries. The Stainless Steel RTCO model is the latest transitioning to the plastic regime, at a higher displacement value, compared with the other model in Figure 4.13.

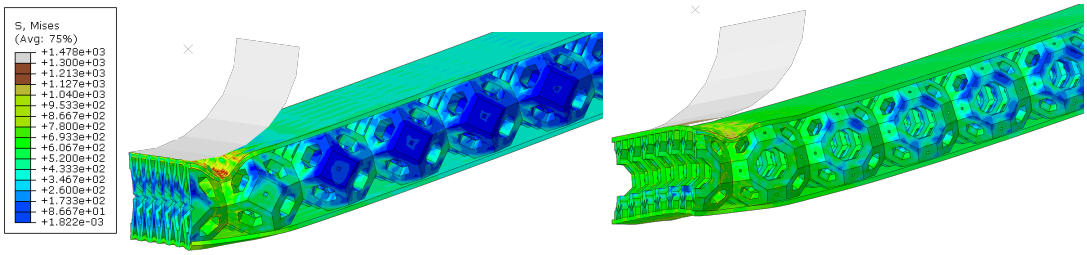

Figure 4.14: FEA of (left) TO and (left) RTCO of 20% relative density unit cell 0,2 mm of surface height.

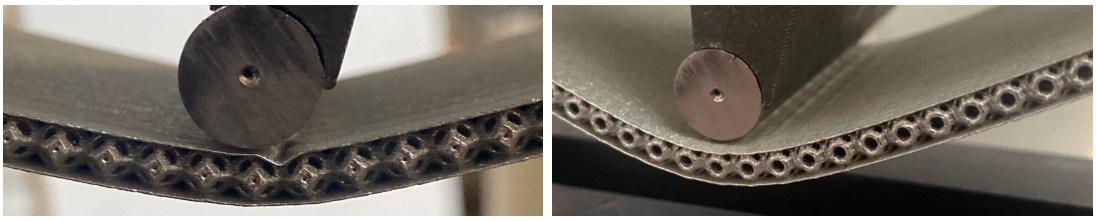

Figure 4.15: Samples produced by SLM (left) TO and (left) RTCO of 25% relative density unit cell and 0,2 mm surface height.

Comparing these models with the TO and RTCO with 25% of relative density and no surface, the force difference between the samples with and without outer surfaces is a direct consequence of the impactful contribution of the surface to the geometry's stiffness. The stiffness will have impact on the moment of inertia in the samples (eq. (4.2)).

$$k = \frac{3EI}{a^3} \tag{4.2}$$

The higher the applied force, the higher the bending moment (eq. (4.3)). As a consequence, there is an increase in deflection (eq. (4.4)), where δ is deflection, P is the load applied in the beam, a is the measured distance end-to-end beam, E is Young's modulus and I is the moment of inertia [105]. The moment of inertia equation (eq. (4.5)) sustains this statement.

$$\sigma = \frac{PS_{/2}c}{I} = \frac{Mc}{I} \tag{4.3}$$

$$\delta = \frac{Pa^3}{48EI} \tag{4.4}$$

$$I = 2(\frac{1}{12}h^3b) + I_{(y)} \tag{4.5}$$

The bending behaviour depends on the moment of inertia, I (Equation (4.3)). The higher the I, the maximum stress (σ_{max}) will decrease. To increase σ the M (applied load (P) x distance of the supports and the loading bar ($S_{/2}$)) needs to increase.

I, the moment of inertia is directly related to the cross-section geometry where the load is applied, (h, and a, are the surface height and length, respectively). In cellular materials due to the difference in the cross-section geometries in the core, $I_{(y)}$ is the calculation of the moment of inertia that is dependent on the y-axis.

For example in Figure 4.16 and Figure 4.17 is possible to observe two different cross-sections of the same sample. The difference in geometry and the distance of the distribution of the cross-section area from the neutral axis (orange zone represented in Figure 4.16 and Figure 4.17) has a significant impact on the bending moment. When a load is applied in a cross-section where the majority of the area is near the neutral axis, the stresses will be higher and the moment of inertia is going to be lower. When a load is applied in a cross-section where the area is distributed in the extremities of the sample and far from the neutral axis, the stresses will be lower and the moment of inertia is going to be higher, possible to observe in eq. (4.6).

$$I = \frac{Md_n}{\sigma_b} \tag{4.6}$$

In eq. (4.6) the moment of inertia of a beam about its neutral axis is calculated. The M is the bending moment, the d_n is the distance from the neutral axis to the point where the bending stress is being calculated and σ_b is the bending stress applied.

In Figure 4.16 and Figure 4.17 on the right is possible to observe geometry area is concentrated in the centre, being more prone to buckling. On the left the concentration of the mass is in the extremities of the samples, having a higher moment of inertia.

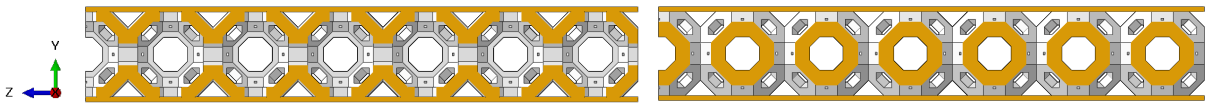

Figure 4.16: RTCO cross-section area in two different zones (orange zone).

The stiffness (k) increases (Equation (4.2)), when the relative density, the volume and the cross-

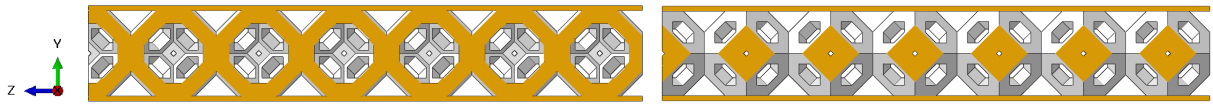

Figure 4.17: TO cross-section area in two different zones (orange zone).

section area of the samples increase (explained in Equation (3.1) and in Section 3.1.1). To maintain the σ, when the geometry is stiffer, the M will increase. The geometry dimensions have an impact on the maximum stress (σ_{max}) in the samples (Equations (4.3) and (4.5)).

The concentration of area in the cross-section where the load is applied is also important, the higher the concentration the stiffer the sample will be, and is less prone to buckle.

In Figure 4.14 and Figure 4.15, the stress presented in the TO and RTCO are similar, both located in the outer surface in the gap between cells, where is possible to observe buckling. Qualitatively the mechanical behaviour is similar both in FEA and the experimental bending test.

The data from the computational model of RTCO and TO with a **relative density of 25% and surface height of 0,4 and 0,53 mm**, respectively, is presented in Figure 4.18.

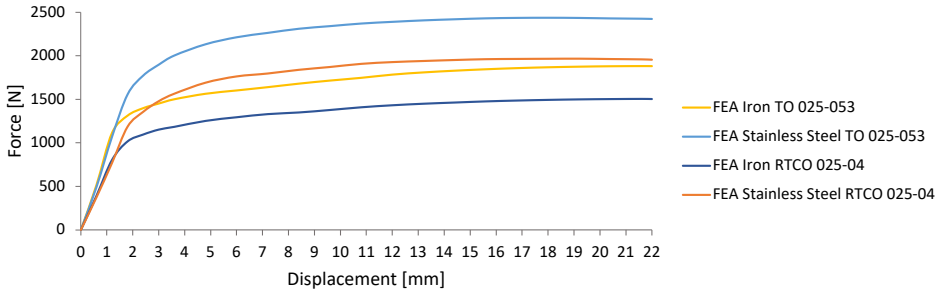

Figure 4.18: Force-displacement curve from FEA of Iron and Stainless Steel of TO and RTCO with density of 25% and surface height of 0,53 and 0,4 mm respectively.

The surface thicknesses of the cell geometries are different from each other, in order to determine the influence of the facing thickness in the specimens. In these models, the surface thickness considered had into account the geometry edges of the specific relative density 25%, for example in TO of relative density 0.25 the edge thickness is 0.53 mm. Therefore, the face thickness is 0.53 mm. All the calculations used to determine the surface thickness are presented in the chapter 3 in section 3.1.

Table 4.6: Vales for Energy absorption (E_a) [J/mm^2] from laboratory tests and FEA of Iron and Stainless Steel of TO and RTCO with density of 25% and surface height of 0,53 and 0,4 mm respectively.

	RTCO		TO	
	Iron	Stainless Steel	Iron	Stainless Steel
FEA	29032	38294	35339	47930
Lab	-	37696	-	45513

Contrary to the force-displacement curves presented before, the reaction force and absorption en-

ergy of the TO model have higher values than the RTCO model in Figure 4.18. This is due to the difference in the surface heights applied to the geometries. The TO sample has a higher surface height than RTCO. When there is higher volume and relative density, the stiffness and reaction force will increase, because the geometry has an impact on the maximum stress (σ_{max}) in the samples (Equation (4.3) and Equation (4.5) - effect of inertia).

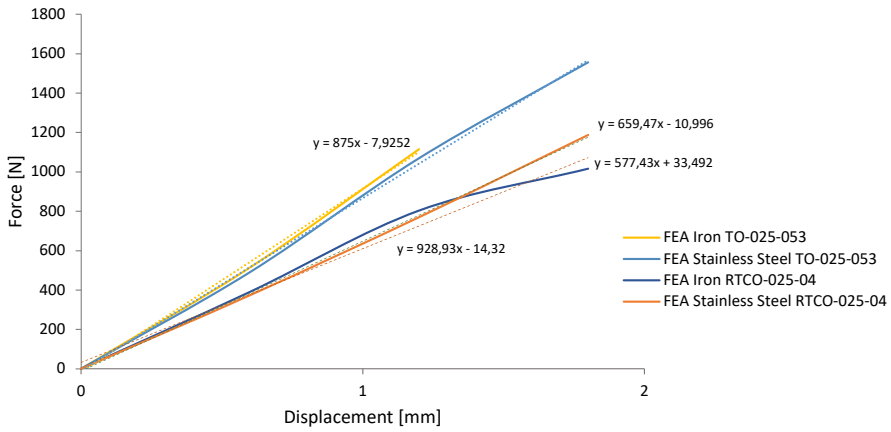

Figure 4.19: Stiffness evaluation from FEA of Iron and Stainless Steel of TO and RTCO with density of 25% and surface height of 0,53 and 0,4 mm respectively.

It can be concluded that the height of the surfaces that delimit the cells has a great impact on the reaction force of each test piece to the detriment of the geometry of the cells.

The Stainless Steel models have higher energy absorption values than the Iron models, presented in Figure 4.18 and in Table 4.6.

The stiffness is similar within the same cell geometry. The TO has higher stiffness than the RTCO. The elastic region behaviour is expected to be similar since the slopes presented in Figure 4.19 are similar. However, the Stainless Steel models need more force to enter the plastic regime than the Iron models.

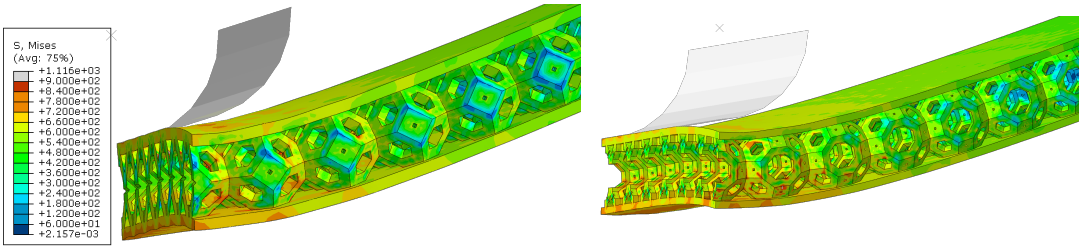

Figure 4.20: FEA of (left) TO and (left) RTCO of 25% relative density unit cell and 0,53 and 0,4 mm of surface height, respectively.

As the height of the outer surface is higher, the outer surface separates from the loading bar (in Figure 4.20). It is to be noted that the model is ¼ of the samples. Thus, the centre is supporting more

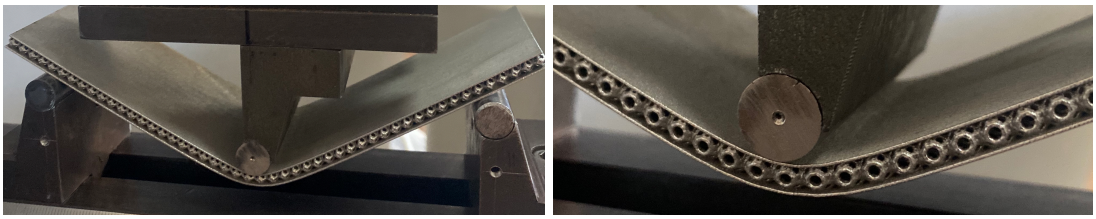

Figure 4.21: Samples produced by SLM (left) TO and (left) RTCO of 25% relative density unit cell and 0,53 and 0,4 mm of surface height.

load than the outer part of the sample since it is not in contact. The behaviour of the cells qualitatively is similar between the FEA and laboratory tests (in Figure 4.20 and Figure 4.21).

The next models to be analysed are TO and RTCO with a **relative density of 25%, a surface height of 0,2 mm and 2 cell rows**. These models were simulated in order to understand the difference between one and two rows of cells and to understand the influence of the number of cells on the mechanical behaviour of the structures.

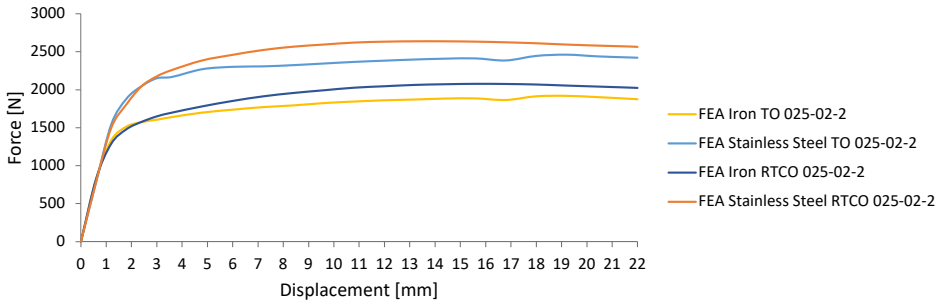

Figure 4.22: Force-displacement curve from FEA of Iron and Stainless Steel of TO and RTCO with density of 25%, surface height of 0,2 mm and 2 cell layers.

The Stainless Steel RTCO model presents greater force-displacement values than the Stainless Steel TO model. This also happens with the Iron material models. The latter has lower values than the Stainless Steel material models.

Table 4.7: Vales for Energy absorption (E_a) [J/mm^2] from laboratory tests and FEA of Iron and Stainless Steel of TO and RTCO with density of 25% and surface height of 0,2 mm and 2 cell layers.

	RTCO		TO	
	Iron	Stainless Steel	Iron	Stainless Steel
FEA	41240	52924	38367	49350
Lab	-	52782	-	46569

Comparing the values obtained from the same relative density (25%) and same height surface (0,2 mm) but only one row, there is an increase of the absorpted energy and the reaction force values of about 2.5 times more with the second layer in both geometries, shown in Table 4.5 and Table 4.7.

Despite, comparing the three models, with the same relative density (25%), the best ratio between

volume/reaction force is with an increase in surface height, that is, the surface height has a greater impact on the mechanical behaviour of the specimens than an increase in the number of layers.

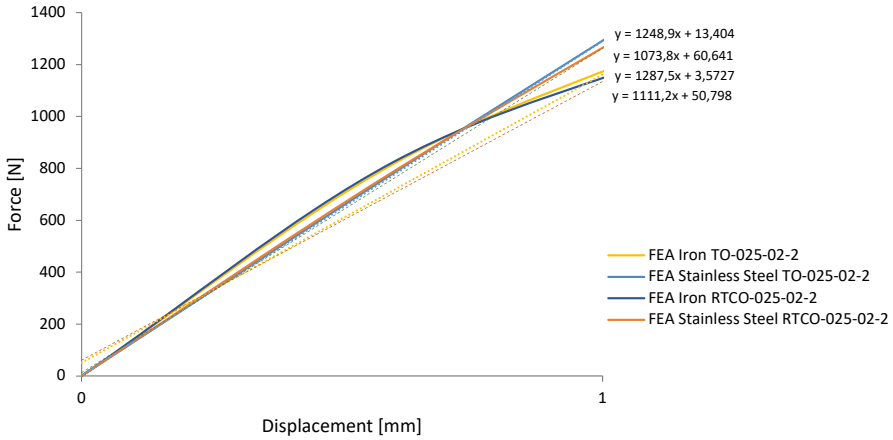

Figure 4.23: Stiffness evaluation from FEA of Iron and Stainless Steel of TO and RTCO with density of 25%, surface height of 0,2 mm and 2 cell layers.

The RTCO have higher stiffness than the TO (Figure 4.23). The stiffness values are similar between Iron and Stainless Steel materials in the same type of geometry. With the increase in the number of rows, the cells' stiffness increases. All of the computational models presented in the Figure 4.23 enter the plastic regime with the same displacement, independently of the geometry or material applied.

The samples with two rows of cells experience more evident signs of buckling in the outer surfaces compared with the rest of the samples. This is due to the increase of the influence of the cells in the sample. In the two-row samples, due to the increase in the distance of the neutral axis, the surface stresses also increase.

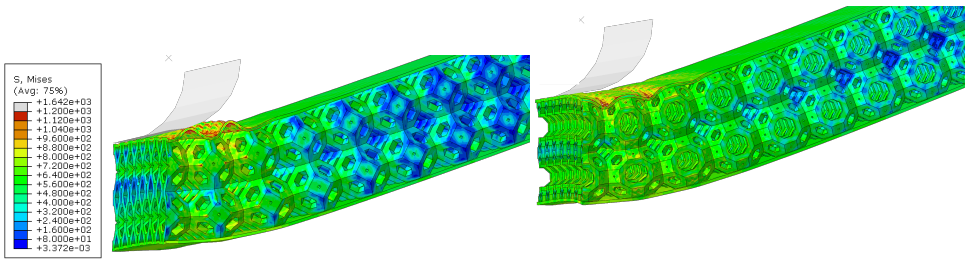

Figure 4.24: FEA of (left) TO and (left) RTCO of 25% relative density unit cell, 0,2 mm of surface height and two rows of cells.

Qualitatively the mechanical behaviour of the FEA is similar to the laboratory tests (Figures 4.24 and 4.25). The computational models presented in Figure 4.26 have the highest relative density in the samples scopes, which accounts for **40% and have 0,2 mm of surface height**. The computational model containing the RTCO cell geometries has higher energy absorption and force values than the TO

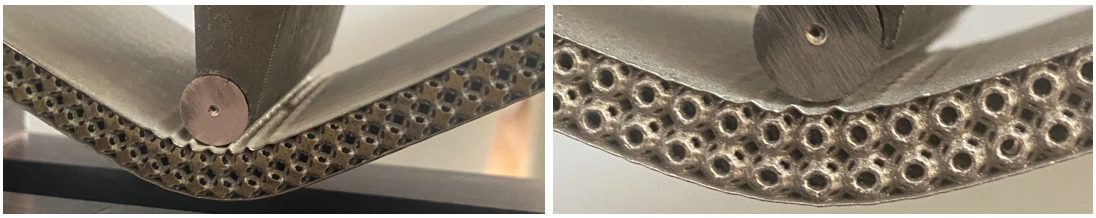

Figure 4.25: Samples produced by SLM (left) TO and (left) RTCO of 25% relative density unit cell and 0,2 mm of surface height and two rows of cells.

(Table 4.8).

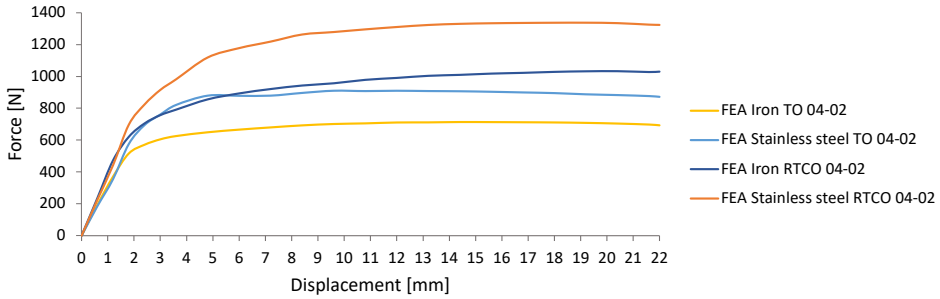

Figure 4.26: Force-displacement curve from FEA of Iron and Stainless Steel of TO and RTCO with density of 40% and surface height of 0,2 mm.

There is a significant difference between the models with Stainless Steel material properties and the Iron material properties, having the latter having lower values.

Table 4.8: Vales for Energy absorption (E_a) [J/mm^2] from laboratory tests and FEA of Iron and Stainless Steel of TO and RTCO with density 40% and surface height of 0,2 mm.

	RTCO		TO	
	Iron	Stainless Steel	Iron	Stainless Steel
FEA	19848	25650	14331	18197
Lab	-	25608	-	28686

The stiffness values between the same geometries are similar (Figure 4.27). The Iron material models enters the plastic regime with lower displacement than the Stainless Steel models, which means the samples with Iron material start having permanent deformation with less displacement applied than the Stainless Steel samples.

The TO sample has a higher stress concentration. The space between the cells allows the surface to move into it, contrary to the RTCO case (Figure 4.28 and Figure 4.29). In TO, because of the buckling in the surface, the relative stiffness can be higher in the cells than in the outer surface. The stress distribution in the centre is more even in the RTCO sample (fig. 4.28). In this sample, the stress distribution is similar in the outer surfaces and the cells. The FEA mechanical behaviour is similar to the laboratory test, qualitatively (Figures 4.28 and 4.29).

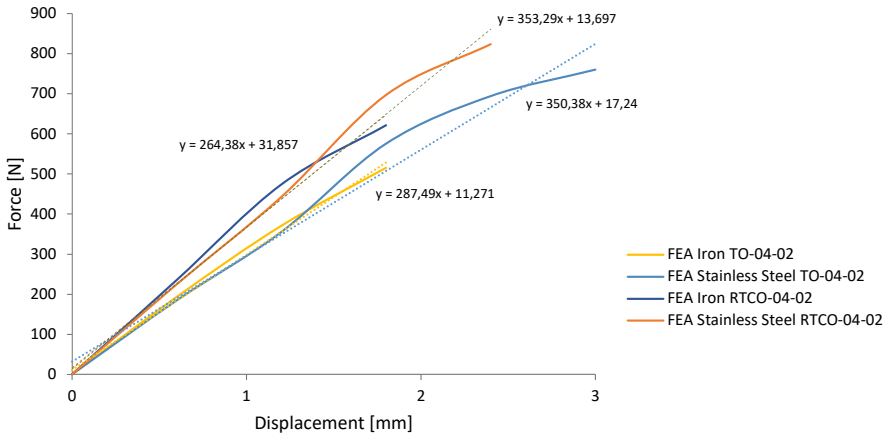

Figure 4.27: Stiffness evaluation from FEA of Iron and Stainless Steel of TO and RTCO with density of 40% and surface height of 0,2 mm.

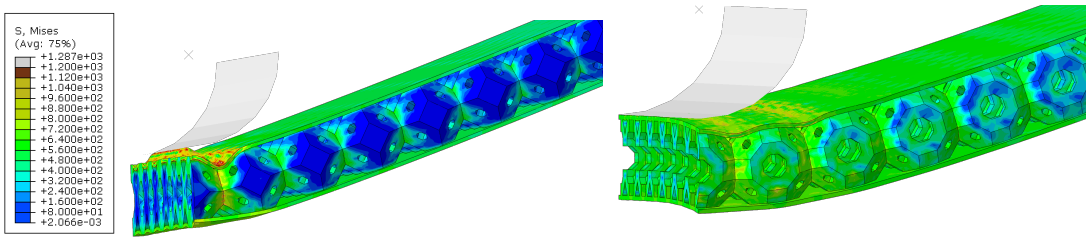

Figure 4.28: FEA of (left) TO and (right) RTCO of 40% relative density unit cell and 0,2 mm of surface height.

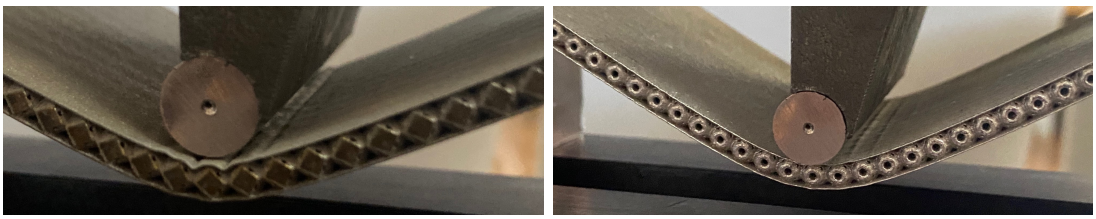

Figure 4.29: Samples produced by SLM (left) TO and (left) RTCO of 40% relative density unit cell and 0,2 mm of surface height.

Last but not least, as presented in Figure 4.30, the RTCO and TO models of Stainless Steel and Iron with a **relative density of 40% and surface height of 0,56 and 0,79 mm** respectively, are analysed.

Table 4.9: Vales for Energy absorption (E_a) [J/mm^2] from laboratory tests and FEA of Iron and Stainless Steel of TO and RTCO with density 40% and surface height 0,79 and 0,56 mm, respectively.

	RTCO		TO	
	Iron	Stainless Steel	Iron	Stainless Steel
FEA	44886	59224	57892	76712
Lab	-	57083	-	71939

As it happens with the computational model of RTCO and TO with a relative density of 25% and surface height of 0,56 and 0,79 mm, respectively. The surface thicknesses of the cell geometries are

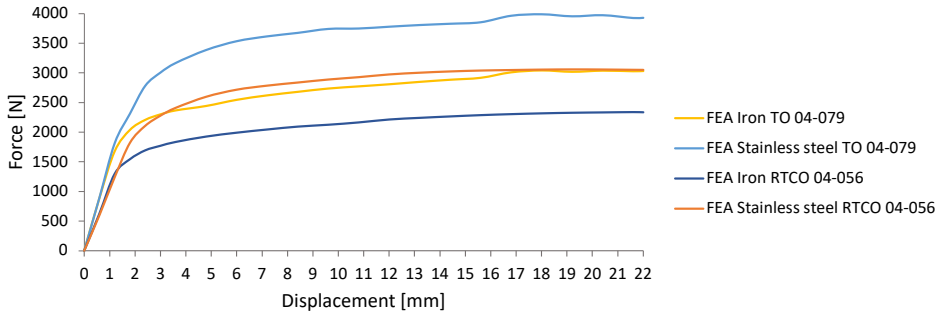

Figure 4.30: Force-displacement curve from FEA of Iron and Stainless Steel of TO and RTCO with density of 25% and surface height of 0,79 and 0,56 mm respectively.

different from each other, due to the geometry edges of the specific relative density 40% being different in TO and RTCO. All the calculations used to determine the surface thickness are presented in Chapter 3.

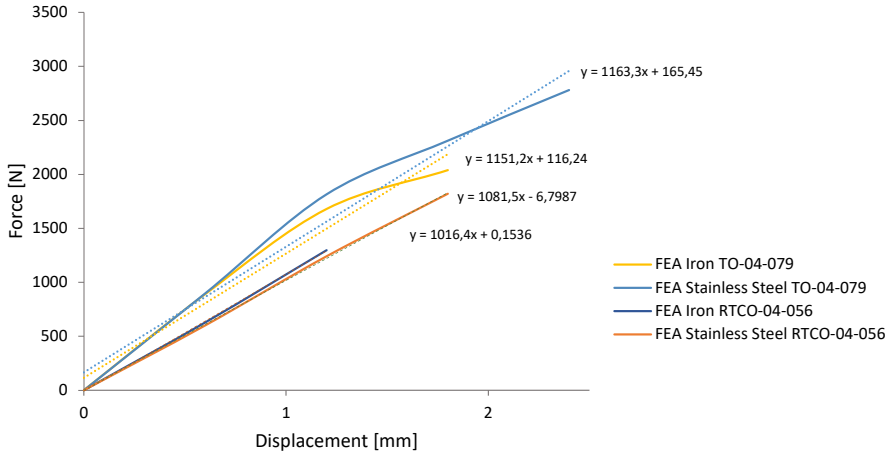

Figure 4.31: Stiffness evaluation from FEA of Iron and Stainless Steel of TO and RTCO with a relative density of 40% and surface height of 0,79 and 0,56 mm, respectively.

The RTCO model has lower energy absorption and force-displacement values than TO due to the latter having thicker surfaces. In the model presented in Figure 4.31, the surfaces that delimit the cells have a substantial influence on the mechanical behaviour of the specimens.

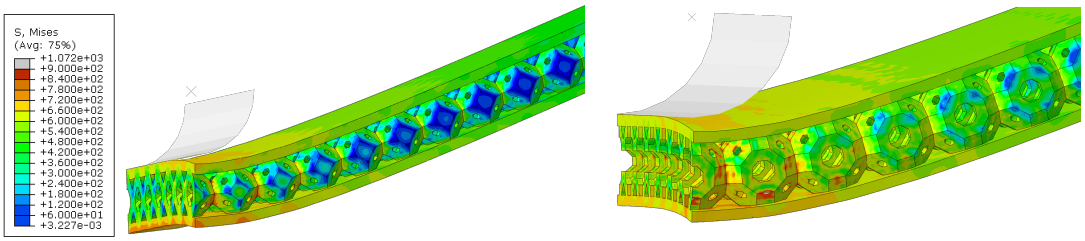

Figure 4.32: FEA of (left) TO and (left) RTCO of 40% relative density unit cell and 0,79 and 0,56 mm respectively of surface height.

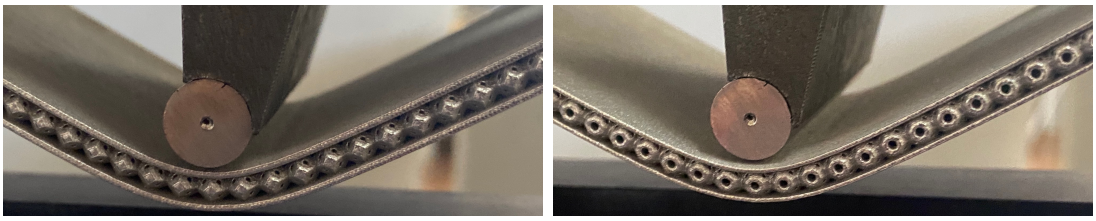

Figure 4.33: Samples produced by SLM (left) TO and (left) RTCO of 40% relative density unit cell and 0,79 and 0,56 mm respectively of surface height.

The Stainless Steel model has higher force values, while the stiffness is higher in TO geometry models than the RTCO and the latter enters in the plastic regime with lower applied displacement.

Both samples do not experience buckling, and similarly to the samples with 25% of relative density and heights of 0,53 and 0,4 mm (TO and RTCO, respectively), the outer surface in the exterior edges, detaches from the loading bar. These are the samples with higher values of reaction force and stiffness and have less stress concentration because of the higher height in the outer surfaces.

The stress levels in these models are higher since the relative density of the cell is higher. The load is more evenly distributed. There is less concentration of stresses in the models because of the transference of stresses. Qualitatively the mechanical behaviour is similar between the FEA and laboratory test (Figures 4.32 and 4.33).

4.3 Comparison between different densities and surface heights

To understand the impact of the different relative densities and wall heights, a performance index analysis was carried out. The performance index was used to evaluate the bending properties of the specimens studied. The performance index method is a common tool to assist in decision-making, being useful to facilitate the rationalization of design and application in engineering.

The selection of the features studied in this thesis had to do with overall mechanical performance. To understand the results, there are two main factors to take into consideration, the material properties and geometry. To analyse these, the stiffness, maximum reaction force (both present in Table D.3) and relative density of the whole structure including the surfaces (Table 4.10 and Table 4.11) were taken into account.

The values analysed by this method are the laboratory and FEA results of RTCO and TO geometries made of Stainless Steel. The relative density densities ($\bar{\rho}$) were calculated for the laboratory result according to Equation (4.7):

$$\bar{\rho} = \frac{V_M}{V_T} = \frac{\rho*}{\rho_s} \tag{4.7}$$

The volume of the material is represented V_M and the total volume of the specimen is V_T. $\rho*$ is the cellular material density and the ρ_s is the solid material density.

For the laboratory results, measures were performed before the bending test and are presented in Section 3.4.2. For the measurement of the computational model, the relative densities were retrieved from the software SolidWorks. The properties of the materials were introduced into the software in order to obtain a calculated relative density from the modelled topology of the samples.

Table 4.10: Relative density values for the RTCO samples [%].

Core Relative Density [%]	5	25				40	
Outer surfaces height [mm]	0,2	0	0,2	0,4	0,2-2	0,2	0,56
Total Relative Density [%]	15	25	33	39	29	46	54

Table 4.11: Relative density values for the TO samples [%].

Core Relative Density [%]	5	25				40	
Outer surfaces height [mm]	0,2	0	0,2	0,53	0,2-2	0,2	0,79
Total Relative Density [%]	15	25	33	42	29	46	58

The performance index used is described in Equation (4.8).

$$PI = \frac{\bar{\rho} \cdot k}{MRF} \tag{4.8}$$

PI is the performance index, k is the stiffness, MRF is the maximum reaction force in the elastic regime. The values of PI for the specimens are in the Appendix D in Table D.3. The performance index calculations are presented in appendix E in more detail. The eq. (4.8) should be minimized, meaning that to obtain the best PI, the calculations should have the lowest values possible.

Equation (4.8) is obtained from the analysis by Ashby for the minimization of mass in the case of bending of a plate [105].

In the present analysis, the higher the MRF and the lower the relative density, the greater the performance of the part. To avoid stress shielding, despite the maximisation of the MRF, these structures should have lower k values. Through the Equation (4.8), there is the optimization of mechanical properties intrinsic to the material, but also of the geometry. The lower the stiffness and relative density and the higher the maximum reaction force in the elastic regime the better behaviour the geometry is going to have.

The performance index from the experimental bending test with the RTCO samples is analysed in Figure 4.34. The index presents a slope of 1, calculated by Equation (4.8).

The best experimental bending test specimens with the RTCO geometries are mentioned below:

- RTCO with a relative density of 5% and surface height of 0,2 mm,
- RTCO with a relative density of 25% without surfaces,

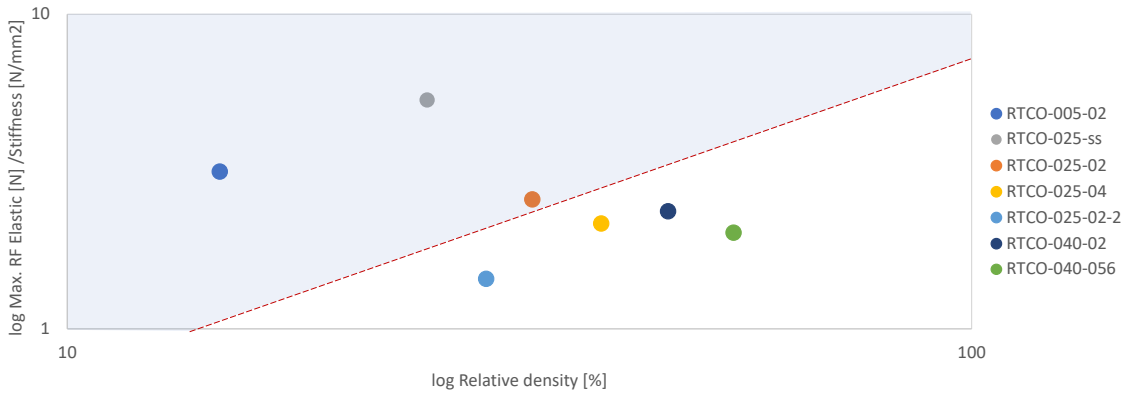

Figure 4.34: Performance index of experimental flexural test with the RTCO samples.

- RTCO with a relative density of 25% and surface height of 0,2 mm.

However it is important to note that the two-cell row specimen has an increase of 164% on the energy absorption (E_a), and the importance of the cells in the specimens is greater when the number of rows increases.

Nevertheless, for specimens with only one row of cells, the surface height has more influence. Changing the height of the surfaces can lead to higher E_a without compromising the mass-to-volume ratio, when comparing the sample with two-cell rows, and the sample with one row of cells and the height corresponding to the measure of the edge of the cell. To achieve approximately the same energy absorption (E_a) of the sample with two-cell rows, but only using one row of cells, the height surfaces only need to increase to 0,8 mm. For instance, if RTCO samples with a relative density of 25% with one row of cells, to get the same E_a as the two-row cells sample, the height surface needs to be 0,8 mm instead of having 0,4 mm.

The performance indexes from the FEA of Stainless Steel with the RTCO specimens are analysed in the Figure 4.35. The index presents a slope calculated by the Equation (4.8).

The results are similar to the performance indexes of the experimental bending test with the RTCO specimens. The best specimens in the FEA of the Stainless Steel with the RTCO geometries are mentioned below:

- RTCO with a relative density of 25% without surfaces,
- RTCO with a relative density of 5% and surface height of 0,2 mm,
- RTCO with a relative density of 25% and surface height of 0,2 mm.

The conclusions are the same as the performance index of the experimental bending test, mentioned before. It was found that there is an increase in E_a of 88% from the RTCO with a relative density of 25% without a surface specimen to RTCO with 0,2 mm surface height and same relative density. The RTCO

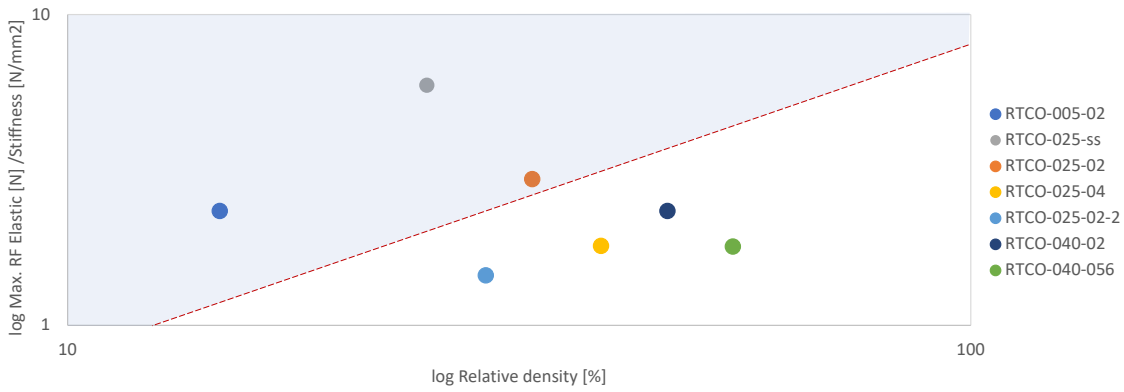

Figure 4.35: Performance index of FEA of the Stainless Steel with the RTCO parts.

with a relative density of 25% and surface height of 0,4 mm has an increase in E_a of 61% of performance compared to RTCO with 0,2 mm surface height and same relative density. In the specimens with a relative density of 40%, when the initial surface height of 0,2 mm increases to 0,4 mm, the performance increases 65%. In Table 4.12, presents the increase of E_a.

Table 4.12: Performance index - Influence of surface height for E_a - RTCO geometries.

Performance index - Influence of surface height - RTCO				
RTCO-025-0	RTCO-025-02	RTCO-025-04	RTCO-04-02	RTCO-04-056
88%		-	-	-
-	61%		-	-
-	-	-	65%	

The performance index of the experimental flexural test of TO geometries analysed is presented in Figure 4.36.

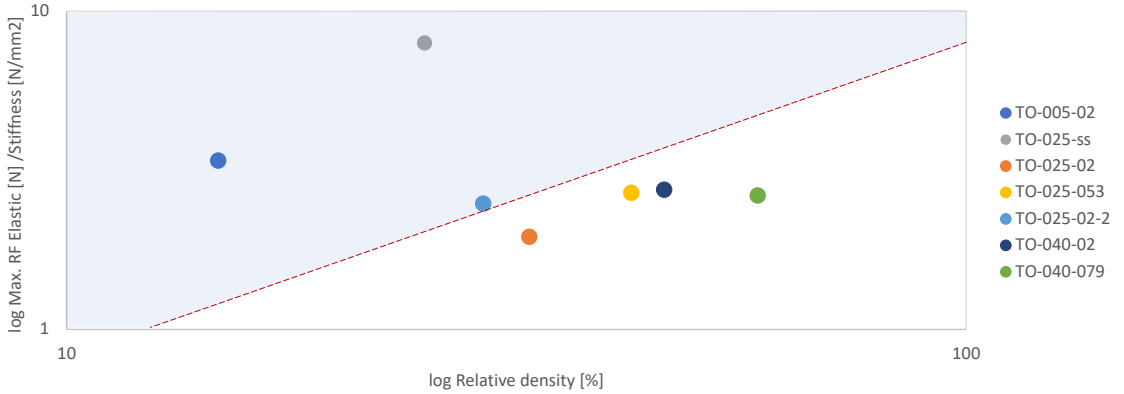

Figure 4.36: Performance index of experimental flexural test with the TO samples.

The best specimens in the experimental bending test with the TO geometries are mentioned below:

- TO with a relative density of 25% without surface,

- TO with a relative density of 5% and surface height of 0,2 mm,
- TO with a relative density of 25% and surface height of 0,2 mm and two rows of cells.

The same conclusion was retrieved from the previous index analysis, the influence of the surfaces is greater than the cells, however when increasing the number of rows, the cells influence more the mechanical behaviour of the specimen.

The performance index of the FEA of TO geometries analysed is presented in Figure 4.37.

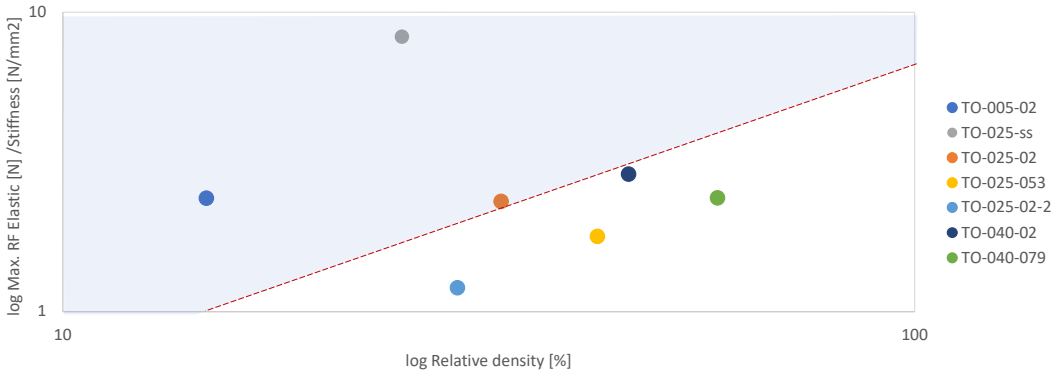

Figure 4.37: Performance index of FEA of the Stainless Steel with the TO parts.

The data retrieved from the FEA TO performance index has the highest performers are:

- TO with a relative density of 25% without surfaces,
- TO with a relative density of 5% and surface height of 0,2 mm,
- TO with a relative density of 25% and surface height of 0,2 mm.

The FEA values are slightly higher than the flexural test values. The explanation for this is detailed in Section 4.1.

In Section 4.2, the cells with the best behaviour are the RTCO. In the analysis of the influence of the surface height of the TO geometry, the E_a percentage increases between geometries are much higher than RTCO, meaning that the surface height has a higher effect on the TO geometry specimens. The TO with a relative density of 25% and with a surface height of 0,2 mm has an increase of 95% in E_a to RTCO with a relative density of 25% without surfaces.

The TO with a relative density of 25% and with a surface height of 0,4 mm has an increase in E_a of 69% compared to RTCO with a relative density of 25% and with a surface height of 0,2 mm.

The specimens with higher relative density, 40%, have an increase of 77% in E_a when the surface height increases from 0,2 mm to 0,79 mm, the analysis of the increase of E_a is mentioned in Table 4.13.

The values obtained from the performance index are presented in table 4.14 and table 4.15, for RTCO and TO geometries, both using the experimental and FEA results. These calculations used the

Table 4.13: Performance index - Influence of surface height for E_a - RTCO geometries.

Performance index - Influence of surface height - TO				
TO-025-0	TO-025-02	TO-025-053	TO-04-02	TO-04-079
95%		-	-	-
-	69%		-	-
-	-	-	77%	

eq. (4.8). When comparing the PI between the stainless steel and iron, both have similar values, and this is due to the variables selected referring to samples in the elastic regime only. The stainless steel and iron have similar E and k, thus they will show similar behaviour in the elastic regime.

Table 4.14: Performance index values (eq. (4.8)) - RTCO geometries.

	RTCO						
Relative Density [%]	5	25				40	
Surface height [mm]	0,2	0	0,2	0,4	0,2-2	0,2	0,56
Lab PI	4,67	4,68	12,70	18,02	20,19	19,52	27,02
FEA PI	6,32	4,22	11,09	21,64	20,07	19,8	30,47

Table 4.15: Performance index values (eq. (4.8)) - TO geometries.

	TO						
Relative Density [%]	5	25				40	
Surface height [mm]	0,2	0	0,2	0,53	0,2-2	0,2	0,79
Lab PI	4,35	3,14	16,72	15,79	11,7	16,79	22,28
FEA PI	6,18	3,02	14,04	23,85	24,21	99,22	43,83

This analysis only evaluates the mechanical properties, not the best geometries for bone prosthesis. The bone properties depend on fracture location and patient characteristics and medical history, such as age, diseases, and cellular behaviour [1].

The selection of the geometry, density and surface height must be evaluated depending on the characteristics of the patient using the prosthesis. The next subchapter contains an example, with a comparison between two types of bones and the simulated Iron specimens. The aim is to find the most appropriate specimens for the bones used as examples.

4.4 Comparison of FEA models - Iron specimens and bone

To understand the relevance of FEA in medical application, the results obtained were applied to a specific case. The geometries were compared with two bone tissue types: cortical and trabecular.

This analysis shows the potential of this methodology, supporting informed decisions in the production of medical devices such as osteosynthesis plates. As mentioned in chapter 2, bones can be different according to age, diseases, and cellular behaviour [1] and have different locations with different properties. This methodology helps to understand which is the best geometry and relative density to be used in different scenarios.

Trabecular and cortical bones were considered for this analysis. The composition, density and porosity are the main differences, making the properties and the use of both bones different, as mentioned in Section 2.2 [34].

A FEA of bone under bending was conducted, and the properties of both types of bones were retrieved from literature [106–108]. The constraints applied were the same as the specimens and the bone had the same dimension as the specimen, this is due to the direct influence of the geometry in bending. The simulations were compared with the FEA of the RTCO and TO Iron specimens. The results of the simulations are presented as a force-displacement curve in Figures 4.38 and 4.39.

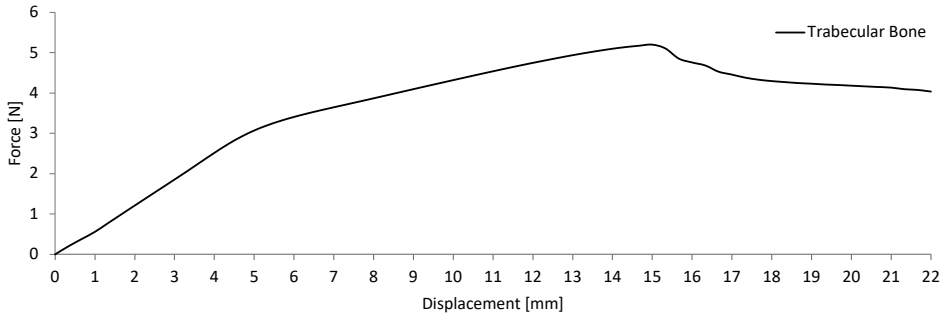

Figure 4.38: Force-displacement curve of FEA of trabecular bone.

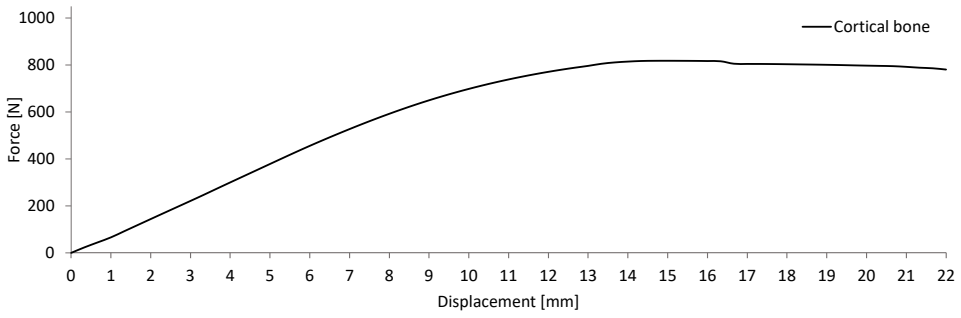

Figure 4.39: Force-displacement curve of FEA of cortical bone.

4.4.1 Trabecular Bone

In Section 2.2, the trabecular bone is considered to be an anisotropic composite material, with high porosity and with low density [34]. For this study, the Ash density used in the simulations was 0,1667 g/mm^3, retrieved from Öhman Mägi et al., Dalstra et al. and Røhl et al. [106–108].

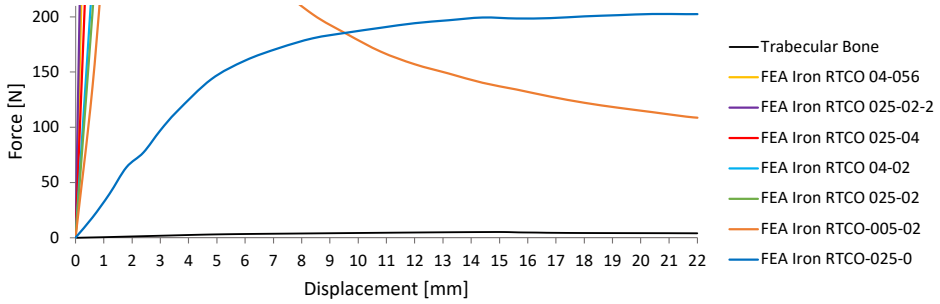

Figure 4.40: Force-displacement curve of FEA of trabecular bone and RTCO Iron samples.

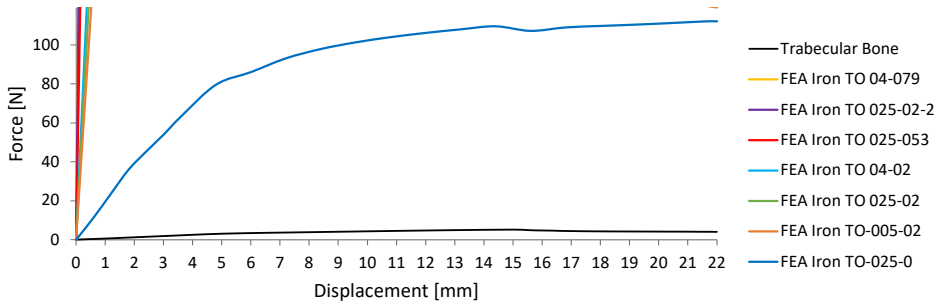

Figure 4.41: Force-displacement curve of FEA of trabecular bone and TO Iron samples.

The maximum reaction force and the stiffness values of the trabecular bone are very low compared with the values from the RTCO and TO samples, as seen similarly in Figures 4.40 and 4.41.

The MRF and the k of the trabecular bone are much lower than the samples being studied. The specimens that fit the best are the RTCO-025-0 and TO-025-0, being the latter the best. However, the MRF and the k difference between the trabecular FEA and the samples, (Figures 4.40 and 4.41) is about 360% higher in RTCO and 200% higher in TO, making it unsuitable for this bone, since all the samples will cause stress shielding.

4.4.2 Cortical Bone

The FEA of the cortical bone is presented in the Figure 4.39. As mentioned above, since the cortical has higher density and lower porosity, the MRF and k values are higher than the trabecular bone. The ash density used was 0,83 g/cm^3, retrieved from Öhman Mägi et al., Dalstra et al. and Røhl et al. [106–108].

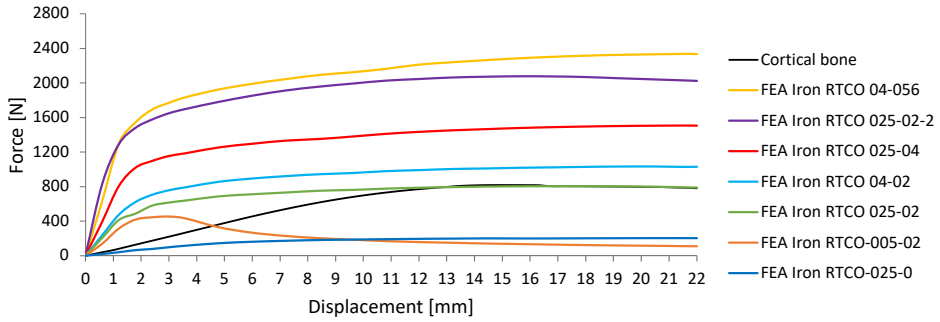

Figure 4.42: Force-displacement curve of FEA of cortical bone and RTCO Iron samples.

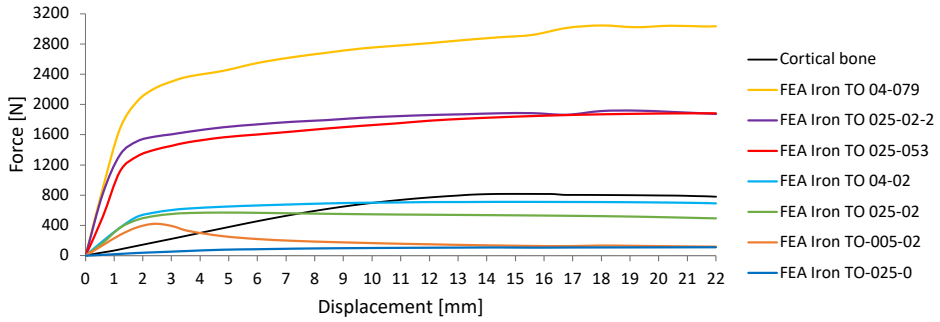

Figure 4.43: Force-displacement curve of FEA of cortical bone TO Iron samples.

Despite the superior mechanical properties of the cortical bone, the stiffness is still relatively low in comparison with the RTCO and TO samples. However, the plastic regime can be similar depending on the type of cell and the relative density.

The principal concern while matching the bone being studied and the prosthesis is the stress shielding that can occur. The prosthesis must have slightly superior mechanical behaviours in order to maintain the bones in place, and must not deform permanently easily (meaning enter the plastic regime). To accomplish this, the stiffness and the maximum reaction force in the elastic regime must be sufficiently higher than the fractured bone.

To accomplish the best results, the prosthesis' stiffness must be slightly higher than the bone, to avoid stress shielding. That happens with two scenarios presented in Figures 4.42 and 4.43, with the samples RTCO-025-02 and TO-04-02, respectively.

In the RTCO-025-0, RTCO-005-02, TO-005-02 and TO-025-0 models, the elastic regime is lower and would deform before the bone, making it no suitable for this application. The RTCO-04-056, RTCO-025-02-2, RTCO-025-04 RTCO-04-02, TO-04-079, TO-025-02-2 and TO-025-053 are not suitable for this application since the mechanical behaviour is higher than the bone being studied causing stress shielding. (Figures 4.42 and 4.43). The RTCO-025-02 and TO-04-02 are suitable for this application.

5

Conclusions

In this section, the conclusions of the present thesis are presented, as well as future work.

5.1 Conclusions

As people are living longer, orthopaedic health issues rise. Bones lose the ability to regenerate with age, increasing the risk of fractures [2]. Prostheses and plates have been used for decades to help regenerate fractures. Recently, temporary prostheses and cellular structures have evolved to be implemented in medical use. Two unit cell geometries were studied based on Chantarapanich et al. [84], since the RTCO and TO had the best mechanical behaviour in the compression tests in Castresana Olleta [20]. These cells were further studied in the present dissertation. Numerical simulations and laboratory tests were conducted using the three-point bending method with specimens of varying relative densities and surface heights. The results from these investigations are in agreement with most models.

The materials used for the study of the samples were Stainless Steel and Iron. To proceed with the validation of the model, Stainless Steel FEA and lab experiments were conducted and compared. For the final application of the methodology expressed in Chapter 3, FEA of Iron samples and different types of bone were executed.

The main goal of the present thesis was to understand and find the superior mechanically behaved cell and to validate the methodology to be applied in the future, where the main goal is to match a structure to be used in prostheses depending on the patients' condition.

The computational model is able to represent accurately the mechanical behaviour of the samples in bending. Most of the samples have less than 5% of relative error when comparing FEA with the lab tests, and despite some of them being above 5%, the values are not above the acceptable relative error percentage for computational model validation studied by Liu et al. [102]. This model yields accurate predictions to support informed design decisions on prostheses' materials and geometric parameters produced by AM for bone fracture treatment applications.

From the FEA and lab test, it is possible to obtain the mechanical behaviour parameters of each type

of cell and compare them:

- When having the same relative density and surface height, the RTCO cells are more stable and have higher mechanical properties such as k and E_a.
- The presence of the outer surfaces and their heights plays an important role in the RF, k and E_a values. The higher the surface, the higher the influence it has on the mechanical behaviour, with the cells having a lower contribution. This is observable in Section 4.2 where, despite the superior mechanical behaviour of RTCO cell geometry (relative to TO unit cell with the same density, but different surface height), the TO presents superior properties, even though is the worst cell of the two.
- The RTCO-005-02 and TO-005-02, (samples with less relative density) are not stable, as seen in Section 4.1. These models have higher relative error percentage. In Figure 4.4, the shape of the curve has a peak indicating that the structure's strength decreases abruptly and buckles. In the lab, these were the only samples presenting fractures in the cells' structure.
- The surface plays an important role. There is an increase of 61% - 95% of Energy absorption when using outer surfaces (Figures 4.12 and 4.13).
- The number of rows has a direct influence on the amount of stress supported by the outer surfaces. The higher the number of rows, the lower the load the outer surface is going to be able to support.
- Excluding the samples with 5% relative density, all of the other cells are stable and can be used in prostheses or plates. The selection depends on the characteristics of the fracture being treated, on each patient's characteristics and on the bone type.

Last but not least, the methodology presented in Figure 3.1 shows that is possible to adopt the use of FEA, in a methodical manner, to make informed decisions about the implementation of prosthesis and its characteristics, such as shape, density, size and material, to a specific scenario.

Allying the FEA of the samples and the bone can give insights into which is the best geometry, relative density and surface height for each case, minimizing the mismatch of elastic properties (stress shielding) between bone and implant and avoiding stress shielding. This can only be possible due to the results of the computational model validation in Section 4.1.

The methodology presented in this work highlights the possibility of tailoring mechanical properties to the patient's needs through Iron-based porous structures produced via AM. Patient-tailored implants provide the optimal solution for each individual. Through AM and the application of appropriate design methodology, it is possible to provide the ideal prostheses.

5.2 Future Work

As mentioned in Chapter 2, there are many factors in need of analysis to safely and effectively produce medical equipment.

Since this thesis is framed in the project ”GradImp - Implantes biodegradáveis em ferro poroso obtidos por fabrico aditivo”, FCT PTDC/CTM-CTM/3354/2021, several studies can be further made.

Compression and bending have been already studied, however, bones have other types of stress states applied. Therefore, further mechanical behaviour tests are recommended, such as torsion. FEA and lab tests can be done to understand the behaviour of the unit cells under torsion.

In a single bone, the material properties can be different. Gradients in the lattice structure can be studied to mimic different properties, through the use of different relative densities within the same part. This allows the production of different cell densities in the same prosthesis or plates.

The interaction of the surface or cells of the prosthesis with the soft and hard tissues should be analysed, as prostheses produced by AM. Therefore, a tribological FEA analysis could be performed, contemplating roughness, corrosion, fatigue and rate of biodegradation of the prosthesis.

With the information gathered from the GradImp project, at this point, it is possible to propose the development, design, FEA and production of plates and similar implants based on pure iron produced by AM involving cellular structures.

Bibliography

[1] L. García-Prat, E. Perdiguero, S. Alonso-Martín, S. Dell'Orso, S. Ravichandran, S. R. Brooks, A. H. Juan, S. Campanario, K. Jiang, X. Hong, L. Ortet, V. Ruiz-Bonilla, M. Flández, V. Moiseeva, E. Rebollo, M. Jardí, H.-W. Sun, A. Musarò, M. Sandri, A. del Sol, V. Sartorelli, and P. Muñoz-Cánoves, "FoxO maintains a genuine muscle stem-cell quiescent state until geriatric age," *Nature Cell Biology*, vol. 22, no. 11, pp. 1307–1318, 2020. DOI: 10.1038/s41556-020-00593-7

[2] S. E. Iismaa, X. Kaidonis, A. M. Nicks, N. Bogush, K. Kikuchi, N. Naqvi, R. P. Harvey, A. Husain, and R. M. Graham, "Comparative regenerative mechanisms across different mammalian tissues," *Regenerative Medicine*, vol. 3, no. 1, p. 6, 2018-02-23. DOI: 10.1038/s41536-018-0044-5

[3] T. Shisha, "Parameters for defining efficacy in fracture healing," *Clin Cases Miner Bone*, vol. 7, 2010.

[4] B. Huzum, B. Puha, R. Necoara, S. Gheorghevici, G. Puha, A. Filip, P. Sirbu, and O. Alexa, "Biocompatibility assessment of biomaterials used in orthopedic devices: An overview (review)," *Experimental and Therapeutic Medicine*, vol. 22, no. 5, p. 1315, 2021. DOI: 10.3892/etm.2021.10750

[5] E. Borgiani, G. N. Duda, and S. Checa, "Multiscale modeling of bone healing: Toward a systems biology approach," *Frontiers in Physiology*, vol. 8, p. 287, 2017. DOI: 10.3389/fphys.2017.00287

[6] M. S. Ghiasi, J. Chen, A. Vaziri, E. K. Rodriguez, and A. Nazarian, "Bone fracture healing in mechanobiological modeling: A review of principles and methods," *Bone Reports*, vol. 6, pp. 87–100, 2017. DOI: 10.1016/j.bonr.2017.03.002

[7] M. Fatima, H. Canhao, and J. Eurico, "Bone: A composite natural material," in *Advances in Composite Materials - Analysis of Natural and Man-Made Materials*, P. Tesinova, Ed. InTech, 2011. DOI: 10.5772/17523

[8] A. Bigham-Sadegh and A. Oryan, "Basic concepts regarding fracture healing and the current options and future directions in managing bone fractures: Bone healing biology," *International Wound Journal*, vol. 12, no. 3, pp. 238–247, 2015. DOI: 10.1111/iwj.12231

[9] F. Wu, B. Mason, A. Horne, R. Ames, J. Clearwater, M. Liu, M. C. Evans, G. D. Gamble, and I. R. Reid, "Fractures between the ages of 20 and 50 years increase women's risk of subsequent fractures," *Archives of Internal Medicine*, vol. 162, no. 1, p. 33, 2002-01-14. DOI: 10.1001/archinte.162.1.33

[10] W. Ai-Min, C. Bisignano, S. L. James, G. G. Abady, A. Abedi, E. Abu-Gharbieh, R. K. Alhassan, V. Alipour, J. Arabloo, M. Asaad, W. N. Asmare, A. F. Awedew, M. Banach, S. K. Banerjee, A. Bijani, T. T. Birhanu, S. R. Bolla, L. A. Cámera, J.-C. Chang, D. Y. Cho, M. T. Chung, R. A. S. Couto, X. Dai, L. D. R. Dandona, F. Farzadfar, I. Filip, F. Fischer, A. A. Fomenkov, T. K. Gill, B. Gupta, J. A. Haagsma, A. Haj-Mirzaian, S. Hamidi, S. I. Hay, I. M. Ilic, M. D. Ilic, R. Q. Ivers, M. Jürisson, R. Kalhor, T. Kanchan, T. Kavetskyy, R. Khalilov, E. A. Khan, M. Khan, C. J. Kneib, V. Krishnamoorthy, G. A. Kumar, N. Kumar, R. Lallo, S. Lasrado, L. S. S, Z. Liu, A. Manafi, N. Manafi, R. G. Menezes, T. J. Meretoja, B. Miazgowski, T. R. Miller, Y. Mohammad, A. Mohammad-Hafshejani, A. H. Mokdad, C. J. L. Murray, M. Naderi, M. D. Naimzada, V. C. Nayak, N. C. Tat, N. Rajan, A. T. Olagunju, N. Otstavnov, S. S. Otstavnov, J. R. Padubidri, J. Pereira, H. Q. Pham, M. Pinheiro, S. Polinder, H. Pourchamani, N. Rabiee, A. Radfar, M. H. U. Rahman, D. L. Rawaf, S. Rawaf, M. R. Saeb, A. M. Samy, L. S. Riera, D. C. Schwebel, S. Shahabi, M. A. Shaikh, A. Soheili, R. Tabarés-Seisdedos, M. R. Tovani-Palone, B. X. Tran, R. S. Travillian, P. R. Valdez, T. J. Vasankari, D. Z. Velazquez, N. Venketasubramanian, G. T. Vu, Z.-J. Zhang, and T. Vos, “Global, regional, and national burden of bone fractures in 204 countries and territories, 1990–2019: a systematic analysis from the global burden of disease study 2019,” *The Lancet Healthy Longevity*, vol. 2, no. 9, pp. e580–e592, 2021-09. DOI: 10.1016/S2666-7568(21)00172-0

[11] S. Amin, S. J. Achenbach, E. J. Atkinson, S. Khosla, and L. J. Melton, “Trends in fracture incidence: A population-based study over 20 years: FRACTURE TRENDS,” *Journal of Bone and Mineral Research*, vol. 29, no. 3, pp. 581–589, 2014-03. DOI: 10.1002/jbmr.2072

[12] R. Dimitriou, E. Jones, D. McGonagle, and P. V. Giannoudis, “Bone regeneration: current concepts and future directions,” *BMC Medicine*, vol. 9, no. 1, p. 66, 2011-12. DOI: 10.1186/1741-7015-9-66

[13] P. J. Prendergast, R. Huiskes, and K. Søballe, “Biophysical stimuli on cells during tissue differentiation at implant interfaces,” *Journal of Biomechanics*, vol. 30, no. 6, pp. 539–548, 1997. DOI: 10.1016/S0021-9290(96)00140-6

[14] K. Søballe, “Hydroxyapatite ceramic coating for bone implant fixation: Mechanical and histological studies in dogs,” *Acta Orthopaedica Scandinavica*, vol. 64, pp. 1–58, 1993-01. DOI: 10.3109/17453679309155636

[15] D. R. Carter, G. S. Beaupr, N. J. Giori, and J. A. Helms, “Mechanobiology of skeletal regeneration:,” *Clinical Orthopaedics and Related Research*, vol. 355S, pp. S41–S55, 1998-10. DOI: 10.1097/00003086-199810001-00006

[16] C. Pan, Y. Han, and J. Lu, “Design and optimization of lattice structures: A review,” *Applied Sciences*, vol. 10, no. 18, p. 6374, 2020-09-13. DOI: 10.3390/app10186374

[17] W. Tao and M. C. Leu, “Design of lattice structure for additive manufacturing,” in *2016 International Symposium on Flexible Automation (ISFA)*. IEEE, 2016-08, pp. 325–332. DOI: 10.1109/ISFA.2016.7790182

[18] K. S. Ødegaard, J. Torgersen, and C. W. Elverum, “Structural and biomedical properties of common additively manufactured biomaterials: A concise review,” *Metals*, vol. 10, no. 12, p. 1677, 2020-12-15. DOI: 10.3390/met10121677

[19] M. Alonzo, F. Alvarez Primo, S. Anil Kumar, J. A. Mudloff, E. Dominguez, G. Fregoso, N. Ortiz, W. M. Weiss, and B. Joddar, "Bone tissue engineering techniques, advances, and scaffolds for treatment of bone defects," *Current Opinion in Biomedical Engineering*, vol. 17, p. 100248, 2021-03. DOI: 10.1016/j.cobme.2020.100248

[20] K. Castresana Olleta, "Additive manufacturing of metallic bone implants," *Master's Thesis, Instituto Superior Técnico, Escuela politécnica superior de Mondragon Unibertsitatea*, 2021.

[21] A. Jain, "Research in orthopedics: A necessity," *Indian Journal of Orthopaedics*, vol. 43, no. 4, p. 315, 2009. DOI: 10.4103/0019-5413.55968

[22] M. Hua, D. Myers, and L. Host, "The impact of orthopaedic research evidence on health financing in australia," *Health Research Policy and Systems*, vol. 16, no. 1, p. 36, 2018-12. DOI: 10.1186/s12961-018-0314-0

[23] M. R. McClung, "The relationship between bone mineral density and fracture risk," *Current Osteoporosis Reports*, vol. 3, no. 2, pp. 57–63, 2005-06. DOI: 10.1007/s11914-005-0005-y

[24] J. Li, M. A. Kacena, and D. L. Stocum, "Fracture healing," pp. 235–253, 2019. DOI: 10.1016/B978-0-12-813259-3.00012-9

[25] L. Claes and C. Heigele, "Magnitudes of local stress and strain along bony surfaces predict the course and type of fracture healing," *Journal of Biomechanics*, vol. 32, no. 3, pp. 255–266, 1999-03. DOI: 10.1016/S0021-9290(98)00153-5

[26] Q. M. Ud Din, "Effect of biomaterial prosthetics on the rehabilitation of lower limb amputees," *Biomedical Journal of Scientific & Technical Research*, vol. 1, no. 4, 2017-09-18. DOI: 10.26717/BJSTR.2017.01.000362

[27] S. Madhanagopal, M. Burns, D. Pei, R. Mukundhan, H. Meyerson, and R. Vinjamuri, "Introductory chapter: Past, present, and future of prostheses and rehabilitation," in *Prosthesis*, R. Vinjamuri, Ed. IntechOpen, 2020-02-05. DOI: 10.5772/intechopen.89987

[28] P. Kloen and D. Ring, "AO - association of the study of internal fixation," *Copyright © 2023 - AO Foundation, Clavadelerstrasse 8, 7270 Davos, Switzerland*, 2023. DOI: https://surgeryreference.aofoundation.org/

[29] R. Chidambaram and D. Mok, "SHOULD RECONSTRUCTION PLATES BE USED IN THE MANAGEMENT OF CLAVICULAR FRACTURES?" *Orthopaedic Proceedings*, vol. 85-B, pp. 70–70, 2003. DOI: 10.1302/0301-620X.85BSUPP_I.0850070b

[30] A. A. Padron, J. R. Owen, J. S. Wayne, S. A. Aktay, and R. F. Barnes, "In vitro biomechanical testing of the 3.5 mm LCP in torsion: a comparison of unicortical locking to bicortical nonlocking screws placed nearest the fracture gap," *BMC Research Notes*, vol. 10, no. 1, p. 768, 2017-12. DOI: 10.1186/s13104-017-3102-y

[31] M. Y. Khalid, A. Al Rashid, Z. U. Arif, W. Ahmed, H. Arshad, and A. A. Zaidi, "Natural fiber reinforced composites: Sustainable materials for emerging applications," *Results in Engineering*, vol. 11, p. 100263, 2021-09. DOI: 10.1016/j.rineng.2021.100263

[32] B. E. Fabien, N. Boris, and A. Ateba, “Review article a literature review on natural fibers, its properties and influence of water absorption on mechanical properties of composites,” *International journal of Recent Advance in Multidisciplinary Research*, 2019.

[33] X. Feng, “Chemical and biochemical basis of cell-bone matrix interaction in health and disease,” *Current Chemical Biology*, vol. 3, no. 2, pp. 189–196, 2009-05-01. DOI: 10.2174/187231309788166398

[34] E. F. Morgan, G. U. Unnikrisnan, and A. I. Hussein, “Bone mechanical properties in healthy and diseased states,” *Annual Review of Biomedical Engineering*, vol. 20, no. 1, pp. 119–143, 2018-06-04. DOI: 10.1146/annurev-bioeng-062117-121139

[35] H. Williams, J. T. Gebhardt, M. D. Tokach, J. C. Woodworth, J. M. DeRouchey, R. D. Goodband, J. R. Bergstrom, C. W. Hastad, Z. Post, M. Rahe, C. Siepker, P. Sitthicharoenchai, and S. Ensley, “260 the effect of different bones and analytical methods on assessment of bone mineralization response to dietary p, phytase, and vitamin d in finishing pigs,” *Journal of Animal Science*, vol. 100, pp. 113–114, 2022-09-22. DOI: 10.1093/jas/skac247.218

[36] N. A. Johanson, M. E. Charlson, L. Cutignola, M. Neves, E. F. DiCarlo, and P. G. Bullough, “Femoral neck bone density,” *The Journal of Arthroplasty*, vol. 8, no. 6, pp. 641–652, 1993-12. DOI: 10.1016/0883-5403(93)90013-T

[37] T. P. Doan-Nguyen and D. Crespy, “Advanced density-based methods for the characterization of materials, binding events, and kinetics,” *Chemical Society Reviews*, vol. 51, no. 20, pp. 8612–8651, 2022. DOI: 10.1039/D1CS00232E

[38] A. Oliveira, L. Reis, M. Leite, F. Alves, A. Moita De Deus, M. Sardinha, and M. F. Vaz, “Evaluation of cellular structures with triply periodic minimal surfaces fabricated by additive manufacturing,” *Engineering Manufacturing Letters*, vol. 1, no. 1, pp. 28–33, 2022-04-21. DOI: 10.24840/2795-5168_001-001_0006

[39] W. Lin, O. Tadai, M. Takahashi, D. Sato, T. Hirose, W. Tanikawa, Y. Hamada, and K. Hatakeda, “An experimental study on measurement methods of bulk density and porosity of rock samples,” *Journal of Geoscience and Environment Protection*, vol. 03, no. 5, pp. 72–79, 2015. DOI: 10.4236/gep.2015.35009

[40] S. Ritter, “Mixing it up: Materials science: New metal-organic framework features unprecedented porosity and surface area,” *Chemical Engineering News*, 2007. DOI: 10.1021/cen-v085n052.p010a

[41] D. Leguillon, E. Martin, and M.-C. Lafarie-Frenot, “Flexural vs. tensile strength in brittle materials,” *Comptes Rendus Mécanique*, vol. 343, no. 4, pp. 275–281, 2015-04. DOI: 10.1016/j.crme.2015.02.003

[42] L. Griffin, J. Gibeling, R. Martin, V. Gibson, and S. Stover, “The effects of testing methods on the flexural fatigue life of human cortical bone,” *Journal of Biomechanics*, vol. 32, no. 1, pp. 105–109, 1999-01. DOI: 10.1016/S0021-9290(98)00151-1

[43] R. P. Hubbard, “Flexure of layered cranial bone,” *Journal of Biomechanics*, vol. 4, no. 4, pp. 251–263, 1971-07. DOI: 10.1016/0021-9290(71)90031-5

[44] N. H. Hart, S. Nimphius, T. Rantalainen, A. Ireland, A. Siafarikas, and R. U. Newton, “Mechanical basis of bone strength: influence of bone material, bone structure and muscle action,” *Musculoskelet Neuronal Interact*, 2017.

[45] D. D. Kiradzhiyska and R. D. Mantcheva, “Overview of biocompatible materials and their use in medicine,” *Folia Medica*, vol. 61, no. 1, pp. 34–40, 2019-03-01. DOI: 10.2478/folmed-2018-0038

[46] A. Hudecki, G. Kiryczyński, and M. J. Łos, “Biomaterials, definition, overview,” in *Stem Cells and Biomaterials for Regenerative Medicine*. Elsevier, 2019, pp. 85–98. DOI: 10.1016/B978-0-12-812258-7.00007-1

[47] Technical Committee ISO/TC 194, *Biological evaluation of medical devices*.

[48] M. Salama, D. Rechena, L. Reis, A. Deus, C. Santos, M. Carmezim, and M. Vaz, “Effect of the topology on the mechanical properties of porous iron immersed in body fluids,” *Proceedings of the Institution of Mechanical Engineers, Part L: Journal of Materials: Design and Applications*, vol. 235, no. 5, pp. 1066–1076, 2021-05. DOI: 10.1177/1464420720987860

[49] A. Costa, L. N. Liberato, P. Palestra, and G. Barosi, “Small-dose iron tolerance test and body iron content in normal subjects,” *European Journal of Haematology*, vol. 46, no. 3, pp. 152–157, 2009-04-24. DOI: 10.1111/j.1600-0609.1991.tb01269.x

[50] L. J. Gibson, “Cellular solids,” *MRS Bulletin*, vol. 28, no. 4, pp. 270–274, 2003-04. DOI: 10.1557/mrs2003.79

[51] L. J. Gibson, M. F. Ashby, and B. A. Harley, *Cellular materials in nature and medicine*. Cambridge University Press, 2010, isbn: 978-0-521-19544-7.

[52] O. Al-Ketan, R. Rowshan, and R. K. Abu Al-Rub, “Topology-mechanical property relationship of 3d printed strut, skeletal, and sheet based periodic metallic cellular materials,” *Additive Manufacturing*, vol. 19, pp. 167–183, 2018-01. DOI: 10.1016/j.addma.2017.12.006

[53] A. Shrivastava, “3 - plastic properties and testing,” in *Introduction to Plastics Engineering*, ser. Plastics Design Library, A. Shrivastava, Ed. William Andrew Publishing, 2018, pp. 49–110. DOI: 10.1016/B978-0-323-39500-7.00003-4

[54] B. C. Chakraborty and D. Ratna, “Chapter 6 - experimental techniques and instruments for vibration damping,” in *Polymers for Vibration Damping Applications*, B. C. Chakraborty and D. Ratna, Eds. Elsevier, 2020, pp. 281–325. DOI: 10.1016/B978-0-12-819252-8.00006-9

[55] ASTM D20.10 Committee, *Standard Test Methods for Flexural Properties of Unreinforced and Reinforced Plastics and Electrical Insulating Materials*. DOI: 10.1520/D0790-03

[56] ASTM D30.04 Committee, *Standard Test Method for Flexural Properties of Polymer Matrix Composite Materials*. DOI: 10.1520/D7264_D7264M-07

[57] Technical Committee ISO/TC 61/SC 2, *Plastics - Determination of flexural properties*.

[58] ASTM D30 Committee, *Test Method for Core Shear Properties of Sandwich Constructions by Beam Flexure*. DOI: 10.1520/C0393_C0393M-11

[59] M. Ueda and M. Akiyama, “Compression test of a single carbon fiber in a scanning electron microscope and its evaluation via finite element analysis,” *Advanced Composite Materials*, vol. 28, no. 1, pp. 57–71, 2019-01-02. DOI: 10.1080/09243046.2018.1433506

[60] Z. Pater, P. Walczuk, K. Lis, and L. Wójcik, “PRELIMINARY ANALYSIS OF a ROTARY COMPRESSION TEST,” *Advances in Science and Technology Research Journal*, vol. 12, no. 2, pp. 77–82, 2018-06-01. DOI: 10.12913/22998624/86812

[61] Shahbeyk, Voyiadjis, Habibi, Astaneh, and Yaghoobi, “Review of size effects during micropillar compression test: Experiments and atotic simulations,” *Crystals*, vol. 9, no. 11, p. 591, 2019-11-10. DOI: 10.3390/cryst9110591

[62] ASTM E28 Committee, *Standard Test Methods of Compression Testing of Metallic Materials at Room Temperature*. DOI: 10.1520/E0009-09

[63] K. K. Pradhan and S. Chakraverty, “Finite element method,” in *Computational Structural Mechanics*. Elsevier, 2019, pp. 25–28. DOI: 10.1016/B978-0-12-815492-2.00010-1

[64] B. E. Rapp, “Finite element method,” in *Microfluidics: Modelling, Mechanics and Mathematics*. Elsevier, 2017, pp. 655–678. DOI: 10.1016/B978-1-4557-3141-1.50032-0

[65] K. Uchino, “Overview of the ATILA finite element method (FEM) software code,” in *Applications of ATILA FEM Software to Smart Materials*. Elsevier, 2013, pp. 3–25e. DOI: 10.1533/9780857096319.1.3

[66] N. Zobeiry, J. Reiner, and R. Vaziri, “Theory-guided machine learning for damage characterization of composites,” *Composite Structures*, vol. 246, p. 112407, 2020. DOI: 10.1016/j.compstruct.2020.112407

[67] K. Rajaguru, T. Karthikeyan, and V. Vijayan, “Additive manufacturing – state of art,” *Materials Today: Proceedings*, vol. 21, pp. 628–633, 2020. DOI: 10.1016/j.matpr.2019.06.728

[68] M. Leary, “Design of titanium implants for additive manufacturing,” in *Titanium in Medical and Dental Applications*. Elsevier, 2018, pp. 203–224. DOI: 10.1016/B978-0-12-812456-7.00009-3

[69] Y. Xu, G. Han, G. Huang, T. Li, J. Xia, and D. Guo, “Properties evaluations of topology optimized functionally graded lattice structures fabricated by selective laser melting,” *Materials*, vol. 16, no. 4, p. 1700, 2023-02-17. DOI: 10.3390/ma16041700

[70] M. Rybachuk, C. Alice Mauger, T. Fiedler, and A. Öchsner, “Anisotropic mechanical properties of fused deposition modeled parts fabricated by using acrylonitrile butadiene styrene polymer,” *Journal of Polymer Engineering*, vol. 37, no. 7, pp. 699–706, 2017-08-28. DOI: 10.1515/polyeng-2016-0263

[71] C. Patil, P. D. Sonawane, M. Naik, and D. G. Thakur, “Finite element analysis of flexural test of additively manufactured components fabricated by fused deposition modelling,” in *AIP Conference Proceedings 2311, 070026*, 2020, p. 070026. DOI: 10.1063/5.0034306

[72] ASTM F42.91 Committee, *Standard Terminology for Additive Manufacturing Technologies*. DOI: 10.1520/F2792-12

[73] D. Pereira, F. P. Alves, L. Reis, M. Leite, A. M. Deus, M. Sardinha, and M. F. Vaz, “Cellular lattice cores of sandwich panels fabricated by additive manufacturing: Effect of dimensions and relative density on mechanical behaviour,” *Proceedings of the Institution of Mechanical Engineers, Part L: Journal of Materials: Design and Applications*, vol. 237, no. 5, pp. 1188–1201, 2023-05. DOI: 10.1177/14644207221138003

[74] J. P. Davim and K. Gupta, Eds., *Addictive Manufacturing*, ser. Handbooks in Adavanced Manufacturing. Elsevier, 2021.

[75] M. Gieseke, D. Albrecht, C. Nölke, S. Kaierle, O. Suttmann, and L. Overmeyer, “Laserbasierte technologien,” in *3D-Druck beleuchtet*, R. Lachmayer, R. B. Lippert, and T. Fahlbusch, Eds. Springer Berlin Heidelberg, 2016, pp. 19–30. DOI: 10.1007/978-3-662-49056-3_3

[76] R. K. Shastri, C. P. Mohanty, S. Dash, K. M. P. Gopal, A. R. Annamalai, and C.-P. Jen, “Reviewing performance measures of the die-sinking electrical discharge machining process: Challenges and future scopes,” *Nanomaterials*, vol. 12, no. 3, p. 384, 2022-01-25. DOI: 10.3390/nano12030384

[77] S. K. Padhi, S. S. Mahappatra, and H. C. Das, “Performance of a copper electroplated plastic electrical discharge machining electrode compared to a copper electrode,” *International Journal of Pure and Applied Mathematics*, 2017.

[78] J. Geroge and M. K K, “Optimization of sustainable electrical discharge machining using TOPSIS - entropy weight method: An integrated approach,” *SSRN Electronic Journal*, 2020. DOI: 10.2139/ssrn.3791069

[79] C. Gnanavel, R. Saravanan, M. Chandrasekaran, and R. Pugazhenthi, “Restructured review on electrical discharge machining - a state of the art,” *IOP Conference Series: Materials Science and Engineering*, vol. 183, p. 012015, 2017-03. DOI: 10.1088/1757-899X/183/1/012015

[80] C. R. Mahesha, R. Suprabha, S. Thenmozhi, V. Gowri, C. M. Chowdary, V. Savithiri, B. V. V. L. Kala Bharathi, R. Subbiah, and I. Komalnu Raghavan, “Optimizing the parameters of zirconium carbide and rice husk ash reinforced with AA 2618 composites,” *Advances in Materials Science and Engineering*, vol. 2022, pp. 1–11, 2022-09-21. DOI: 10.1155/2022/1962523

[81] K. KabiniS. and K. BojerS., “Effect of capacitance on electrical discharge machining using an rc type pulse generation circuit,” in *The Sustainable Research and Innovation (SRI) Conference*, 2015.

[82] S. O. Obadimu and K. I. Kourousis, “Compressive behaviour of additively manufactured lattice structures: A review,” *Aerospace*, vol. 8, no. 8, p. 207, 2021-07-30. DOI: 10.3390/aerospace8080207

[83] J. Zhang, H. Huang, G. Liu, H. Zong, and C. Zhang, “Stiffness and energy absorption of additive manufactured hybrid lattice structures,” *Virtual and Physical Prototyping*, vol. 16, no. 4, pp. 428–443, 2021-07-04. DOI: 10.1080/17452759.2021.1954405

[84] N. Chantarapanich, P. Puttawibul, S. Sucharitpwatskul, P. Jeamwatthanachai, S. Inglam, and K. Sitthiseripratip, “Scaffold library for tissue engineering: A geometric evaluation,” *Computational and Mathematical Methods in Medicine*, vol. 2012, pp. 1–14, 2012. DOI: 10.1155/2012/407805

[85] P. Sharma and P. M. Pandey, “Morphological and mechanical characterization of topologically ordered open cell porous iron foam fabricated using 3d printing and pressureless microwave sintering,” *Materials & Design*, vol. 160, pp. 442–454, 2018-12. DOI: 10.1016/j.matdes.2018.09.029

[86] P. Nogueira, K. Castresana, J. Magrinho, M. Silva, A. M. De Deus, and M. Vaz, “Computational evaluation of the compressive properties of different lattice geometries to be used as temporary implants,” *Procedia Computer Science*, vol. 217, pp. 928–937, 2023. DOI: 10.1016/j.procs.2022.12.290

[87] P. Nogueira, F. Vaz, B. Silva, A. M.Deus, and J. Magrinho, “Compression testing of Stainless Steel 316L samples produced by Additive Manufacturing, Instituto Superior Técnico, project ” GradImp - Implantes biodegrad´aveis em ferro poroso obtidos por fabrico aditivo”, FCT PTDC/CTM-CTM/3354/2021,” Internal Report, available upon request.

[88] ASTM E28.04 Committee, *Standard Test Methods of Compression Testing of Metallic Materials at Room Temperature*. DOI: 10.1520/E0009-19

[89] ASTM F42.05 Committee, *Standard Specification for Additive Manufacturing Stainless Steel Alloy (UNS S31603) with Powder Bed*. DOI: 10.1520/F3184-16

[90] ASTM A01.17 Committee, *Standard Specification for Stainless Steel Bars and Shapes*. DOI: 10.1520/A0276-13A

[91] P. Neves Manuel, “Finite element modelling of corrosion behavior,” *Master’s Thesis, Instituto Superior Técnico*, 2021.

[92] *M2 Series 5 Steel 316L Parameters for Concept Laser M2 Series 5*, GE Additive, 2021. DOI: https://www.ge.com/additive/sites/default/files/2021-02/M2SERIES5_316L_CMDS_20210209.pdf

[93] “Nof instituto superior técnico.” DOI: https://nof.tecnico.ulisboa.pt/rede-de-oficinas/oficina-de-mecanica/

[94] Q. uz Zaman Khan, M. Farhan, and A. Raza, “Progressive deterioration of reinforced concrete structures: effect on dynamic properties of flexural members,” *Multidiscipline Modeling in Materials and Structures*, 2023. DOI: 10.1108/mmms-01-2023-0003

[95] H. S. Hamid, R. Rahgozar, and A. A. Maghsoudi, “Flexural testing of high strength reinforced concrete beams strengthened with cfrp sheets,” *International Journal of Engineering, Transactions B: Applications*, vol. 22, pp. 131–146, 2008.

[96] S. Khalaf, A. O. E. Masri, F. Alhendi, and F. H. Abed, “Flexural response of cfst beams with incorporated dcls,” *2022 Advances in Science and Engineering Technology International Conferences (ASET)*, pp. 1–4, 2022. DOI: 10.1109/ASET53988.2022.9734909

[97] J. Sridhar, G. B. Shinde, D. Vivek, K. Naseem, P. Gaur, P. P. Patil, and M. T. Tesema, “Response surface methodology approach to predict the flexural moment of ferrocement composites with weld mesh and steel slag as partial replacement for fine aggregate,” *Advances in Materials Science and Engineering*, 2022. DOI: 10.1155/2022/9179480

[98] M. Aowad, A. Banik, C. Zhang, I. Kaiser, M. H. Khan, A. C. A. Almeida, D. Lazarenko, F. Khabaz, and K. T. Tan, “Flexural behavior and microstructural material properties of sandwich foam core under arctic temperature conditions,” *Journal of Sandwich Structures & Materials*, 2023. DOI: 10.1177/10996362231157016

[99] R. Marqués, J. Melchor, I. Sánchez-Montesinos, O. Roda, G. Rus, and P. Hernández-Cortés, “Biomechanical finite element method model of the proximal carpal row and experimental validation,” *Frontiers in Physiology*, vol. 12, p. 749372, 2022-01-24. DOI: 10.3389/fphys.2021.749372

[100] R. Mootanah, C. Imhauser, F. Reisse, D. Carpanen, R. Walker, M. Koff, M. Lenhoff, S. Rozbruch, A. Fragomen, Z. Dewan, Y. Kirane, K. Cheah, J. Dowell, and H. Hillstrom, “Development and validation of a computational model of the knee joint for the evaluation of surgical treatments for osteoarthritis,” *Computer Methods in Biomechanics and Biomedical Engineering*, vol. 17, no. 13, pp. 1502–1517, 2014-10-03. DOI: 10.1080/10255842.2014.899588

[101] K.-T. Kang, S.-H. Kim, J. Son, Y. H. Lee, and Y.-G. Koh, “Validation of a computational knee joint model using an alignment method for the knee laxity test and computed tomography,” *Bio-Medical Materials and Engineering*, vol. 28, no. 4, pp. 417–429, 2017-07-12. DOI: 10.3233/BME-171686

[102] L. Liu, P. Kamm, F. García-Moreno, J. Banhart, and D. Pasini, “Elastic and failure response of imperfect three-dimensional metallic lattices: the role of geometric defects induced by selective laser melting,” *Journal of the Mechanics and Physics of Solids*, vol. 107, pp. 160–184, 2017-10. DOI: 10.1016/j.jmps.2017.07.003

[103] M. Xu, D. Liu, P. Wang, Z. Zhang, H. Jia, H. Lei, and D. Fang, “In-plane compression behavior of hybrid honeycomb metastructures: Theoretical and experimental studies,” *Aerospace Science and Technology*, vol. 106, p. 106081, 2020-11. DOI: 10.1016/j.ast.2020.106081

[104] B. Proaño, H. Miyahara, K. Morishita, T. Matsumoto, H. Sakai, H. Noguchi, and S. Hamada, “Annealing effects on fracture process and tensile strength of non-combustible mg products fabricated by selective laser melting,” *Theoretical and Applied Fracture Mechanics*, vol. 120, p. 103411, 2022-08. DOI: 10.1016/j.tafmec.2022.103411

[105] M. F. Ashby, *Materials selection in mechanical design*, 2nd ed. Elsevier Butterworth-Heinemann, 2004. DOI: 10.1016/C2009-0-25539-5

[106] C. Öhman Mägi, O. Holub, D. Wu, R. M. Hall, and C. Persson, “Density and mechanical properties of vertebral trabecular bone—a review,” *JOR SPINE*, vol. 4, no. 4, p. e1176, 2021. DOI: 10.1002/jsp2.1176

[107] M. Dalstra, R. Huiskes, A. Odgaard, and L. van Erning, “Mechanical and textural properties of pelvic trabecular bone,” *Journal of Biomechanics*, vol. 26, no. 4, pp. 523–535, 1993. DOI: 10.1016/0021-9290(93)90014-6

[108] L. Røhl, E. Larsen, F. Linde, A. Odgaard, and J. Jørgensen, “Tensile and compressive properties of cancellous bone,” *Journal of Biomechanics*, vol. 24, no. 12, pp. 1143–1149, 1991. DOI: 10.1016/0021-9290(91)90006-9

[109] W. Masahiro, K. Dong-Hun, T. Takashi, and H. Jiro, “Wideband design of a short-slot 2-plane coupler by the mode matching/FEM hybrid analysis considering the structural symmetry,” *IEICE Trans. Commun.*, vol. 102-B, pp. 1019–1026, 2019. DOI: 10.1587/TRANSCOM.2018EBP3202

[110] M. Wakasa, D.-H. Kim, T. Tomura, and J. Hirokawa, “Mode matching/FEM hybrid analysis for a short-slot 2-plane coupler considering the structural symmetry,” *2017 International Symposium on Antennas and Propagation (ISAP)*, pp. 1–2, 2017. DOI: 10.1109/ISANP.2017.8228735

[111] T. Zhang, X.-X. Gong, L. Zhang, Y. Wang, Y. Liu, and L. Li, “A method for solving the additional stiffness introduced by flexible joints in stewart platform based on fem modal analysis,” *Machines*, 2023. DOI: 10.3390/machines11040457

[112] M. Zhang, S. Xue, H. Qin, Z. Kong, and Y. Ma, “The importance of FEM model for linearized EIT image reconstruction,” *2021 IEEE International Conference on Imaging Systems and Techniques (IST)*, pp. 1–6, 2021. DOI: 10.1109/IST50367.2021.9651335

[113] R. J. Talj, D. Hissel, R. Ortega, M. Becherif, and M. Hilairet, “Experimental validation of a PEM fuel-cell reduced-order model and a moto-compressor higher order sliding-mode control,” *IEEE Transactions on Industrial Electronics*, vol. 57, no. 6, pp. 1906–1913, 2010-06. DOI: 10.1109/TIE.2009.2029588

[114] W. D. Corte, K. V. Meirvenne, V. Boel, and L. Taerwe, “Design of anchorage zones of pretensioned concrete girders: A comparison of nonlinear 3d fem results with measurements on a full scale beam,” *Applied Sciences*, 2020. DOI: 10.3390/app10228221

[115] Y. Dewang and V. K. Sharma, “Effect of process parameters on thermo-mechanical behavior of extrusion of aluminum alloy,” *IJMSE*, 2021. DOI: 10.22068/ijmse.18.1.3

[116] Z. Li, “Modeling optimization research on numerical simulation of oil-pan forming process,” *Journal of Plasticity Engineering*, 2002.

[117] *Mechanical Behavior of As-Fabricated and UV-Cured Lattice Structures Printed Using the CLIP Technology*, ser. ASME International Mechanical Engineering Congress and Exposition, vol. Volume 2: Advanced Manufacturing, 11 2017. DOI: https://doi.org/10.1115/IMECE2017-70886

Appendix A - Symmetry sensitivity analysis

In FEM, to save computational time, symmetry analysis are performed. This type of analysis allows simplification of the model. The symmetry analysis is highly dependent on the geometry of the model and can reduce the size up to one-eighth of the original model. It is possible to obtain results without losing accuracy owing to the application boundary conditions that reflect the symmetry [109–111].

To simplify the analysis, two simplified geometries were used, using RTCO and TO cells. Despite the several relative densities for each geometry, to converge all of them would be very time-consuming, therefore the relative density chosen for the mesh convergence was 0.2, which is the average relative density between compact and dense specimens (50% and 3% relative density $\bar{\rho}$, respectively).

In bending, the mechanical behaviour of the specimen is complex, making it only possible to simplify the model up to one-fourth of the original size. Compression and tensile forces are applied in the y-axis, making it unfeasible to apply symmetry in the y-axis.

Hence the complexity of the test performed, which involves several mechanical behaviours due to bending, (compression and tensile forces) the model was simplified. The ratio between the length and width of the geometry was kept equal from the model used in the final simulations, the dimensions are 38.5 x 10.5 x 3.9 mm in the 1/1 model (11 cells in length, 3 cells in width and 1 cell plus 0.2 in each outer surface (x2)) and 19.25 x 5.25 x 3.9 mm in ¼ model (5,5 cells in length, 1,5 cells in width and 1 cell plus 0.2 in each outer surface (x2)), present in Figure A.1. To sum up, three symmetry models were tested in each geometry, 1/1, ½ and ¼, the representation of the geometries is presented in Figure A.1.

The variable used to evaluate the symmetry accuracy was the calculation of the error factor (Equation (A.1)) of the average displacement of four nodes presented in each model, presented in Figure A.2. The position of the nodes chosen aims to emulate the whole model and not just a localized region.

$$\text{Error}(\%) = \left| \frac{\bar{\Delta}_{M,i} - \bar{\Delta}_{M,i-1}}{\bar{\Delta}_{M,i-1}} \right| \times 100 \tag{A.1}$$

The $\Delta_{M,i}$ is the average displacement obtained in the mesh i, and $\Delta_{M,i-1}$ is the same but for the previous mesh.

The maximum relative error considered is 5%, to assume the accuracy of the further results

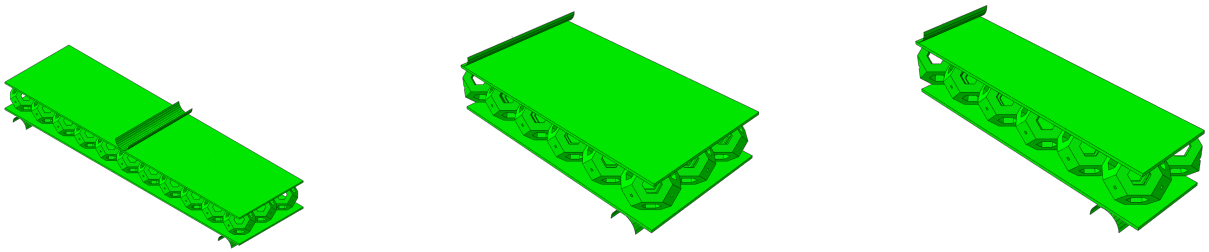

Figure A.1: TO Symmetry model (left) 1/1, represents the hole model, (centre) ½ model, is divided in the x-axis and, (right) ¼ model, is divided in the x and z-axis.

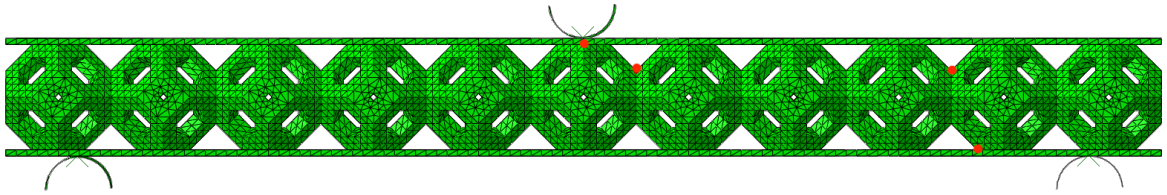

Figure A.2: Location of the nodes used in the calculation for the TO symmetry model 1/1, ½ and ¼ model.

Table A.1: Parameters regarding the TO geometry model in function of symmetry.

Symmetry model	Node nº	N º elements	Nº nodes	Computacional time [s]	Displacement [mm]	Average displacement [mm]	Relative error [%]	Average relative error [%]
1/1	1	300317	555860	6934	-0,1	-6,43E-02	-	-
	2				-0,09		-	
	3				-0,03		-	
	4				-0,37		-	
½	1	126679	232556	1409	-0,1	-6,39E-02	0,16	1,09
	2				-0,09		0,14	
	3				-0,03		3,24	
	4				-0,37		0,82	
¼	1	63187	117661	299	-0,1	-6,3E-02	0,45	2,88
	2				-0,09		0,86	
	3				-0,03		9,34	
	4				-0,04		0,88	

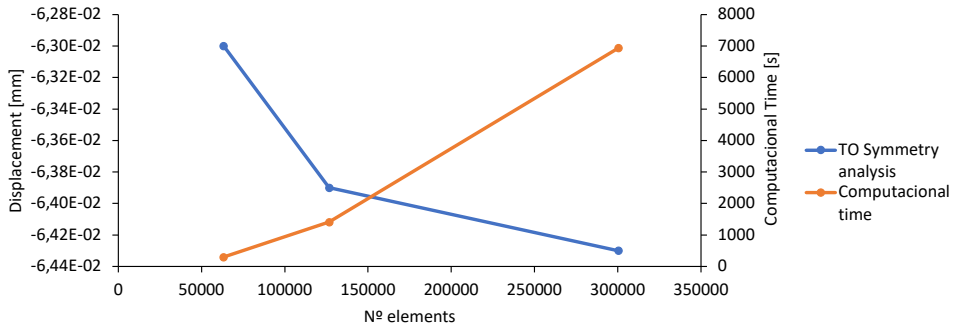

Figure A.3: TO average displacement and computational time symmetry analysis.

As seen in Table A.1 both ½ and ¼ TO's symmetry model had less than 5 % relative error, making it possible to use the symmetry model with less computational time. The ¼ model was chosen since it has a decrease of approximately 23.2% in computational time with only 2.88% of relative error.

The same analysis was conducted in the RTCO geometries, the symmetry models are represented in Figure A.4 and the location of the nodes are in Figure A.5.

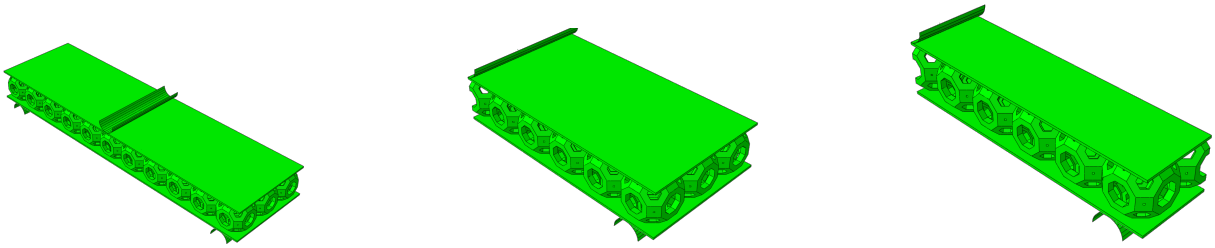

Figure A.4: RTCO Symmetry model (left) 1/1, represents the hole model, (centre) ½ model, is divided in the x-axis and, (right) ¼ model, is divided in the x and z-axis.

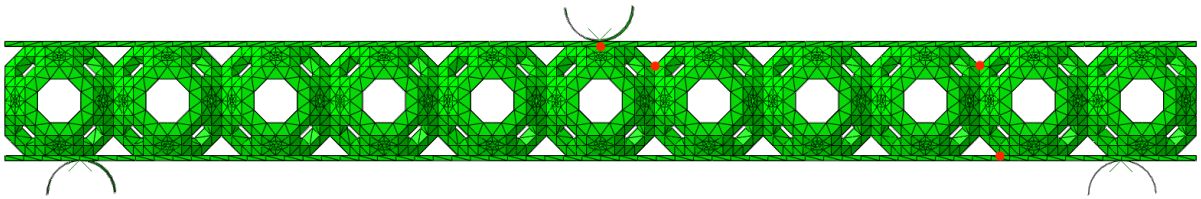

Figure A.5: Location of the nodes used in the calculation for the RTCO symmetry model 1/1, ½ and ¼ model.

Table A.2: Parameter regarding the RTCO geometry model in function of symmetry.

Model Partition	Node Nº	Nº Elements	Nº Nodes	Computacional Time [sec]	Displacement [mm]	Average Displacement [mm]	Relative Error [%]	Average Relative Error [%]
1/1	1	175914	322998	1261	-0,1	-7,25E-02	-	-
	2				-0,09		-	
	3				-0,03		-	
	4				-0,03		-	
½	1	99782	185290	489	-0,09	-7,27E-02	0,25	0,76
	2				-0,09		0,36	
	3				-0,03		2,21	
	4				-0,04		0,24	
¼	1	50910	94990	156	-0,1	-7,23E-02	0,42	0,50
	2				-0,09		0,06	
	3				-0,03		1,06	
	4				-0,04		0,47	

The same criteria were applied to the RTCO geometry, and all the symmetry models had less than 5% relative error, the ¼ model was chosen, since had a decrease of approximately 8% in computational time with only 0.5% of relative error.

To note, with this type of analysis, there is a factor of two and four in the ½ and ¼ model respectively, possible to observe in Figure A.5, where the reaction force is approximately two or four times less than the whole model. In

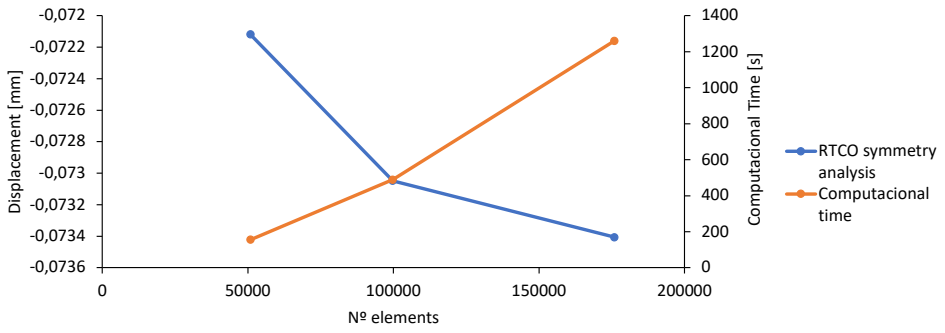

Figure A.6: RTCO average displacement and computational time symmetry analysis.

the final ¼ model, when calculating the reaction force with a model ¼ it is necessary to times four to get the real reaction force.

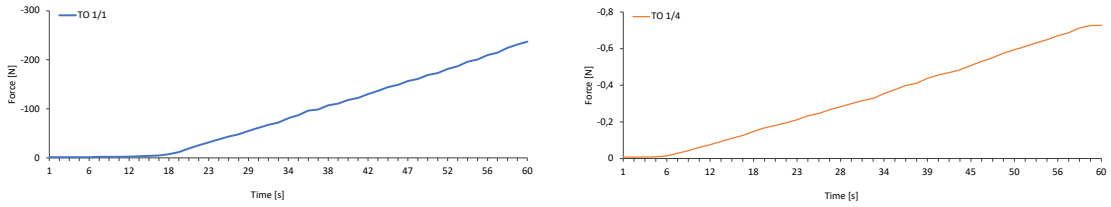

Figure A.7: Study of the impact of symmetry in values of reaction force taken out from (left) TO 1/1; reaction force -233.899 (right) TO ¼ reaction force -73.614.

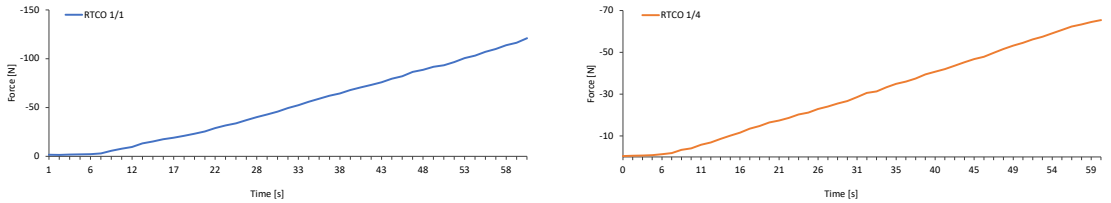

Figure A.8: Study of the impact of symmetry in values of reaction force taken out from (left) RTCO ½ reaction force -124.331 (right) RTCO ¼ reaction force -65.8479.

B

Appendix B - Mesh Convergence Analysis

To accurately represent the simulation model and to obtain the most reliable results without compromising the computational cost, it is necessary to perform a mesh convergence analysis.

As mentioned in Section 2.6, in order to run the simulation, it is necessary to have elements to do the iterations, therefore, it is important to determine the number of seeds in the model. The finer the mesh, the higher the density of finite elements, which allows a better translation of the boundary conditions and higher approximation to the real model, however, the results take more time to obtain. To balance the computational time and the accuracy of the results obtained is necessary to proceed with the mesh convergence analysis [112].

The mesh convergence analysis consists of taking the values of several nodes in the model. With the modification size of the elements, the values change within the same nodes, and the relation between the values obtained in the previous simulation will determine if the model converges accurately.

The geometries chosen in the present thesis (TO and RTCO) have been tested. Even though there are several relative densities for each geometry, it would be extremely time-consuming to carry out the convergence for all of them, consequently, the relative density chosen for the mesh convergence was 0,2, which is the middle relative density in the sample scope, furthermore is the average relative density between compact and dense specimen (50% and 3% relative density, respectively).

After the symmetry analysis was completed, the ¼ model (5,5 cells in length, 1,5 cells in width and 1 cell plus 0,2 in each outer surface (x2)) was used for the mesh convergence analysis, present in Figure B.1.

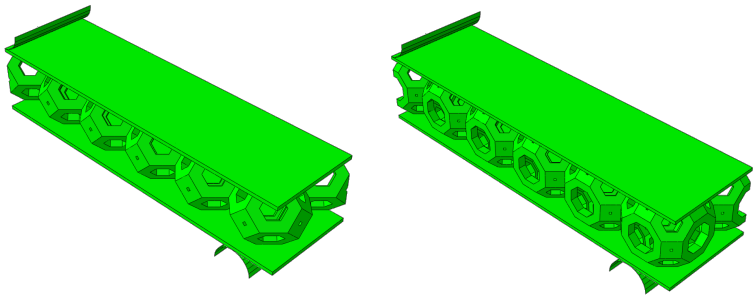

Figure B.1: (left) TO Symmetry model ¼, (right) RTCO Symmetry model ¼.

The variable to calculate the error factor was the average displacement of three nodes presented in each model, presented in Figure B.2. The position of the nodes chosen aims to emulate the whole model and not just a localized region.

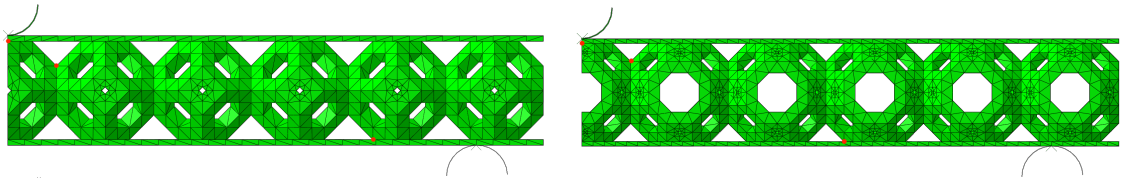

Figure B.2: (left) TO Symmetry model ¼, (right) RTCO Symmetry model ¼.

The number of nodes and elements and the time of each simulation were annotated. The deviation values were obtained by calculating the relative error, the equation used is presented in Equation (B.1).

$$\text{Error}(\%) = \left| \frac{\bar{\Delta}_{M,i} - \bar{\Delta}_{M,i-1}}{\bar{\Delta}_{M,i-1}} \right| \times 100 \tag{B.1}$$

The $\Delta_{M,i}$ is the average displacement obtained in the mesh i, and $\Delta_{M,i-1}$ is the same but for the previous mesh.

In all simulations, the maximum relative error considered is 5% [113], which assures the accuracy needed for all the models studied in the present work.

The Table B.2 presents all the data to make the correct evaluation of the best accuracy-cost ratio from the sizes of the different elements in the TO model.

In the TO model, all the mesh sizes are below 5%, as a consequence, further analysis of the results was taken into account. The increased percentage of computational time was compared with the increased percentage of average relative error.

The analysis concluded that the most appropriated mesh is the one with 0.4 as seed since the relative error only increases by 1.85% regarding the 0.6 mesh and the computational time increases only 1.52% regarding the initial time. Despite the 0.5 being the best accuracy-cost ratio mesh, the difference was not significant, furthermore, 0.4 has a less relative error and allows to have the same mesh as RTCO geometry, presented in the following paragraph.

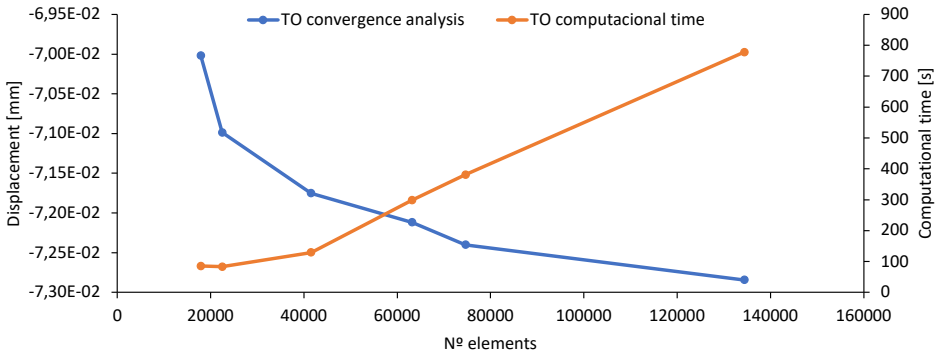

Figure B.3: TO displacement and computational time mesh convergence analysis.

Table B.1: TO Mesh converge analysis.

Element Size	Node Nº	N º Elements	Nº Nodes	Computacional Time [sec]	Displacement [mm]	Average Displacement [mm]	Relative Erro [%]	Average Relative Erro [%]
0,6	1	17885	35444	85	-0,09	-7,00E-02	-	-
	2				-0,08		-	
	3				-0,03		-	
0,5	1	22500	44758	83	-0,09	-7,10E-02	1,75	2,38
	2				-0,08		2,55	
	3				-0,03		2,84	
0,4	1	41543	78870	129	-0,09	-7,18E-02	1,46	1,64
	2				-0,08		1,67	
	3				-0,03		1,79	
0,35	1	63187	117661	299	-0,09	-7,21E-02	0,66	0,58
	2				-0,08		0,67	
	3				-0,03		0,43	
0,3	1	74630	140253	381	-0,09	-7,24E-02	0,63	0,82
	2				-0,08		0,66	
	3				-0,02		1,17	
0,225	1	134402	239418	778	-0,09	-7,28E-02	0,95	0,89
	2				-0,08		0,76	
	3				-0,02		0,96	

Table B.2: TO Mesh converge analysis - time versus relative error.

Element Size	Relative error [%]	Time [s]	Time/Relative error [s/%]
0,6	5,54	-	-
0,5	2,68	0,98	0,37
0,4	1,85	1,52	0,82
0,35	0,66	3,52	5,33
0,3	0,92	4,48	4,87
0,225	-	9,15	-

The Table B.2 has all the data allowing the selection of the best mesh for the RTCO geometry model. The criteria applied were the same as the TO mesh convergence analysis. In the RTCO model, all the mesh sizes are below 5%. Further analysis of the result was taken into account to decide the size of the mesh. The rise in the percentage of computational time was compared with the rise in the percentage of average relative error. The analysis concluded that the most appropriated mesh is 0.4 since the relative error only increases by 1.58% relative to the 0.225 mesh and the computational time increases only 0.01% relative to the initial time, being the best accuracy-cost ration mesh of 0.01.

To conclude, the following size mesh used in the present work is in Table B.5

After obtaining the proper mesh size, it is performed a friction coefficient sensitivity analysis.

Table B.3: RTCO Mesh converge analysis.

Element Size	Node Nº	N º Elements	Nº Nodes	Computacional Time [sec]	Displacement [mm]	Average Displacement [mm]	Relative Erro [%]	Average Relative Erro [%]
0,6	1	32841	62857	154	-0,09	-7,06E-02	-	-
	2				-0,08		-	
	3				-0,03		-	
0,5	1	41576	78078	166	-0,1	-7,18E-02	2,88	2,61
	2				-0,09		2,11	
	3				-0,03		2,86	
0,4	1	50910	94990	156	-0,1	-7,23E-02	0,83	1,32
	2				-0,09		1,39	
	3				-0,03		1,75	
0,35	1	70992	130766	300	-0,1	-7,28E-02	1,46	1,05
	2				-0,09		0,58	
	3				-0,03		1,12	
0,3	1	94594	173434	283	-0,1	-7,28E-02	0,14	0,42
	2				-0,09		0,5	
	3				-0,03		0,61	
0,225	1	161581	292479	744	-0,1	-7,32E-02	0,93	0,84
	2				-0,09		0,48	
	3				-0,03		1,11	

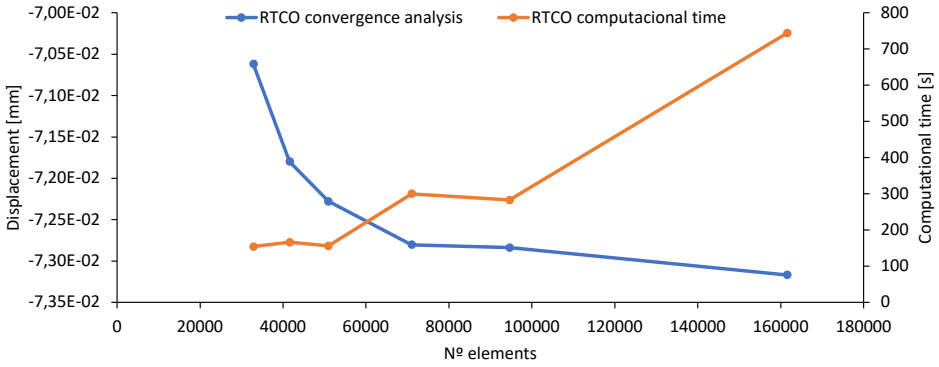

Figure B.4: RTCO displacement and computational time mesh convergence analysis.

Table B.4: RTCO Mesh converge analysis - time versus relative error.

Element Size	Relative error [%]	Time [s]	Time/Relative error [s/%]
0,6	4,31	-	-
0,5	3,12	0,08	0,03
0,4	1,58	0,01	0,01
0,35	1,26	0,95	0,75
0,3	0,5	0,84	1,68
0,225	-	3,83	-

Table B.5: Summary of the element size selected for each topology.

Topology	Element size
TO	0.4
RTCO	0.4

C

Appendix C - Friction coefficient sensitivity analysis

To ensure accuracy during the simulations, the friction coefficient sensitivity analysis was performed.

This type of analysis is important in FEM since allows a systematic approach (where it is possible to identify the variation of the results), optimization (select the optimal friction coefficient) [114], validation of the model [115], accuracy and reliability (identify the range of values for which the results are valid) [116].

The values of the friction coefficient studied were; 0.05, 0.1, 0.15, 0.2, 0.25, 0.5. In the present work, this study aims to understand if there are significant differences in the results between the different friction coefficients since this is a parameter that is difficult to evaluate experimentally, and for which the information present in the literature is scarce. The elastic and plastic regimes were considered, although the most important is the former since the proper application of the structures should not reach the plastic regime. All the values studied are presented in the literature, however, since the most used friction coefficient in literature is 0.2, the reference values are from the model with 0.2. The approach was to gather the results of the reaction force every 10 seconds and calculate the relative error for each value obtaining the maximum relative error possible. The equation used was:

$$\text{Error}(\%) = \left| \frac{\bar{\Delta}_{M,i} - \bar{\Delta}_{M,i-1}}{\bar{\Delta}_{M,i-1}} \right| \times 100 \tag{C.1}$$

The $\Delta_{M,i}$ is the average displacement obtained in the mesh i, and $\Delta_{M,i-1}$ is the same but for the previous mesh.

In the TO model there was no significant change in results using all friction coefficient values, especially in the elastic regime, presented in Table C.1 and Figure C.1, where the maximum error is 3% in the elastic regime.

In RTCO the same approach was taken, concluding the same results, the coefficient values did not have an extreme impact on the final results, especially in the elastic regime where the maximum relative error was 3%, possible to observe in Table C.2 and Figure C.2.

To sum up, in the present work the friction coefficient does not have a significant impact on the final result, since the calculated relative error was less than 5% [113].

Table C.1: Calculation of Relative Error of TO friction coefficient model.

	TO 005		TO 01		TO 015		TO 02		TO 025		TO 05	
Time [s]	Reaction Force [N]	Error [%]	Reaction Force [N]	Error [%]	Reaction Force [N]	Error [%]	Reaction Force [N]	Error [%]	Reaction Force [N]	Error [%]	Reaction Force [N]	Error [%]
0	0	-	0	-	0	-	0	-	0	-	0	-
10	46,26	0%	46,32	0%	46,38	0%	46,44	0%	49,09	-6%	47,79	-3%
20	94,48	0%	94,5	0%	94,52	0%	94,54	0%	93,56	1%	92,25	2%
30	107,66	0%	107,73	0%	107,8	0%	107,87	0%	109,4	-1%	109,68	-2%
40	117,55	0%	117,71	0%	117,87	0%	118,03	0%	117,8	0%	118,87	-1%
50	121,12	1%	121,37	0%	121,62	0%	121,87	0%	120,9	1%	122,13	0%
60	122,18	1%	122,51	1%	122,85	0%	123,3	0%	122,2	1%	123,6	0%
70	122,29	1%	122,72	1%	123,14	0%	123,64	0%	122	1%	123,68	0%
80	122,03	1%	122,59	1%	123,15	0%	123,66	0%	121,2	2%	123,39	0%
90	122,48	2%	123,13	1%	123,79	0%	124,35	0%	120,2	3%	122,89	1%
100	122,71	2%	123,48	1%	124,22	1%	125,01	0%	119,3	5%	122,29	2%
110	122,41	2%	123,3	1%	124,21	1%	125,03	0%	118,4	5%	121,78	3%
120	122,36	2%	123,36	2%	124,35	1%	125,30	0%	117,7	6%	121,43	3%
130	121,91	3%	123	2%	124,11	1%	125,20	0%	117,1	6%	121,23	3%
140	121,19	3%	122,46	2%	123,77	1%	124,95	0%	116,6	7%	121,098	3%
150	120,64	3%	121,92	2%	123,18	1%	124,52	0%	116,2	7%	121,12	3%
160	119,9	3%	121,35	2%	122,79	1%	124,22	0%	115,8	7%	121,05	3%
170	118,94	4%	120,5	3%	122,01	1%	123,61	0%	115,3	7%	120,89	2%
180	117,98	4%	119,56	3%	121,2	1%	122,85	0%	114,8	7%	120,74	2%
	Error max. [%]	4%		3%		1%		0%		7%		3%

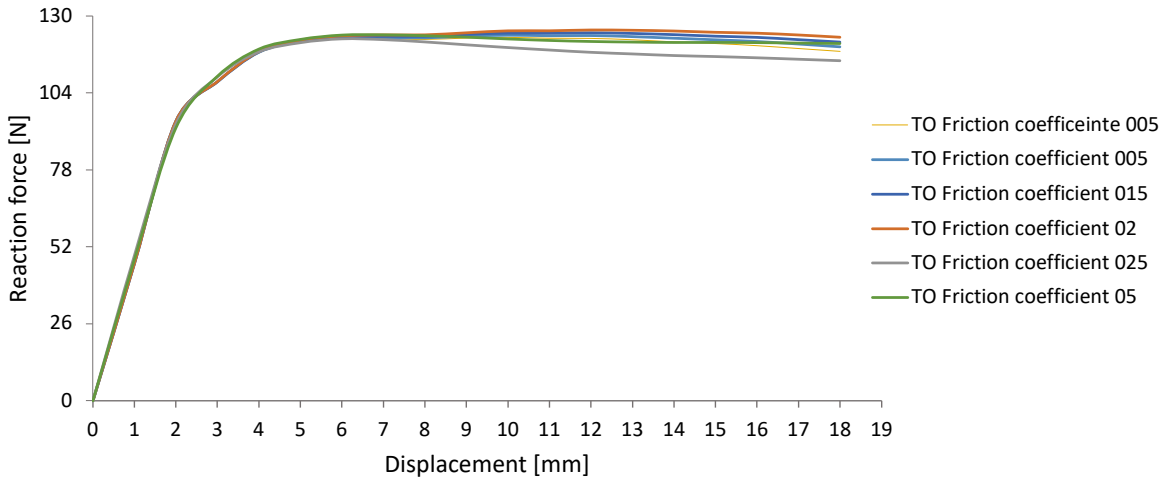

Figure C.1: TO analysis of friction coefficient.

Table C.2: Calculation of Relative Error of RTCO friction coefficient model.

	TO 005		TO 01		TO 015		TO 02		TO 025		TO 05	
Time [s]	Reaction Force [N]	Error [%]	Reaction Force [N]	Error [%]	Reaction Force [N]	Error [%]	Reaction Force [N]	Error [%]	Reaction Force [N]	Error [%]	Reaction Force [N]	Error [%]
0	0	-	0	-	0	-	0	-	0	-	0	-
10	50,92	3%	53,37	8%	49,65	0%	49,58	0%	49,78	0%	48,17	3%
20	102,17	1%	103,13	2%	101,5	1%	100,97	0%	101,54	1%	101,70	1%
30	118,41	1%	116,69	1%	119,05	1%	117,78	0%	119,05	1%	116,99	1%
40	130,34	3%	126,77	0%	126,96	0%	127,09	0%	127,30	0%	132,71	4%
50	136,7	1%	138,04	0%	138,54	0%	138,65	0%	138,93	0%	140,41	1%
60	140,73	2%	142,07	1%	142,67	0%	142,97	0%	143,17	0%	145,14	2%
70	145,75	0%	145,24	1%	145,70	0%	146,16	0%	146,62	0%	148,86	2%
80	147,95	1%	148,55	1%	149,13	0%	149,70	0%	150,28	0%	153,07	2%
90	150,64	1%	151,36	1%	152,05	0%	152,74	0%	153,43	0%	156,8	3%
100	153,6	1%	154,49	1%	154,62	1%	155,42	0%	156,23	1%	160,18	3%
110	154,95	2%	156,44	1%	157,47	0%	157,52	0%	159,46	1%	164,39	4%
120	156,99	2%	158,1	1%	158,98	1%	160,02	0%	161,30	1%	166,64	4%
130	158,36	2%	159,56	1%	160,12	1%	161,28	0%	162,46	1%	168,18	4%
140	159,5	2%	160,6	2%	161,96	1%	163,34	0%	164,65	1%	171,35	5%
150	160,19	3%	161,68	2%	163	1%	164,44	0%	166,1	1%	173,18	5%
160	161,06	3%	162,33	2%	163,91	1%	165,5	0%	167,1	1%	174,86	6%
170	161,34	3%	163,17	2%	164,75	1%	166,6	0%	168,29	1%	176,65	6%
180	161,65	3%	163,48	2%	165,35	1%	167,17	0%	168,96	1%	177,84	6%
	Error max. [%]	3%		8%		1%		0%		1%		6%

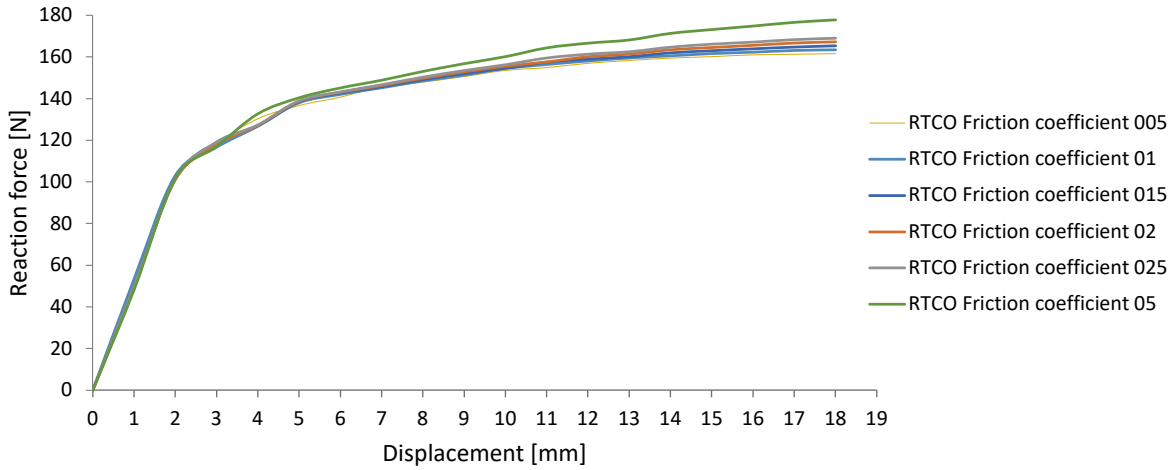

Figure C.2: RTCO analysis of friction coefficient.

D

Appendix D - Values of 3PB experimental test and FEA of Stainless Steel and Iron

Table D.1: Table of measurements of samples RTCO experimental bending test and FEA of Stainless steel.

	RTCO													
	0,054		0,2434								0,4057			
	0,2		0		0,2		0,4		0,2-2		0,2		0,56	
	mass [g]	volume [mm^3]	mass [g]	volume [mm^3]	mass [g]	volume [mm^3]	mass [g]	volume [mm^3]	mass [g]	volume [mm^3]	mass [g]	volume [mm^3]	mass [g]	volume [mm^3]
Lab	67,4	4609,3	70,8	6839,2	117,49	9854,9	130	13125,1	181,8	16567,2	149,2	14363,2	190,6	20162,6
FEA SS	36,8	4584	55,6	6920,4	80,6	10041,7	105,64	13163	136,2	16962	112,1	13963,8	157,2	19582,1

Table D.2: Table of measurements of samples TO experimental bending test and FEA of Stainless steel.

	TO													
	005		025								04			
	02		0		02		04		02-2		02		056	
	mass [g]	volume [mm^3]	mass [g]	volume [mm^3]	mass [g]	volume [mm^3]	mass [g]	volume [mm^3]	mass [g]	volume [mm^3]	mass [g]	volume [mm^3]	mass [g]	volume [mm^3]
Lab	47,8	4603,7	67,2	6718,3	104,1	9820,3	146,6	14993,3	165,5	16485,2	131,4	13288,1	208,6	23412
FEA SS	36,1	4496	55,5	6916,6	80,6	10038	121,9	15188,1	136,1	16954,6	112,8	14051,6	186,7	23259,5

Table D.3: Table of values of experimental bending test and FEA of Stainless steel and Iron samples.

		RTCO				TO			
		5% - 0,2 mm				5% - 0,2 mm			
LAB	*Max Rf. [N]*	543				470			
	Ea [J/mm²]	5351				2141			
	K.	170				138			
	Max Rf. (elastic) [N]	536				468			
FEA Stainless Steal	*Max Rf. [N]*	611				541			
	Ea [J/mm²]	5657				5126			
	K. [N/mm]	233				210			
	Max Rf. (elastic) [N]	544				500			
FEA Iron	*Max Rf. [N]*	452				420			
	Ea [J/mm²]	4479				4071			
	K. [N/mm]	238				179			
	Max Rf. (elastic) [N]	417				420			
		25%				25%			
		0	0,2	0,4	0,2-2	0	0,2	0,53	0,2-2
LAB	*Max Rf. [N]*	303	1064	1958	2695	179	778	2344	2363
	Ea [J/mm²]	5101	19913	37696	52782	2958	14809	45513	46569
	K. [N/mm]	37	255	565	1055	17	238	650	755
	Max Rf. (elastic) [N]	196	656	1220	1518	139	465	1746	1875
FEA Stainless Steal	*Max Rf. [N]*	272	1030	1968	2638	149	778	2438	2463
	Ea [J/mm²]	4546	20004	38294	52924	2513	14335	47930	49350
	K. [N/mm]	30	259	659	1249	15	274	875	1288
	Max Rf. (elastic) [N]	180	765	1187	1808	123	637	1557	1545
FEA Iron	*Max Rf. [N]*	203	803	1505	2076	112	571	1882	480
	Ea [J/mm²]	3633	15703	29032	41240	1991	11350	35339	38367
	K. [N/mm]	28	240	577	1074	17	271	929	1111
	Max Rf. (elastic) [N]	160	579	1017	1289	80	475	1115	1333
		40%				40%			
		0,2		0,56		0,2		0,79	
LAB	*Max Rf. [N]*	1369		2981		805		3728	
	Ea [J/mm²]	25608		57083		28686		71939	
	K. [N/mm]	320		855		212		1064	
	Max Rf. (elastic) [N]	757		1726		583		2801	
FEA Stainless Steal	*Max Rf. [N]*	1336		3057		909		3974	
	Ea [J/mm²]	25650		59224		18197		76712	
	K. [N/mm]	353		1016		264		1163	
	Max Rf. (elastic) [N]	824		1820		760		2782	
FEA Iron	*Max Rf. [N]*	1033		2337		713		3043	
	Ea [J/mm²]	19848		44886		14331		57893	
	K. [N/mm]	350		1082		287		1151	
	Max Rf. (elastic) [N]	621		1298		516		2039	

Appendix E - Performance index calculations

To obtain the formula for the performance index, several calculations were conducted. The performance index (PI) is obtained using performance metrics, and it depends on control variables. In this case the control variables include the dimensions of the specimen, the force it must carry, and the properties of the material from which it is made [105]. The equation used to calculate the performance metrics (PI) uses controlled variables (eq. (E.1)). In the PI equation "f" means "a function of", load is represented by P, G is geometry and M is material.

$$PI = f[(P), (G), (M)] \tag{E.1}$$

Depending on the study and selection, the different variables can be included or disregarded [105].

For this study the performance index has the Length L and width b specified (geometric constraints), and the objective is to minimize the mass of the beam. The free variable is the specimen's height.

In the case of a rectangular plate, the objective function for the specimen mass is shown in eq. (E.2), where m is the mass of the specimen, b is the width of the specimen, L is the length, h is the height and the cellular material density is represented by $\rho*$.

$$m = bhL\rho* \tag{E.2}$$

Since bending tests were performed, the bending stiffness equation is used (eq. (E.3)). The bending stiffness is represented by k, the moment of inertia is I, C_1 is a constant that depends on the distribution of the loads, the Young's modulus is represented by E and the length of the sample is L.

$$k = \frac{IC_1E}{L^3} \tag{E.3}$$

Through the eq. (E.3), the I is calculated:

$$I = \frac{L^3k}{C_1E} \tag{E.4}$$

The mass can be reduced by reducing h, but as a free variable, it must be explicitly eliminated from the mass

equation. To eliminate h the eq. (E.5) is used.

$$\sigma = \frac{Mc}{I} = \frac{D_1 F \frac{L}{2} \frac{h}{2}}{\frac{L^3 k}{C_1 E}} \tag{E.5}$$

Where D1 is a constant related to the distribution of loads. The eq. (E.6) eliminates h and the objective function gives:

$$h = \frac{4\sigma L^2 k}{D_1 C_1 F E} \tag{E.6}$$

In the initial eq. (E.2) the h is substituted by the eq. (E.6) and the $\rho*$ is substituted using eq. (E.7). The Young's modulus is given by the eq. (E.8) [117].

$$\rho* = \bar{\rho}\rho_s \tag{E.7}$$

$$\frac{E}{E_s} = \alpha(\frac{\rho*}{\rho_s})^2 = \alpha\bar{\rho}^2 \tag{E.8}$$

The final equation is presented in eq. (E.9).

$$m = bhL\rho* = b(\frac{4\sigma L^2 k}{D_1 C_1 F E})L\rho* \tag{E.9}$$

Assuming that σ can be identified with the cellular material's yield strength, and that it scales similarly with $\bar{\rho}$ as in the case of the Young's modulus, we obtain:

$$m = \frac{4bL^3}{C_1 D_1} \frac{\sigma_s^y \rho_s}{E_s} \frac{\bar{\rho} k}{F^y} \tag{E.10}$$

Where σ_s^y is the solid's yield strength and F^y is the force at yield. In order to obtain the variables to the specific problem studied in this dissertation, the k, $\bar{\rho}$ and F_y were combined to form the Performance Index, shown in eq. (E.11).

$$PI = \frac{k\bar{\rho}}{F^y} \tag{E.11}$$

This index is to be minimized, thus the best samples are those with the lowest k and $\bar{\rho}$ and higher F^y (MRF in section 4.3).